University of Milano Bicocca

Department of Materials Science

Study of new materials and their functionality for hydrogen storage and other energy applications

Doctorate School in Materials Science

Thesis

by

Mohammad Reza Ghaani

Supervisor: prof. Michele Catti

January 2014

Summary

The first part of this thesis deals with hydrogen storage materials, in view of their applications as promising energy carriers. One of the main open problems with these materials is: how can their decomposition temperature be lowered, when hydrogen is wanted to be released, so as to improve the energy efficiency of the process. A possible answer is given by joint decomposition of two or more hydrides, if very stable mixed compounds are formed ('hydride destabilization').

Aiming at this result, the new hydride composite *2LiBH₄-Mg₂FeH₆* was considered, it was synthesized, and its thermodynamic and kinetic properties were investigated. The sequence of dehydrogenation reactions of the composite was studied by PCI (Pressure-Composition-Isotherm) and TPD (Temperature-Programmed-Desorption) techniques in a Sievert apparatus. The produced phases were identified by ex-situ X-ray diffraction, in-situ synchrotron X-ray diffraction and FTIR spectroscopy. Three distinct plateaus are detected on each isotherm: A, B, and C on decreasing pressure. The A reaction, involving formation of *FeB*, *MgH_2* and *LiH*, occurs at higher pressure/lower temperature than dehydrogenation of either pure hydrides; these are then effectively destabilized thermodynamically. The B process is plain decomposition of *MgH_2*, and in C the magnesium produced reacts with *$LiBH_4$* left forming *MgB_2* and *LiH*. The B+C sequence is fully reversible, and it corresponds to two-step dehydrogenation of the *$LiBH_4/MgH_2$* system.

$$2Mg_2FeH_6 + 2LiBH_4 \rightarrow 2LiH + 4MgH_2 + 2FeB + 5H_2 \quad \text{(A)}$$

$$MgH_2 \leftrightarrow Mg + H_2 \quad \text{(B)}$$

$$2LiBH_4 + Mg \leftrightarrow 2LiH + MgB_2 + 3H_2 \quad \text{(C)}$$

Reaction enthalpies and entropies were obtained through van't Hoff plots of all processes, thus providing a full thermodynamic characterization of the system.

Reaction enthalpies and entropies were obtained through van't Hoff plots of all processes, thus providing a full thermodynamic characterization of the system.

The rates of the irreversible A reaction and reversible C reaction (with significant sorption/desorption hysteresis) were measured by isothermal-isobaric experiments in a Sievert-type apparatus. Measurements were done at several temperature *T* and overpressure *Δp/p* values, deriving the rate constants *k(T,Δp/p)* by Avrami's fitting of reaction advancement vs. time. The results could be rationalized on the basis of the:

$$k = Aexp(-E_a/RT) = A_0 exp[-E_a^0/RT + a(\Delta p/p)]$$

kinetic formula, which couples the standard Arrhenius approach for thermal effects with an exponential dependence of the rate constant on overpressure. The empirical *a* coefficient varies with temperature in a way that requires the activation energy and entropy to depend linearly on *Δp/p*. For the first of the above reactions (A), E_a = -151(*Δp/p*) + 118 kJ.mol^{-1} and ln(*A*/min^{-1}) = -34(*Δp/p*) + 16; similar values are obtained for the second one (C). Relations of this kinetic model with the thermodynamic driving force *ΔG* and with equations of electrochemical kinetics, where overpressure is replaced by overvoltage, are discussed.

In addition to the main part of the research work done, which was summarized above, other topics were covered in this thesis work. One of them concerns 'nanoconfinement' of hydrogen storage materials, i.e. the attempt to insert the active hydrides into inert carbon matrices, so as to decrease the size of particles and then improve the kinetics of the hydrogen absorption-desorption processes. In this respect, the goal was to confine Mg_2FeH_6 and Mg_2CoH_5 inside scaffolds of carbon xerogels. We hoped to synthesize these complex hydrides directly in the matrices by infiltration of iron/cobalt and magnesium hydride and subsequent reaction. The steps of infiltration of iron and cobalt oxides and following chemical reduction to metal state were successfully performed, but the final step of complex hydride formation could not be carried out to the final stage.

Another important class of hydrogen storage materials was briefly considered in the thesis work: amidoboranes and their alkali derivatives, with particular focus on lithium amidoborane $LiNH_2BH_3$. The thermodynamic behavior of this compound was studied by use of the TPD method at variable temperature and H_2 pressure. The decomposition

temperature was determined, and it was seen to be little dependent on pressure. As its products of dehydrogenation are amorphous, the XRD technique is not useful unfortunately for identification purposes. The possible joint decomposition of MgH_2 and $LiBH_4$ with $LiNH_2BH_3$ was also investigated. The dehydrogenation reaction of MgH_2-$LiNH_2H_3$ has a similar behavior to that of pure lithium amidoborane, whereas $LiBH_4$ seems to destabilize $LiNH_2BH_3$.

In the second part of this thesis work lithium oxide materials, of relevant interest for applications to batteries, were investigated. The chemical lithiation reaction of niobium oxide was considered, as equivalent to the electrochemical process of lithium insertion on discharging a Nb_2O_5 cathode vs. a metal *Li* anode. Thus, the $Li_2Nb_2O_5$ compound was synthesized by reaction of monoclinic α-Nb_2O_5 with n-butyllithium. This material was investigated by neutron powder diffraction (D2B equipment at ILL, France) and its structure was Rietveld refined in space group *P2* to wR_p=0.045, locating the *Li* atoms inserted in the α-Nb_2O_5 framework. The ensuing chemical formula turned out to be $Li_{12/7}Nb_2O_5$. A part of *Li* atoms are more strongly bonded (five coordinated *O* atoms), a part are less (coordination number = 4).

Acknowledgements

I wish to express my deep gratitude to my supervisor, Professor Michele Catti, for his guidance in my PhD journey with its challenges and interests. I appreciate what I have learned from him; he taught me how to look at science, and how to think and to act as a scientist.

It is also my great pleasure to thank Dr. Torben Jensen and his friendly group, in particular Mr. Payam Javadian and Dr. Dmytri Korablov. I spent 6 months with them in Aarhus University; it was a great experience working with them and learning from them.

Thanks to the instrument scientist Emmanuelle Suard (ILL, Grenoble, France) for her help with the neutron diffraction data collection on the D2B equipment.

Personal thanks and love to my family that supported me during these three years. Without their love and support I could never have achieved everything that I have in life.

1 Hydrogen storage materials

1.1 Introduction

1.1.1 Energy from hydrogen

Reducing CO_2 emission from burning fossil fuels has been clearly recognized as the main action to moderate global warming and climate change. On top of this, resources of oil, coal and natural gas are limited and requiring alternative solutions before the demand becomes unsustainable anymore. In this scenario hydrogen as an energy carrier shows great potential.

Hydrogen can be obtained via various sources whether from electrolysis of water [1, 2], methane and methanol reformation [3] or hydrogen evolution from biomass reactors [4], and can be used to generate electricity by direct combination with O_2 in fuel cells or using in combustion engines to make mechanical energy.

Many researches, including experimental and theoretical studies, have recently been carried out the use of hydrogen as an energy carrier. However, it is necessary to understand the broader aspects of hydrogen energy to make it realizable. For hydrogen

fueled transportation the most fundamental technological and economic challenges stated by DOE (United state Department Of Energy) [5] are:

- **Weight and Volume:** The weight and volume of hydrogen storage systems are presently too high, resulting in inadequate vehicle range compared to conventional petroleum fueled vehicles. Materials and components are needed that allow compact, lightweight, hydrogen storage systems.
- **Efficiency:** Energy efficiency is a challenge for all hydrogen storage approaches. The energy required to get hydrogen in and out is an issue for reversible solid state materials.

- **Durability:** Durability of hydrogen storage systems is inadequate. Materials and components are needed that allow hydrogen storage systems with a lifetime of 1500 cycles.
- **Refueling Time:** Refueling times are too long. There is a need to develop hydrogen storage systems with refueling times of less than three minutes over the lifetime of the system.
- **Cost:** The cost of on-board hydrogen storage systems is too high, particularly in comparison with conventional storage systems for petroleum fuels. Low-cost materials and components for hydrogen storage systems are needed, as well as low-cost, high-volume manufacturing methods.
- **Life-Cycle and Efficiency Analyses:** There is a lack of analyses of the full life-cycle cost and efficiency for hydrogen storage systems.

To realize hydrogen powered vehicle, DOE has translated the performance of a gasoline powered vehicle into the targets for hydrogen storage system. The latest DOE hydrogen storage targets established in 2012 is reported in Table 1-1. The 2017 targets would allow some low volume vehicles to achieve a driving range of 300 miles (~480 km). The current target for gravimetric capacity of a hydrogen storage system is 5.5 wt% H_2 in the year 2017 and ultimately it would be 7.5 wt% H_2. The delivery temperature target has been set at –40 to 85 °C with a delivery pressure of 5 bar for fuel cell applications. Recharging ideally would not take more than 2.5 minutes, it would need to be rapidly reversible, withstand 1500 de/rehydrogenation cycles and be of low enough cost for widespread acceptance [5].

Table 1-1. Technical System Targets: Onboard Hydrogen Storage for Light-Duty Fuel Cell Vehicles [5].

Storage Parameter	Units	2017	Ultimate
System Gravimetric Capacity	kWh/kg ($kg\ H_2/kg$ system)	1.8 (0.055)	2.5 (0.075)
System Volumetric Capacity	kWh/L ($kg\ H_2/L$ system)	1.3 (0.040)	2.3 (0.070)

Durability/Operability			
Min/max delivery temperature	ºC	-40/85	-40/85
Operational cycle life	Cycles	1500	1500
Charging / Discharging Rates			
System fill time (5 kg)	Min	3.3	2.5

1.1.2 Hydrogen storage

The storage of hydrogen for use in mobile applications involves a balance and compromise between two different aspects of the storage system; the volumetric and gravimetric capacities. Therefore it is clear that the increase in volumetric capacity will always have an effect on the gravimetric capacity of the system. Figure 1-1 shows the volumetric and gravimetric densities of different storage materials alongside the conventional storage methods [6].

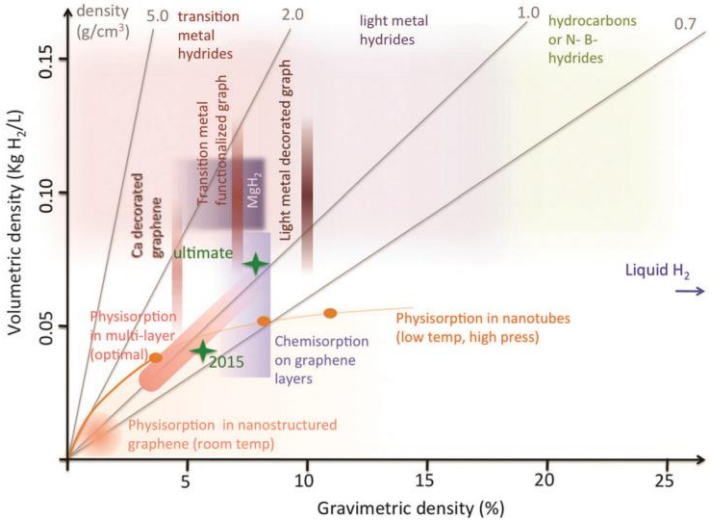

Figure 1-1. Gravimetric vs. volumetric density diagram for several hydrogen storage systems. The DOE targets (for 2015 and ultimate) are indicated with green stars. The constant density lines are in grey [6].

There are several ways to store the hydrogen; each method has its own advantages and disadvantages. In 2004, Züttel [7] described six main categories for hydrogen storage (Table 1-2); the first two known as conventional hydrogen storage techniques, the third process is a type of hydrogen generation (chemical storage) and the last three are solid-state hydrogen storage techniques.

Table 1-2. The six basic hydrogen storage methods and phenomena [7].

Storage method	ρ_m ($mass$%)	ρ_V ($kg\ H_2$ /L)	T (°C)	p (bar)
High-pressure gas cylinders	13	<0.04	RT	800
Liquid hydrogen in cryogenic tanks	Size dependent	0.071	-252	1
Metals and complexes together with water	<40	>.015	RT	1
Adsorbed hydrogen	~2	0.02	-80	100
Absorbed on interstitial sites in a host metal	~2	0.15	RT	1
Complex compounds	<18	0.15	100	1

1.1.1.1 Gaseous form

At the present time, hydrogen storage options have commonly used high pressure gas containers for both stationary purposes and on-board applications. Compression is the simplest way to store hydrogen in a cylinder at pressures up to 800 bar, but due to the energy density of 1.3 kWh.L^{-1} would require a storage volume too big to satisfy the fuel demand of 350 miles range (or 5.6 kg of H_2 on board) [5].

The issues with gas tanks revolve around high pressure, weight, volume, conformability and cost. These tanks must be as light as possible (high gravimetric density) but at the same time strong enough to withstand the internal forces exerted on the walls by the high pressure hydrogen. The materials employed must also be resistant to hydrogen absorption firstly to prevent any leakage of hydrogen and thermally insulated to prevent any heat transfer to the hydrogen inside [8].

High pressure hydrogen storage has several distinct advantages over liquid hydrogen storage in term of structure and cost, since it does not require super-insulation

to maintain cryogenic conditions [4]. In addition, compared to liquid hydrogen storage, the structure of high pressure tanks is much simpler due to the different technical requirements.

1.1.2.1 Liquid form

In principle, storage of hydrogen in a liquid hydrogen tank offers a significantly higher gravimetric density than in a compressed gas tank, since the volumetric capacity of liquid hydrogen and compressed hydrogen gas are 0.070 $kg.L^{-1}$ and 0.039 $kg.L^{-1}$ (at 700 bar) respectively. Therefore, the driving range for vehicles using can be longer than that for compressed hydrogen. Liquid hydrogen tanks can be refueled quickly (in 3 min) with relatively limited evaporative losses [9].

Hydrogen is typically liquefied using the Joule–Thomson cycle [9] which compresses hydrogen gas, cools it down with a heat exchanger and expands the gas rapidly that forms liquid hydrogen. The liquefaction of hydrogen consumes approximately 30% of its heating value, so there is inevitable energy loss during this operation. This problem could be overwhelmed by thermal insulation application, but this affects the system-level gravimetric and volumetric capacity, and above all, increases the cost.

However, despite existing insulated cryogenic tanks with extremely low heat transfer from ambient (1–3 W); Hydrogen boil-off is still a problem. In fact hydrogen has to be vented after 3–5 days of inactivity, and it can happen that after a long period of inactivity the loaded hydrogen depleted completely from the tank [10]. Hydrogen boil-off is also considered a critical safety issue while using cryogenic liquid, when vehicles are parked in limited spaces such as parking garages. Because liquid hydrogen expands considerably as it warms between 20 K to its critical point (33 K), the tanks are filled to only 85–95 % capacity to prevent leaks, leaving 5–15 % of empty space called ullage [11].

Considering the tank cost issues, the low efficiency of the liquefaction process, hydrogen boil-off, and the safety storing hydrogen in the liquid state is not a suitable for onboard applications.

1.1.2.2 Solid state

Although with the compressed and liquid storage options, hydrogen is accessible for use, these storage methods still cannot cover many of the options summarized in Table 1-1. Therefore, hydrogen storage requires a great technological discovery, that is, the storage of hydrogen in some solid state materials.

This method can be dividing into two categories:

1. **Physically bound hydrogen**; where the hydrogen molecule is adsorbed on a high surface area substrate (exterior or interior) such as carbon nanotubes, and

2. **Chemically bound hydrogen**; where the hydrogen atom has formed a chemical compound with the substrate (e.g. metal hydrides, complex hydrides, and chemical hydride).

1.1.2.2.1 Physisorption

In physical adsorption, hydrogen is weakly energetically bound to the material with high surface area. The hydrogen molecules usually cover the surface via weak van der Waals interaction [12]. The adsorption is a fast process and the saturation is achieved within minutes after hydrogen pressure is stabilized, and it is fully reversible. The strength of the van der Waals interaction for hydrogen is very weak, with an enthalpy of adsorption (ΔH_a) between 4 and 10 kJ.mol^{-1} [13]. Therefore, very low temperature, in the range of the temperature of liquid nitrogen, is necessary to adsorb hydrogen gas on a surface by this technique. Surface area is the main factor which controls hydrogen adsorption capacity of these materials. Higher capacity provides by the material with higher surface area. The most frequently studied sorbents are activated carbons, carbon nanostructured materials (e.g. fullerenes [14, 15], carbon nanotubes [16, 17], grapheme [18, 19]), and metal-organic frameworks (MOF) [20, 21].

1.1.2.2.2 Chemisorption

Unlike adsorption (physisorption), in absorption (chemisorption) molecular hydrogen is dissociated and occupies interstitial sites in the metallic or alloy matrix [22]. Hydrogen release from chemically bound hydrogen storage materials can be

achieved either by increasing the temperature or by reducing the pressure. In continue this phenomenon in metal hydrides is explained thoroughly.

1.1.3 Metal hydrides

Metal hydrides are among the most common materials for hydrogen storage and represent an extremely broad research field at the moment. Hydrogen can chemically react with some solids forming covalent or ionic bonds, i.e. be stored via chemisorption. Most common materials considered for hydrogen storage are various metal hydrides (e.g. hydrides of elemental metals and complex hydrides).

Metallic hydrides can be split broadly into two groups with opposing advantages and disadvantages for hydrogen storage applications.

1. Intermetallic metal hydrides: with high volumetric hydrogen capacity and facile hydrogen releasing (in comparison with light metal hydrides) [7]. These materials are not suitable for mobile applications due to their low gravimetric storage capacity (1.5 wt% H_2 in case of $LaNi_5H_6$). This is the main issue for all intermetallic hydrides, with gravimetric capacities less than 4 wt% H_2; they became impractical for mobile applications [23].
2. Light metal hydrides: with large gravimetric storage capacities through the use of light, alkali and alkaline earth metals. The problematic issues for light metal hydrides in addition to their low volumetric storage capacity are high hydrogenation/dehydrogenation temperatures, slow kinetics, and degradation upon successive adsorption/desorption cycling [24].

1.1.3.1 Reaction mechanism

A schematic of hydrogen interaction with a metal surface is illustrated in Figure 1-2. It shows all the individual reaction steps including bulk processes. The formation of the metal hydride can be divided into these following elementary reactions [25-27]:

Dissociation/adsorption: The first step is the dissociation of adsorbed hydrogen on the metal/hydride surface (Figure 1-2-point 1).

Surface penetration: From the surface the hydrogen atoms migrate into the subsurface (point 3).

Bulk diffusion: From the subsurface, the hydrogen atoms diffuse into the bulk (point 4).

Hydride formation: Hydrogen atoms in the bulk (corresponding to a solid solution) can generate hydride nuclei which grow to larger hydride grains by trapping additional hydrogen atoms during reaction advancement (point 6). The formation of a hydride phase complicates the picture somewhat since hydrogen diffusion can also take place through the hydride (point 5).

For dehydrogenation the process is the reverse. A reaction mechanism can be projected on the basis of the above reversible elementary reactions. Looking over the hydrogenation/ dehydrogenation kinetic properties, the rate determining step can roughly be split into two major classes; one is either a surface process such as dissociation or bulk diffusion mechanism (Diffusion control and/or contracting envelope kinetic model) limiting the overall kinetics and the other can be due to nucleation and growth mechanism (Avrami model) reducing the overall kinetics.

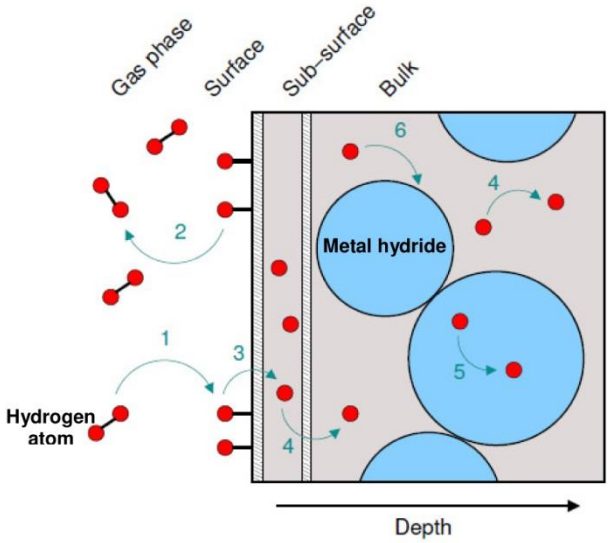

Figure 1-2. Schematic illustration of the different mechanisms involved in the formation of a metal hydride [28].

1.1.3.2 Thermodynamics

The thermodynamics of the hydrogen absorption/desorption reaction is one of the most critical properties of a hydrogen storage material. The thermodynamic properties of the hydrogenation/dehydrogenation reaction are determined precisely by the use of Sievert's apparatus. The pressure-composition absorption isotherm (PCIa) measured at a certain temperature for a reversible hydride is presented on the left side of Figure 1-3. The host metal initially dissolves hydrogen forming a solid solution (α-phase). Afterward, with hydrogen pressure (concentration) increasing, nucleation and growth of the hydride phase (β-phase) occurs. While the two phases coexist, the isotherms show a flat plateau (in definite pressure). The length of this plateau unveils the amount of stored hydrogen. In the pure β-phase, the hydrogen pressure rises steeply with the concentration. The two-phase region ends in a critical point, T_C, which the α to β transition takes place continuously above that temperature [29].

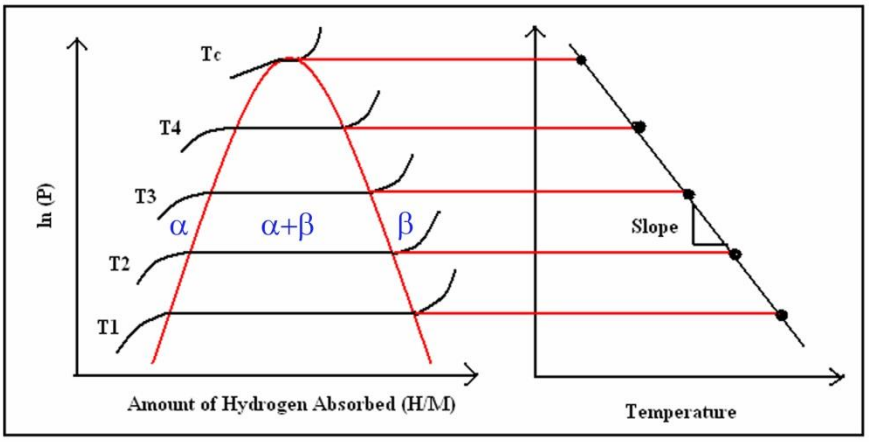

Figure 1-3. Schematic PCT diagram at different temperature (*T1<T2<T3<T4<T$_c$*)(left side), and the van't Hoff plot (right side).

The van't Hoff plot is an appropriate way to designate the pressure-temperature stability of hydrides. In Figure 1-3, a van't Hoff plot is also presented on the right side, which relates the pressure (P), the temperature (T), enthalpy (ΔH_d), and entropy (ΔS_d) of the dehydrogenation reaction. This relation is stated by the van't Hoff equation:

$$ln\left(\frac{P}{P_0}\right) = \frac{\Delta S_d}{R} - \left(\frac{\Delta H_d}{R}\right) \times \left(\frac{1}{T}\right) \quad 1\text{-}1$$

Where P is the equilibrium pressure and R is the gas constant. In the van't Hoff plot, the slope of the line is equal to the minus dehydrogenation enthalpy divided by the gas constant ($-\Delta H_d/R$), and the intercept is equal to the entropy of formation divided by the gas constant ($\Delta S_d/R$). ΔH_d represents the strength of the metal hydrogen bonding [7]. ΔS_d value relies on the intrinsic entropy of the formed hydride.

Another frequently used method for experimentally studying thermodynamic properties is differential scanning calorimetry (DSC). DSC is a thermal analysis technique that measures the difference heat flow between a sample and a reference material as a function of temperature during a controlled temperature program. The advantages of DSC method are: short measurement times (on the order of hours), small sample sizes (about 10mg), and variety of indirectly measurable data (e.g. thermodynamic, kinetic, or thermal information). In the case of hydrogen storage material thermodynamic study, DSC can be used for obtaining enthalpy data for both hydrogen storage reactions and for other possible physico-chemical events, such as melting or polymorphic transformations.

During a DSC measurement, the reference and the sample sensors detect a constant increase of temperature ramp, as stated by the heating program (e.g. 1 °C.min^{-1}). Once a thermal event occurs, for instance, endothermic hydrogen release, to keep the temperature of the sample constant, the heat flux supplied to the sample is increased while the final sample temperature continues to increase linearly according to the temperature program. Once the hydrogen release event is complete, the additional applied heat flux will removed. The area under the sample signal curve is proportional to the amount of heat consumed for that event and consequently the ΔH of the reaction [30].

1.1.3.3 Hydride destabilization using reactive additives

In 1968, Reilly and Wiswall [31] pioneered the destabilization concept for hydrides. The basic idea was to use alloys to make the hydrides less thermodynamically stable.

Thermodynamic destabilization is achieved by using additives that form a new compound through dehydrogenation. Thus, the addition of a second phase to a metal hydride can cause thermodynamic destabilization of that metal hydride by the formation of an end product which has either a lower energy level. Concerning the definition of Gibbs free energy (ΔG):

$$\Delta G = \Delta H - T\Delta S \qquad 1\text{-}2$$

The idea of having lower ΔG value can be satisfied either by lowering ΔH or increasing the ΔS. This process can be displayed in van't Hoff plot with lower slope or higher intercept respectively in comparison with pure hydride decomposition line [32].

To get a better insight on the principle of the destabilization concept, it is better to illustrate it using a general energy diagram. Figure 1-4 generalized energy diagram presenting destabilization through alloy formation upon dehydrogenation. Including the alloying additive, *B*, reduces the energy level of dehydrogenation by the formation of AB_x and effectively destabilizes the hydride AH_2, even though the bonding of AH_2 is not altered [33].

For instance the addition of MgH_2 to $LiBH_4$ led to the formation of MgB_2 and LiH upon dehydrogenation decreases the dehydrogenation enthalpy about 25 kJ.mol^{-1} H_2 lower than the enthalpy for pure $LiBH_4$ to LiH and B [34].

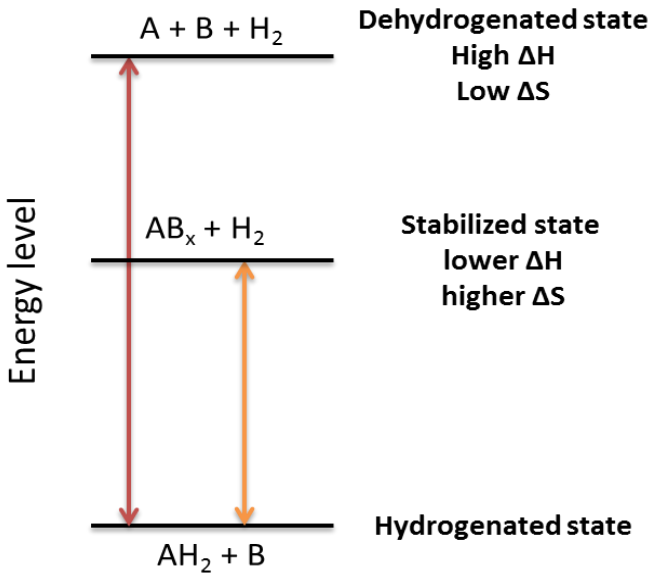

Figure 1-4. Generalized energy diagram illustrating destabilization and stabilization.

1.1.3.4 Metal hydride systems

Magnesium Hydride

Magnesium shows promising potential as an on-board hydrogen storage material due to its low cost, good reversibility in cycling and its maximum theoretical storage capacity of 7.66 wt.% H_2 [35]. However, the main disadvantages of MgH_2 as well as most other metal hydrides are its high temperature dehydrogenation reaction, slow desorption/absorption, and a high reactivity towards air and oxygen [36, 37].

The Mg/MgH_2 system can be destabilized thermodynamically by alloying with other elements such as *Ni*. However this affects the storage capacity as the *Ni* is non-hydriding [31]. Extensive research has been undertaken to try to improve the hydrogen absorption/desorption kinetics in magnesium hydrides. High velocity ball milling [38] or nanoconfinement [39] significantly increases the sorption kinetics by reducing the particle size and hence increasing its surface area. Catalysts such as, V_2O_5 or Nb_2O_5 have been found to reduce the charging time to less than two minutes by increasing hydrogen dissociating rate on the magnesium surface at 250 °C [40, 41].

Lithium borohydride

Complex hydrides are salt-like materials in which hydrogen is covalently bound to the central atoms forming "complex anions". In general, complex hydrides have the chemical formula $M_xMe_yH_z$. Where position *M* is preferentially occupied by elements of the first or second groups of the periodic table and *Me* is occupied either by boron or aluminum are well known and have been intensively investigated.

Boron is an element lighter than aluminum thus borohydrides (MBH_4) possess greater gravimetric storage densities than alanate hydride ($MAlH_3$).

There are four endothermic peaks that were observed during the dehydrogenation process of $LiBH_4$. The first endothermic peak at around 110 °C is assigned to a polymorphic transformation from orthorhombic to hexagonal structure , while the second endothermic peak at around 267-280 °C is as a result of the melting of $LiBH_4$. The third endothermic peak at 490 °C corresponds to the first dehydrogenation of $LiBH_4$, and the fourth endothermic peak at 680 °C is assigned to the release of three of the four hydrogen atoms [42].

$$LiBH_4 \xrightarrow{about\ 490°C} LiH + B + \frac{3}{2}H_2\ (13.8\ wt\%\ H_2) \qquad 1\text{-}3$$

$$LiH \xrightarrow{about\ 680°C} Li + \frac{1}{2}H_2\ (4.7\ wt\%\ H_2) \qquad 1\text{-}4$$

Nevertheless, high dehydrogenation temperature and slow sorption kinetics prevents the use of $LiBH_4$ as a hydrogen storage material. In order to overcome these difficulties, many approaches have been tried such as application of the destabilization concept or the use of catalyst. Previous studies have shown that joint decomposition of $LiBH_4$ with some hydrides such as MgH_2 [34], CaH_2 [43], ScH_2 [44], CeH_2 [44], YH_3 [45] and Mg_2NiH_4 [46] are effective in reducing the dehydriding temperature of $LiBH_4$.

Magnesium Iron hydride

Complex transition metal hydrides derive their name from the presence of one transition metal as a part of hydride composition. Since their discovery in the 1980s the

number of complex transition metal hydrides increased and now in total over 80 compounds are identified [29].

Mg_2FeH_6, Mg_2CoH_5 and Mg_2NiH_4 are well known compounds as the member of this family of hydrides. As shown in Figure 1-5 they contain octahedral $[FeH_6]^{4-}$, square-pyramidal $[CoH_5]^{4-}$and tetrahedral $[NiH_4]^{4-}$anion complexes, respectively, that are surrounded by Mg^{2+}cations.

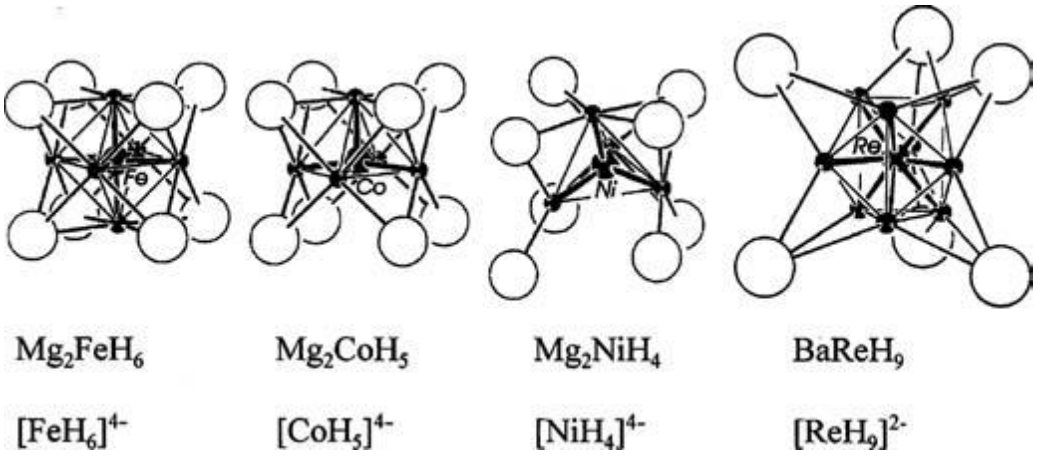

Figure 1-5. Metal–hydrogen complexes and cation environments in complex transition metal hydrides. Small filled circles: hydrogen; large open circles: $Mg^{2+}$and Ba^{2+} [29].

Mg_2FeH_6 is a material with a very high volumetric hydrogen capacity of 150 $g.L^{-1}$ and a gravimetric hydrogen capacity of 5.5 wt% H_2. With a decomposition temperature of 320 °C at one bar hydrogen, this material cannot be considered for room temperature or medium-temperature fuel cell applications. Dehydrogenation enthalpy of this compound is about 77 $kJ.mol^{-1}$ H_2 [47]. Low price precursor metals and excellent cycle stability over hundred cycles are known as the advantages of this compound. These properties could make the material useful for heat storage application in the temperature range around 450–500 °C, for example, for solar heat storage applications [22].

Lithium amidoborane

One of the most promising materials suggested as a potential Solid-state hydrogen store is ammonia borane (NH_3BH_3) with ~19.6 wt% hydrogen capacity. This material is

a stable solid at room temperature and pressure and is neither flammable nor explosive [48]. In the past decade, considerable attention has been given to NH_3BH_3 to improve its dehydrogenation problems such as borazine formation and lowering the reaction temperature less than water vapor temperature [49-51].

Cationic substitution on *AB* was first suggested by Xiong et al. [50] motivated by the earlier work on amide-hydride interactions which involved two oppositely charged H atoms. In their study, chemical compositional modification on *AB* was achieved by reacting alkali metal hydride (*LiH*) with *AB* during milling process [48]. Similar to amide-hydride reaction, the alkali metal hydride acts as hydride source while NH_3 in *AB* acts as proton source. In that reaction, cationic substitution of H^+ in *AB* with an electron donating metal (like Li^+) produces the new compound lithium amidoborane (*LiAB*), according to:

$$LiH + NH_3BH_3 \rightarrow LiNH_2BH_3 + H_2 \qquad 1\text{-}5$$

Non-isothermal decomposition of *LiAB* produces 10.9 wt% of H_2 at 91 °C, without borazine emission. In addition, the dehydrogenation enthalpy is reduced from -20 kJ.mol^{-1} H_2 (for *AB*) to -3 kJ.mol^{-1} H_2 (for *LiAB*), with a significant improvement of the dehydrogenation thermodynamics [50].

1.1.3.5 Nano confinement

The synthesis of phases in nanostructured form is a promising application of nano-technologies to the hydrogen storage field. Nanostructured materials (also referred to as “nanocrystalline” or “nano-phase” materials) are single-phase or multi-phase polycrystalline substances with the grains smaller than 100 nm [52].

Several experiments indicate that practically in all solid state hydrides, the kinetics and also the thermodynamics of hydrogen absorption/desorption can be modified by reducing the grain size of the compound [53, 54]. These observations were attributed to the high surface area to volume ratios, increased number of grain boundaries and reduced diffusion (nano-scales) distances exhibited by these nanostructured metal hydrides.

Improved hydrogen sorption kinetics was reported for MgH_2 [36, 54] and $NaAlH_4$ [55] nanostructures produced through high-energy ball milling. However this method is not suitable to prepare metal hydrides with crystallites sizes less than 10 nm. Moreover, nanostructured hydrides produced through ball-milling easily lose their nano sizing benefit due to the sintering and agglomeration of the nanoparticles during cycling.

A new method to overcome these limitations is nanoconfinement where the metal hydride nanoparticles are confined into a nanoporous scaffold material such as carbon, silica or MOF [39, 56]. These nanoporous scaffolds normally contain micropores (≤ 2 nm) and/or mesopores (2- 50 nm) and sometimes macropores (> 50 nm). As well the average size of the confined metal hydride particles can be tuned by changing the pore sizes of the scaffold.

Autrey *et al.* [57] for the first time successfully confined ammonia borane (NH_3BH_3) into ordered mesoporous silica (*SBA-15*) with a pore diameter of 7-8 nm and showed that the inclusion of the ammonia borane in this nanoporous silica resulted in a significant improvement on its hydrogen release properties. The first decomposition occurred 15 K lower in comparison with the bulk sample and the apparent activation energy for hydrogen release decreased from 184 kJ.mol^{-1}, in the bulk, to 67 kJ.mol^{-1} in the NH_3BH_3/*SBA-15* nanocomposite. Additionally, the decomposition pathway of NH_3BH_3 changed upon confinement, as a result of a significant suppression of the borazine ($B_3H_6N_3$) formation which is typically linked with hydrogen release from NH_3BH_3. Similar results were reported for confined NH_3BH_3 in nanoporous carbon cryogels scaffold [58]

In case of metal borohydrides, Gross et al. [59] confined $LiBH_4$ in nanoporous carbon aerogel by melt infiltration and showed that both the dehydrogenation kinetics and thermodynamic of $LiBH_4$ upon cycling were greatly improved in comparison to the bulk $LiBH_4$. Furthermore, unlike with bulk $LiBH_4$, no diborane was released during dehydrogenation.

Nanoconfinement continues to engender a lot of interest as offers a comparatively easy route to synthesize and stabilize nanostructured metal hydrides using nanoporous hosts as a template.

1.2 Synthesis of materials

1.2.1 Mg_2FeH_6 preparation

1.2.1.1 Ball Milling

The Mg_2FeH_6 component was synthesized according to the route employing magnesium hydride and iron as reagents [60, 61]. A 1.2 g sample of commercial MgH_2 and α-*Fe* (Sigma-Aldrich) in 2:1 molar ratio was loaded with ten 1 cm diameter stainless steel balls (ball-to-powder weight ratio = 30) into a 50 ml vial of the same material. The powder was ball milled in *Ar* atmosphere by a Retsch PM100 planetary mill for 30 h at 400 rounds.min^{-1}.

The sealed vial was then placed on a sun wheel with a counterweight employed to control the oscillations. The sun wheel acted as a rotating plate during ball milling and the vial moved in different direction in a 1:2 ratio.

1.2.1.2 Hydrogenation reaction

The ball milled sample was loaded in an automatic Sievert-type apparatus (0), brought to $p(H_2)$ =100 bar and then heated at 400 °C for various times (monitor mode). Several reaction times were employed: 3, 4, 6, 9 and 14 days, in each case analyzing the final product by X-ray diffraction.

1.2.2 Nanoconfined sample preparation

The preparation of aerogels starts with the synthesis of aqueous colloidal solutions during which the chemical and physical structures of a polymer take shape. Formaldehyde is responsible for the cross-linking of aromatic molecules, the resorcinol/formaldehyde (*R/F*) molar ratio must be $0.4<R/F<0.7$ [62]. Too high a quantity of the remaining formaldehyde induces the collapse of the mesoporous structure of gels, decreasing the pore volume of the aerogel synthesized. The lack of formaldehyde as a cross-linking reagent leads to a weak cross-linking between the

aromatic molecules and thus, no proper gels are formed [63]. With increasing amount of the catalyst the size of particles decreases and the velocity of gelation increase [64].

The overall concentration of reagents in water is usually expressed by a molar ratio of resorcinol/water (*R/W*), which reflects the amount of the solid fraction in the gel. At a given catalyst concentration an increase of the amount of the solid fraction (*R/W*) leads to the formation of smaller pores and a faster gelation. For gel preparation either a basic or acid catalysis alone could be used, but the doubly catalyzed synthesis utilizing both of them is considered to be the most effective [65]. Besides hydroxides, carbonates have also been used as basic catalysts [66]. The typical gelation temperatures used in case of resorcinol gels were in the range of 50-90 °C .As the temperature increases, the rate of gelation increases as well [67].

Principally, a gel is composed of two phases, viz. a liquid phase filling the pores, and a solid phase. In order to obtain porous materials, the liquid phase has to be removed without a significant shrinkage of the solid material [68].

The main factors involved in the drying process of the gel are the solvent exchange and the drying conditions. The most common variations of the drying conditions are subcritical drying, supercritical drying and freeze drying, which produce xerogels, aerogels and cryogels, respectively [69, 70].

The resorcinol formaldehyde xerogels, were prepared by mixing selected amounts of resorcinol (Aldrich, 99%), formaldehyde in water (37 wt % stabilized by ~10–15% methanol, Merck), deionized water, and Na_2CO_3 (Aldrich, 99.999%) in a beaker with continuous stirring. The *pH* value of the final solution was recorded. The selected amounts are reported in Table 1-3.

Table 1-3. Reagents used for synthesis of resorcinol formaldehyde xerogels.

Sample name	m. Resorcinol (g)	V. Formaldehyde (mL)	V. Water (mL)	m. Na_2CO_3 (g)	R/W %	R/F
CX1	25	33.5	38.0	0.0144	35.0	0.5
CX2	25	33.5	38.0	0.0211		
CX3	25	33.5	38.0	0.0274		

Once prepared, solutions were transferred to 300 mL polypropylene container, sealed, and treated one day at 23 °C, one day at 50 °C, and three days at 90 °C. The samples were then cooled, immersed in acetone to displace the water for 3 days. The acetone bath was poured off and refilled every day and then cut into cubes (0.45 cm/side) (Figure 1-6). The aerogel cubes were allowed to dry in air and then heated in a tube oven under nitrogen from room temperature to 800 °C at 2 °C.min^{-1} and maintained at 800 °C for 6 h to pyrolyze the resorcinol-formaldehyde gel. In two cases the activation was carried out at 900°C in a continuous flow of CO_2 for 4 hours.

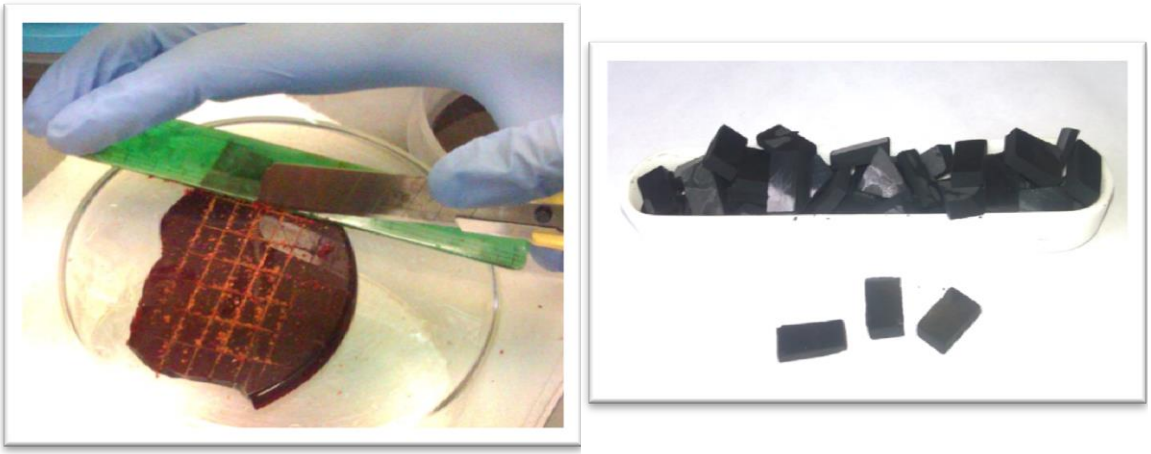

Figure 1-6. Cutting the samples to small cubes before heat treatment and final heat treated xerogel cubes.

The impregnation of iron/cobalt was carried out on final heat treated carbon xerogels (P1 and P2) by (I) dissolving 2.01/1.44 g $Fe(NO_3)_3.9H_2O/Co(NO_3)_2.6H_2O$ (Aldrich) in 5 mL deionized water (II) immersing 0.5 g carbon xerogel in

nitrate solution overnight. The infiltrated gels removed from the solution and loaded into an autoclave to remove water and decompose the metal nitrate to oxide under vacuum at 400 °C. All surfaces of the samples were scratched by abrasive paper (1000 girt) to remove the oxides remained on the surfaces of xerogel. The infiltrated oxide was reduced to metallic form with hydrogen at 100 bar H_2 in 500 °C for 8 hours inside the autoclave.

Table 1-4 reported the BET values of two different carbon xerogels used for uptake investigation on *Mg*, *Fe* and *Co* compounds.

Table 1-4. BET values of carbon xerogels used for uptake study.

Sample name	initial pH	S_{BET} (m^2/g)	V_{micro} (cc/g)	V_{meso} (cc/g)	D_{max} (nm)	V_{tot} (cc/g)
P1	6.06	661	0.149	1.05	21	1.24
P2	5.77	634	0.174	0.88	39	1.09

1.3 Characterization methods

1.3.1 X-Ray Diffraction

Laboratory X-ray Diffraction

X-ray diffraction is a universal and non-destructive technique for characterizing crystalline materials. The method is used to obtain information about crystallographic structures, chemical composition and some physical properties of the investigated samples. In X-ray diffraction, electromagnetic radiation with wavelength in the order of typically 1.54 Å elastically scatters on the electron cloud of the atom in a crystal. The wave-like character of the X-rays causes the scattered X-rays to interfere constructively or destructively, depending on the X-rays wavelength λ and the distance between lattice planes of atoms, in the crystal structure. The interference of these waves follows Bragg`s law

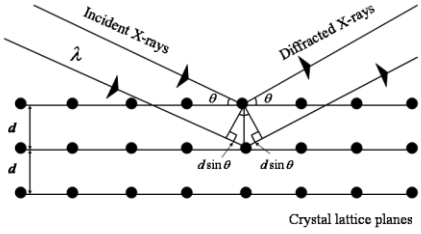

Figure 1-7. Diffraction of incident X-rays from the family of parallel atomic planes.

$$n\lambda = 2dsin\theta \qquad 1\text{-}6$$

Where: n = integer, λ = wavelength, θ = angle between the incident beam and diffraction plane, d = lattice spacing.

A Bruker D8 Advance X-ray powder diffractometer (Bragg-Brentano μ-μ geometry and Cu-Kα radiation), equipped with secondary beam monochromator, operated at 30 mA and 40 kV was used for all ex-situ diffraction measurements. XRD patterns were

collected using step scans, with a step size of 0.02° (*2θ*) and a count time of 18 s per step.

All samples were always protected from air in a special holder (Figure 1-8) covered with Kapton film; this was displaced from the diffraction plane, so as to avoid polymer contribution to the recorded pattern.

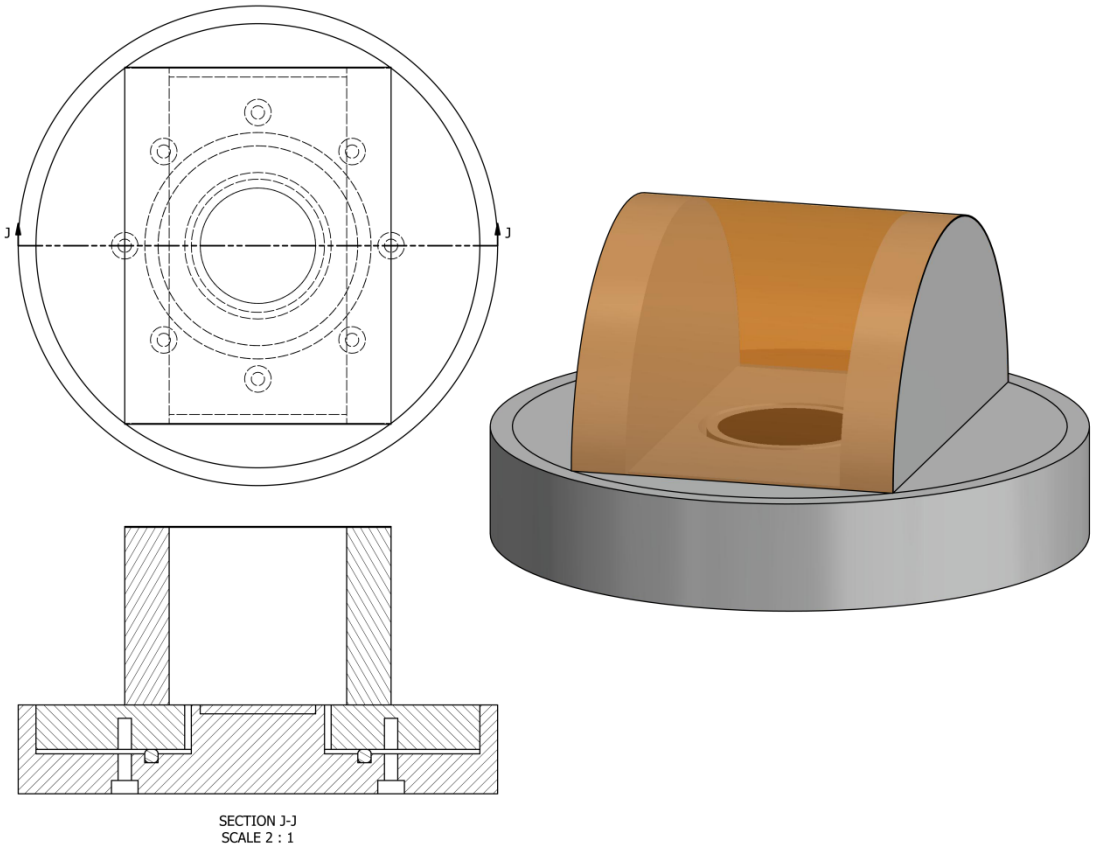

Figure 1-8. Laboratory XRD sample holder with protective atmosphere.

Synchrotron X-ray Diffraction

Synchrotron source X-rays are generated by accelerating electrons or positrons to near the speed of light around an evacuated, magnetized ring. These particles produce electromagnetic radiation when under the influence of an accelerating field; the wavelength and energy of which is proportional to the velocity of the particles.

In-situ synchrotron radiation powder X-ray diffraction (SRPXD) measurements were performed at the beamline I711 of the MAX II (Lund, Sweden)facility and the beam line P02.1 of the PETRA III (DESY, Hamburg) facility. Both high resolution diffractometer used the Debye-Scherrer geometry with X-ray monochromators: the selected wavelength for data collection were λ = 0.99242 Å with a Mar165 CCD detector [71], at MAX II, and λ = 0.2072 Å with a 1621 N ES detector [72], at PETRA IIII.

The sample was loaded into airtight sapphire capillaries in a glove-box under an argon atmosphere. During the experiments the sample pressure can be adjusted. The sample temperature was recorded by a thermocouple inserted into the powder-bed. The system was heated by a tungsten coil and was controlled with an external PID regulator. A schematic diagram of the experimental setup is shown in Figure 1-9 [73]. The applied heating rates and pressures are noted in the each experiment.

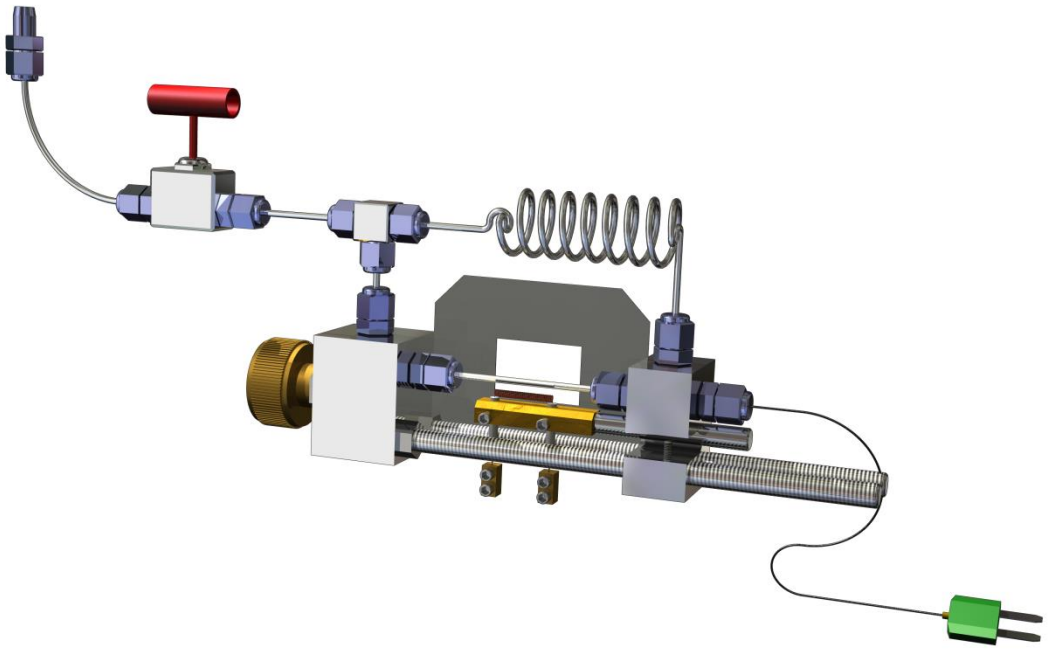

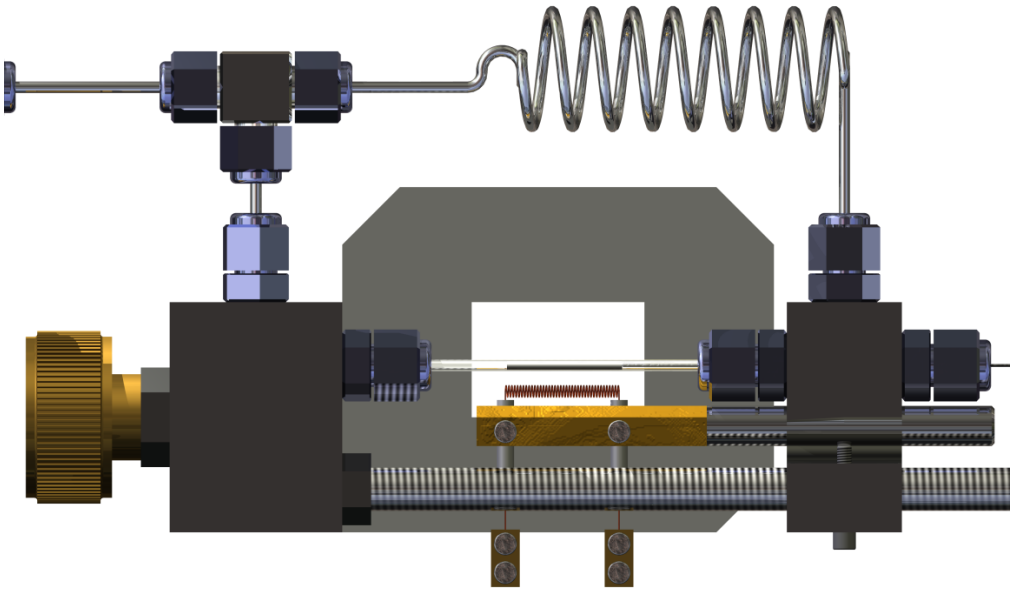

Figure 1-9. High pressure sample holder used for in-situ synchrotron data collections.

The FIT2D software was used to read the areadetector frames (Figure 1-10-a), to integrate the peaks and export the pattern as 2θ - Intensity format (ASCII format) [74].

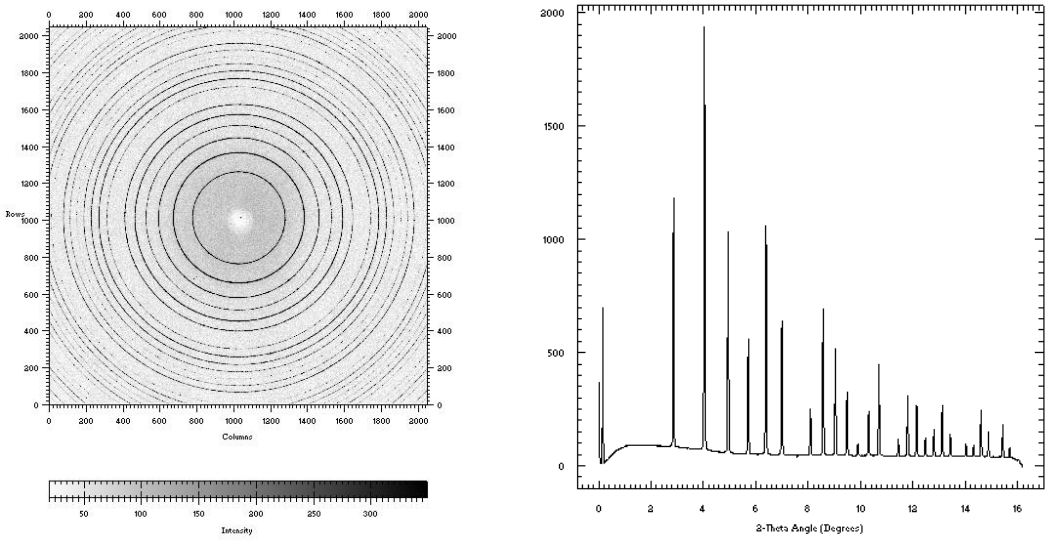

Figure 1-10- LaB_6 diffraction pattern, recorded at DESY, Hamburg (λ=0.2072Å) used for calibration. (a) Image recorded by areadetector and (b) integrated pattern calculated by FIT2D software.

1.3.2 IR spectroscopy

IR spectroscopy is a very useful method for identification of materials without long range crystalline order.

The energy of infrared radiation is of the order of the energy required for the vibration of chemical bonds. If the energy of the incident photon corresponds to the energy gap between the vibrational ground state of a molecule and an excited state, the photon may be absorbed to excite the molecule to a higher vibrational state. The IR spectrum is a result of these transitions between vibrational energy states.

The vibrational spectrum is unique and characteristic for each molecule therefore can be used as a fingerprint for identification of the unknown structure by comparison with previously recorded reference spectra.

In this work, infrared spectra were recorded by a JASCO FT/IR-4100A spectrophotometer in the 400 to 4000 cm^{-1} wavenumber range (2 cm^{-1} resolution). The powder sample was mixed with nujol and inserted between two *KBr* windows, sealed externally in glove box for air protection.

1.3.3 Thermal Analysis and BET

A Setaram Sensys Evo differential scanning calorimeter (horizontal position) coupled with a Hiden Analytical quadrupole mass spectrometer (MS) under a constant flow (28 $mL.min^{-1}$) of ultrahigh-purity argon (99.999% Air Liquide) was used as simultaneous thermal analysis - mass spectroscopy (STA-MS). A powdered sample (<20 mg) was placed in an Al_2O_3 crucible with lid. Loading of the samples was performed without air contact in a glovebox and transferred to the machine in sealed container. The loaded samples were purged with Argon for at least 1h and then heated in the temperature range 25–550 °C ($\Delta T/\Delta t$ = 1 $°C.min^{-1}$). During the experiment the MS signals at *m/e* = 2, 18 and 32 were recorded in order to detect H_2, H_2O and O_2. No significant quantity of H_2O or O_2 was detected.

The BET method for assessing the specific surface area is widely known to be essentially erroneous when looking at microporous materials. However, it is also a widely used tool in the literature for comparison of these types of materials.

N_2 adsorption–desorption measurements were carried out using a Nova 2000e surface area and pore size analyzer from Quantachrome. Prior to the measurements, a known amount of sample was degassed at 200 °C under vacuum for several hours. All samples were measured with a full adsorption and desorption isotherm in the pressure range of 0–1 p/p_0 at liquid nitrogen temperatures (77K) with nitrogen gas as an adsorbent. The measurement was programmed to continuously change the pressure ratio to 1 for adsorption, and to 0 for desorption. Data were analyzed by the t-plot method [75, 76], the Brunner Emmet Teller (BET) method [77], and the Barret Joyner Halenda (BJH) method, and the highest point of the isotherm measurement (where $p/p_0 \sim 1$) was used to calculate the total volume of the sample [78].

1.3.4 The Gas Reaction Controller Sievert's Apparatus

All thermodynamic and kinetic studies (PCI, TPD and SOAK) were performed inside Gas Reaction Controller (GRC), a fully automated Sievert-type Apparatus produced by Advanced Material Corporation (850 Poplar St., Pittsburgh, PA 15220 U.S.A.).

Layout of GRC

The GRC system's layout is illustrated in Figure 1-11. The sample is placed inside “Sample CH1”. The sample holder is an L shape stainless steel tube placed inside a cylindrical furnace. It contains the sample container which is a little stainless steel cylinder (internal volume equal to 4 cc) and one thermocouple (TC1) placed exactly in the middle of sample container; that sample holder connects to the internal part which is inside the main system box and hosts the HP1 pressure transducer.

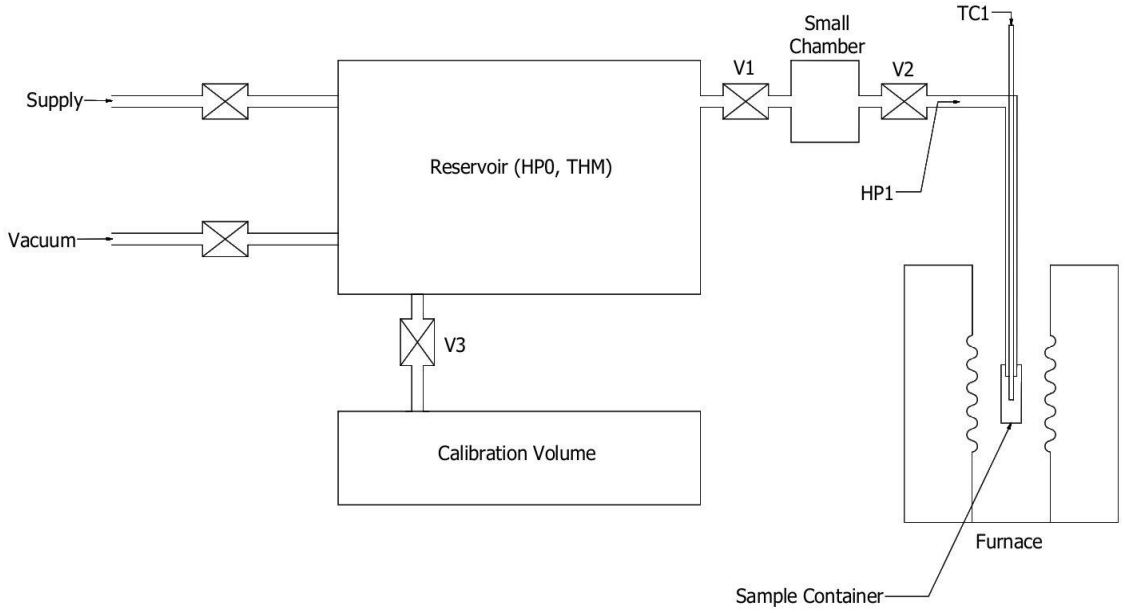

Figure 1-11. Gas Reaction Controller Sievert's Apparatus layout.

Soak mode

This mode is used for studying reaction kinetics in isothermal and isobaric condition. The desired temperature is set to a certain value, and heating or cooling is performed under a constant low/high hydrogen pressure to keep the sample in dehydrogenated/hydrogenated state. When the set temperature has been attained, the system fills the sample chamber with a specified pressure of gas, which is calculated on the basis of the present HP0 and HP1 values taking into account the volume and temperature of each chamber; then a record of pressure and temperature is periodically kept during the reaction.

In this mode the hydrogen pressure on the sample is not strictly constant. During the reaction the system periodically opens the V1 and V2 valves together trying to compensate the released/absorbed hydrogen gas by equalizing HP0 and HP1 to keep the actual pressure as near to the starting pressure as possible.

If the dehydrogenation/hydrogenation reaction occurs at high pressure values, the $\Delta p = p - p_{int.}$ is negligible; on the other hand, in case of low pressure reactions this value can be considerable. In these cases it would be better to assume the average pressure over all points as the nominal pressure for that run.

In the soak mode the run will last for the preset running time. It is worthwhile to notice that in this system the maximum number of points is 2000, and if a reaction lasts more than 2000 min one has to set to command line to be able to record all data.

Pressure composition isotherm modes (PCI)

Two PCI modes are available:

PCI Desorption Mode (PCId) and PCI Absorption Mode (PCIa).

With these modes the system changes the pressure on the sample step by step at a constant temperature.

The system checks the experimental parameters every minute recording these "non-equilibrium data points" in a separate file (*.neq); if reaction is taking place thesystem will observe a pressure (HP0) change in last 10 minutes "d*p*/d*t"*; this change is compared tothe preset threshold d*P*: if

$$\frac{dp(HPO)}{dt} > \frac{dP}{10\ min} \qquad 1\text{-}7$$

the system considers that the reaction is still running and will not add or remove any gas till the settling condition is fulfilled or it will wait for a certain period of time which is called "Maximum Waiting Time, (t_{max})". When the settling condition is satisfied the system records all the experimental parameters as "equilibrium point" and proceeds to the next target pressure.

The measurement's primary terminating condition is reaching the specified final pressure (p_f) on the sample.

The range of pressure settling condition is 0.1-0.01 bar; a low *dP* value increases the resolution of the pressure plateau and is useful in case of reactions with slow kinetics. The total measurement time can be in the order of days.

The procedure of the PCI mode can be summarized as follows:

1. Reach the desired temperature at the starting pressure (p_0).
2. Set the *dP* and t_{max} values according to the reaction kinetics.
3. Set the final pressure (p_f) as terminating condition.
4. The system will calculate the step size (Δp) between subsequent points depending on $p_o - p_f$ and the selected resolution. These steps are not all equal for the whole PCI run; at higher pressures the step sizes are larger because of some technical design. This value can be changed during the run in the advance control panel if required.
5. As one can see in Figure 1-12, for each non-equilibrium set of points the hydrogen release rate decreases, till the termination condition is fulfilled because the total pressure change in the last ten minutes (*dp/dt*) becomes smaller than *dP*/10, or the time spent for the set of points reaches t_{max}. The system considers the last point as the equilibrium point for the set, and it reduces the sample pressure by opening the V2 valve. The new pressure (p_s) is lower than that at the previous point, because the pressure in the small chamber before the V2 opening was lower.
6. During the run, every minute V1 and V3 open to equalize the pressure in the reservoir and the calibration and small chambers. This pressure value (HP0) is controlled by the system to apply the predetermined pressure difference (Δp) on the sample after the opening of V2.
7. In the next non-equilibrium set of points V1 and V3 open again, and the pressure of the small chamber is set back to HP0. In this case HP0 is slightly higher than its previous value.

Three types of plateau can be observed during PCI measurements:

- Nearly flat plateau:
- Nearly flat plateau:
    - The pressure difference between starting and final equilibrium points is about 2 bar.
    - This kind of plateau is usually observed when the reaction kinetics is fast and the *dP* condition is satisfied (Figure 1-15). For example, the decomposition plateaus of MgH_2 are roughly flat.
    - The applied pressure difference at each point is roughly equal to that of the released hydrogen, so that the final equilibrium point for each set remains at a constant pressure (Figure 1-14).

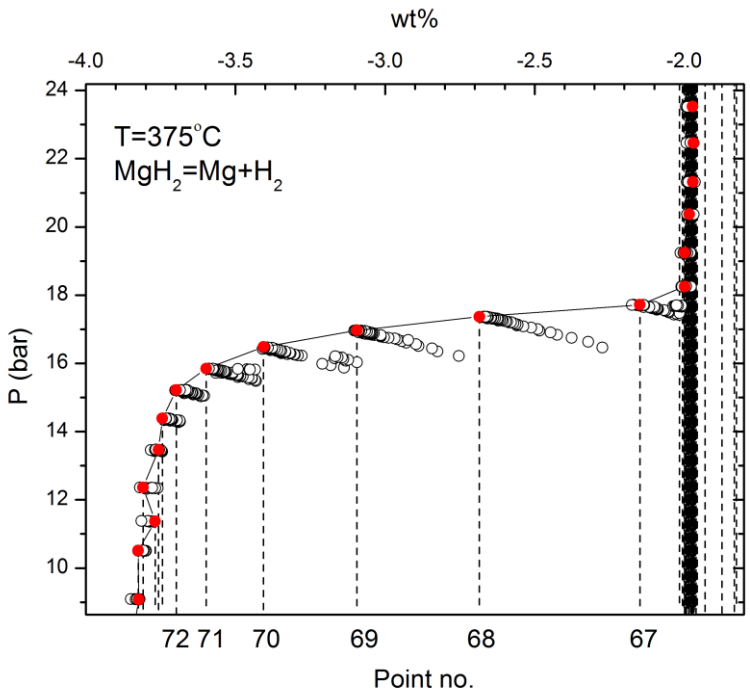

Figure 1-12. Non-equilibrium (open circles) and equilibrium (full circles) set points along a flat plateau.

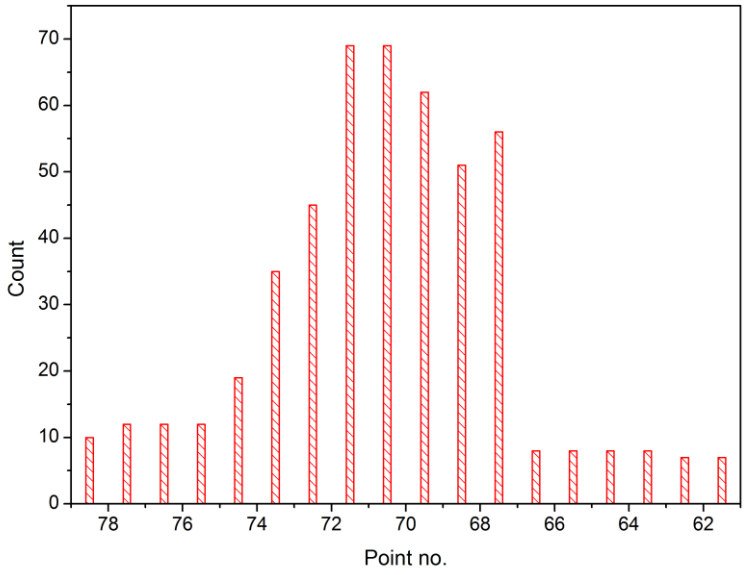

Figure 1-13. Histogram showing the number of non-equilibrium points for each dataset along a flat plateau (t_{max}=120min).

- Inclined plateau
  - The pressure difference between starting and final equilibrium points may be about 10 bar.
  - In this case the pressure of the released hydrogen at each point is much lower than the applied Δp .Reaching t_{max} always acts as terminating condition. This occurs for reactions with slow kinetics. As it can be seen in Figure 1-15 the number of non-equilibrium points is equal to t_{max} divided by the recording period time.
  - To have a better plateau, one can change Δp manually to lower values or increase the maximum waiting time.

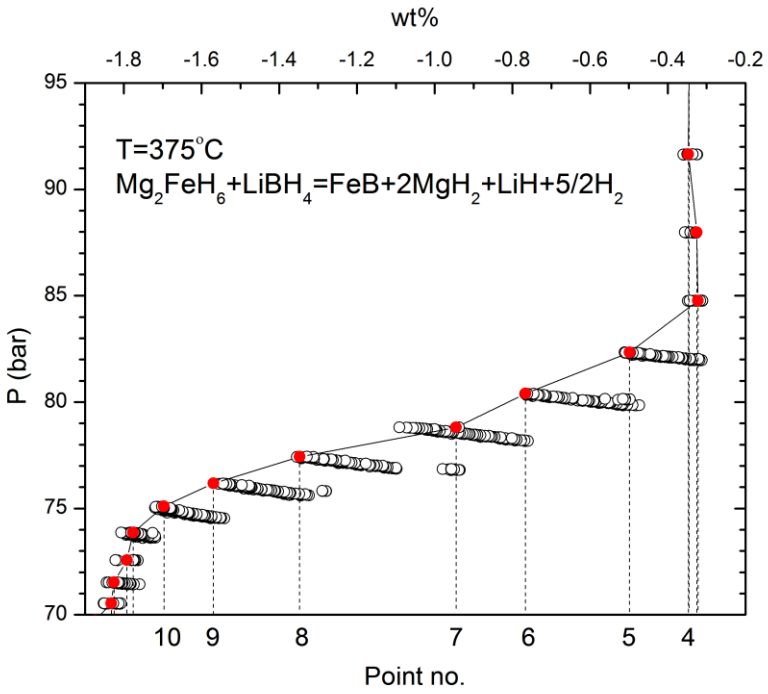

Figure 1-14. Non-equilibrium (open circles) and equilibrium (full circles) data showing an inclined plateau.

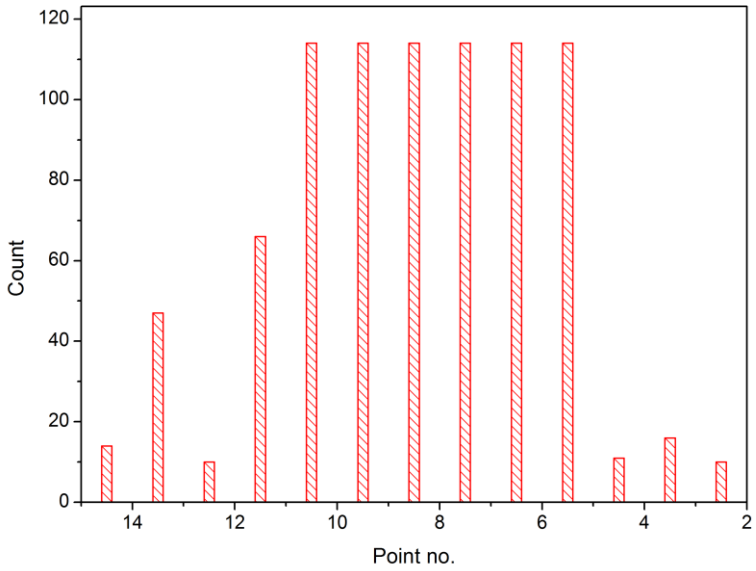

Figure 1-15. Histogram showing the number of non-equilibrium points for each dataset along the inclined plateau (t_{max}=120 min).

- Bumpy plateau
    - The situation observed is sometimes exactly opposite to that of the inclined plateau, i.e. the applied Δp is low and the hydrogen release is large (Figure 1-16). Therefore the pressure of the equilibrium point of each non-equilibrium set is lower than that of the next equilibrium point. In this case in the first half of the reaction an inclined plateau with opposite slope will appear, but in the second part the pressure of equilibrium points will decrease again.

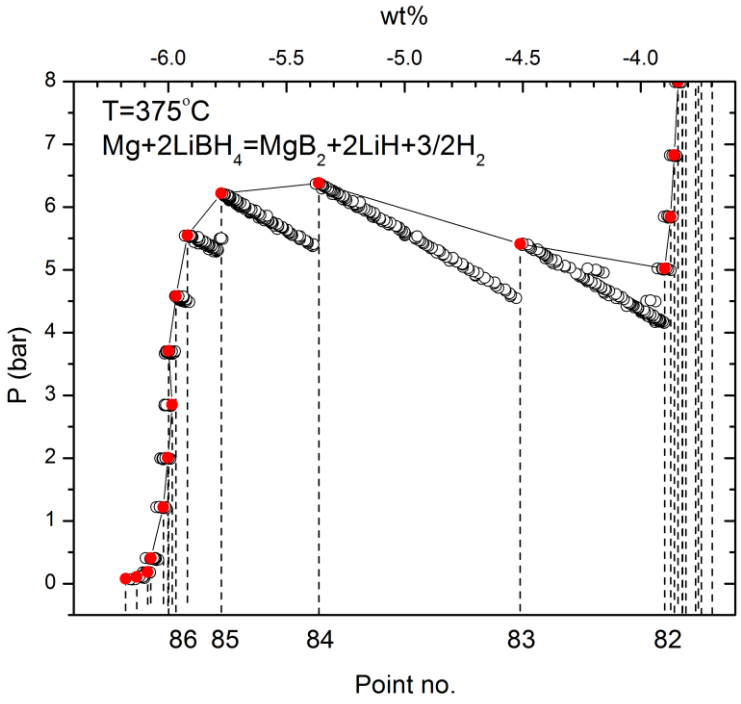

Figure 1-16. Non-equilibrium (open circles) and equilibrium (full circles) data showing a bumpy plateau.

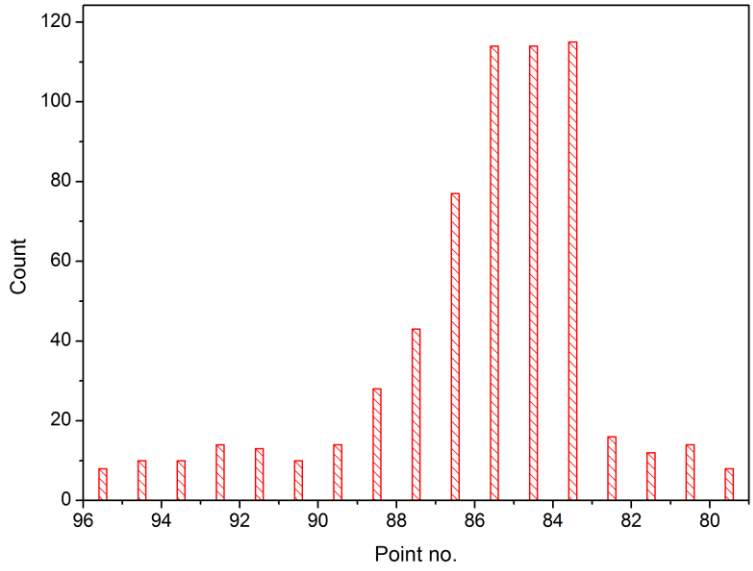

Figure 1-17. Histogram showing the number of non-equilibrium points for each dataset along the bumpy plateau (t_{max}=120 min).

Monitor mode

In monitor mode the system periodically records pressure, temperature, and amount of absorbed/desorbed gas as a function of time. This mode is used for some hydrogenation applications where the exact amount of pressure is not so critical. In this mode the system does not perform any operation but to change the sample temperature, possibly according to a temperature ramp, and all valves are kept closed.

During a monitor run, the pressure increase due to thermal expansion is taken into account by the software to correct the calculation of wt% H_2; because of the small final volume (closed valves) this mode is more sensitive to small hydrogen releases in comparison with the soak mode (where V1 and V2 open every minute). For this reason, this mode is used for temperature programmed decomposition (TPD) measurements.

1.4 Results and Discussion

1.4.1 $2LiBH_4$-Mg_2FeH_6 composite

1.4.1.1 Purity of Mg_2FeH_6

X-ray measurements on the ball milled $2MgH_2 + \alpha Fe$ powder (Figure 1-18-a) showed the presence of Mg_2FeH_6 and alpha-iron only, without traces of either MgH_2 or Mg. Thus, all magnesium hydride was consumed in the $6MgH_2 + 3Fe \rightarrow 2Mg_2FeH_6 + 2Mg + Fe$ reaction; the residual Mg was not observed because it was possibly in nanocrystalline state or remained inside milling vial by sticking to the wall and balls surface.

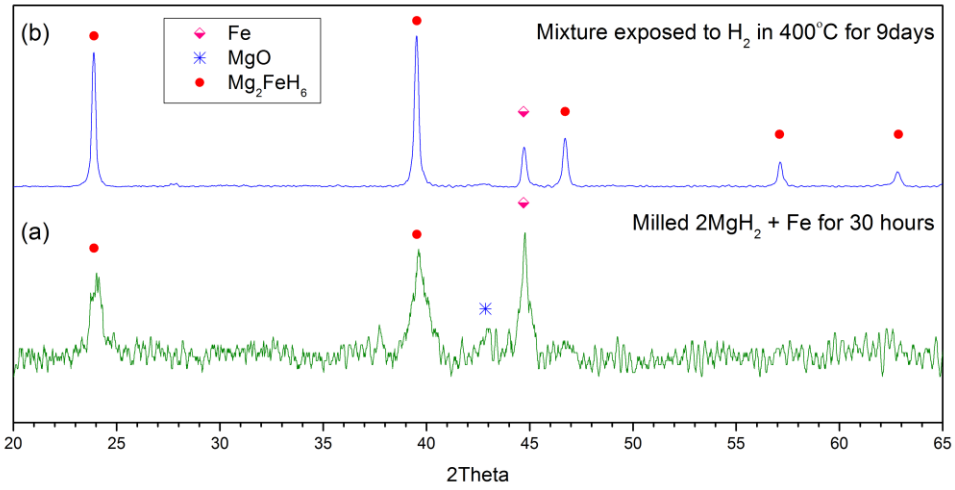

Figure 1-18. X-ray diffraction pattern (Cu-Kα radiation) of the milled for 30 hours (a) and exposed to H_2 in 400°C for 9days (b) sample

After the hydrogenation step in the Sievert apparatus, again the sole presence of Mg_2FeH_6 and of a variable quantity of α-Fe (clearly decreasing with synthesis time) could be detected in the X-ray data (Figure 1-18-b). The amount of iron dropped from the 3 to the 4 days run, and then decreased very slowly to a constant value after 9 days. Thus, the direct synthesis reaction $2Mg + Fe + 3H_2 \rightarrow Mg_2FeH_6$ was not complete in the Sievert equipment, leaving a fraction of not reacted Fe in the sample; this agrees

with what reported in previous work on the magnesium iron hydride system [60]. On the other hand, the small quantity of *Mg* left did not react directly with hydrogen to form magnesium hydride, but it cannot be detected in the X-ray pattern because presumably in nanocrystalline or non-crystalline form.

The relative Fe/Mg_2FeH_6 amount was determined by means of two-phase Rietveld refinements (GSAS/EXPGUI computer package [79]). For 9-days synthesized Mg_2FeH_6, a weight composition of 5.8(1) % *Fe* and 94.2(1) % Mg_2FeH_6 was obtained, corresponding to a Fe/Mg_2FeH_6 weight ratio of 0.062. The refined cubic unit-cell parameters were a = 6.4435(3) and 2.8611(2) Å for Mg_2FeH_6 (space group *Fm-3m*) and α-Fe (space group *Im-3m*), respectively. Final values of the agreement factors: R_p=0.127, wR_p=0.160, reduced χ^2=1.9.

A TPD run was performed on the Mg_2FeH_6 sample in the Sievert apparatus under 3 bar of hydrogen pressure (Figure 1-19-a).

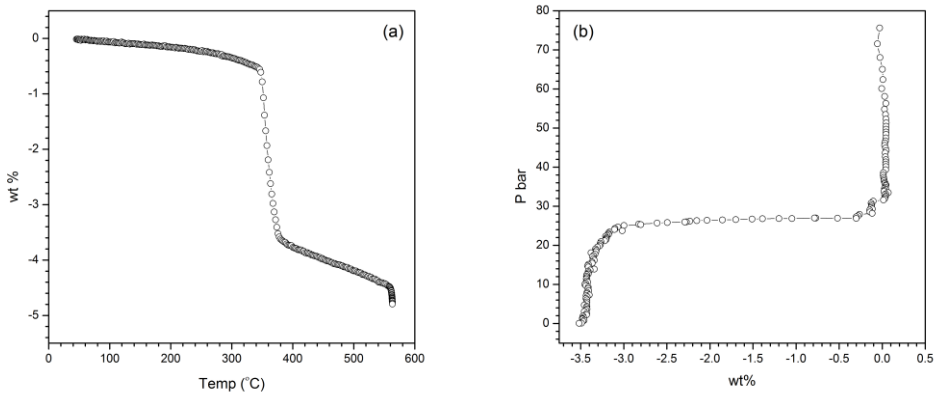

Figure 1-19. TPD (a) and PCI (b) measurements on synthesized Mg_2FeH_6.

The inflexion point of the decomposition profile was located at 350 °C, and a total H_2 release of 4.8 wt% up to 550 °C was observed. This compares well with the expected value of 4.9%, obtained from the ideal H_2 yield of 5.47 wt% of pure Mg_2FeH_6 by correction for the iron and magnesium impurities content.

$$Mg_2FeH_6 \rightarrow Mg + 3H_2 \qquad 1\text{-}8$$

A PCI run was also done on that sample at 425 °C to check the presence of MgH_2 in the synthesized sample, which possibly decomposed together with Mg_2FeH_6 in the TPD measurement. The result (Figure 1-19-b) presents only a plateau at 26.6 bars, corresponding to the decomposition pressure of Mg_2FeH_6 reported for that temperature [47].

1.4.1.2 Phase identification during dehydrogenation process

The 2:1 nominal molar ratio was selected for the $LiBH_4/Mg_2FeH_6$ system, in order to study all multiple dehydrogenation steps of $LiBH_4$ reacting with subsequent products of previous reactions. The theoretical hydrogen yield of Mg_2FeH_6-$2LiBH_4$ is 7.85wt% H_2, considering that not decomposed LiH should be present in the final product. This can be an attractive value for many applications, in case it is coupled to a decreased dehydrogenation temperature with respect to that of pure $LiBH_4$.

Isothermal (PCI) H_2 desorption experiments were performed at eight temperatures in the 325-550 °C range. The results of four of them are reported in Figure 1-20.Three pressure plateaus can be observed in all desorption experiments, indicating distinct dehydrogenation reactions which are denoted as A, B, and C in the decreasing pressure order. The A process was not observed in the isotherms at T> 400 °C, because the maximum applied pressure of about 100 bar was not sufficient to prevent the reaction from occurring already during the heating step. The A dehydrogenation reaction is the most demanding one kinetically: over 2 h waiting time was necessary for the equilibration at each pressure step, whereas about 0.5 and 1.5 h was sufficient on the average for the B and C processes, respectively.

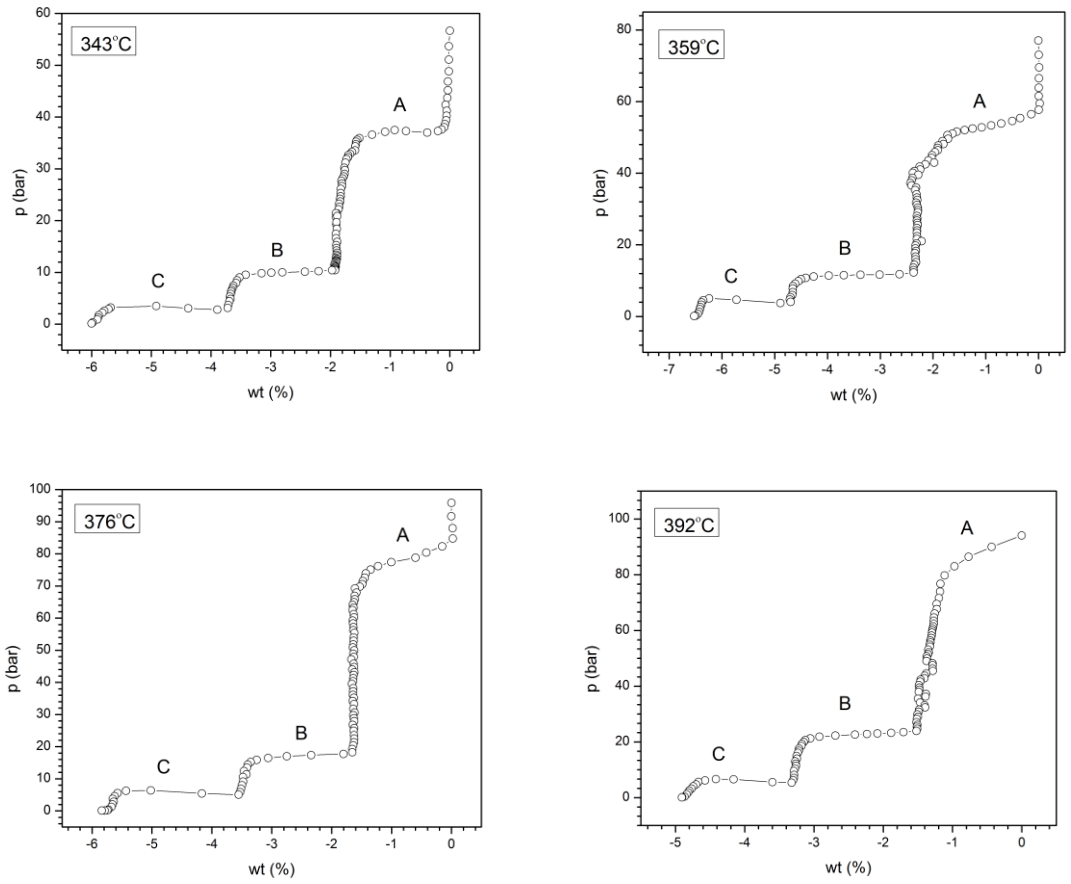

Figure 1-20. PCI (Pressure-Composition-Isotherm) results on the $2LiBH_4$-Mg_2FeH_6 system for four different isotherms. A, B and C denote pressure plateaus corresponding to three distinct desorption steps

The results of TPD measurements, performed in the Sievert's apparatus with 1 C.min^{-1} heating ramp, are shown in Figure 1-21. Three curves were recorded at 3, 20 and 80 bar of hydrogen pressure. In the 3 bar data the A and B processes are not resolved but merged in a single inflexion point at 345 °C. At higher pressures, on the other hand, the inflexion point splits clearly into two ones corresponding to A and B reactions (376 and 402 °C at 20 bar, 411 and 472 °C at 80 bar). The C reaction appears only in the 3 bar experiment (at 460 °C), whereas it moves above the upper *T* limit of the experimental setup (550 °C) in the high pressure runs. On comparing the TPD pairs of *p*-*T* values for each reaction with the corresponding PCI results, lower *p*/higher *T* values are observed as expected, due to the large hysteresis effects of the dynamic thermal ramp mode even with low heating rate. The qualitative agreement is however

good, confirming the sequence of reactions determined by the more accurate isothermal mode.

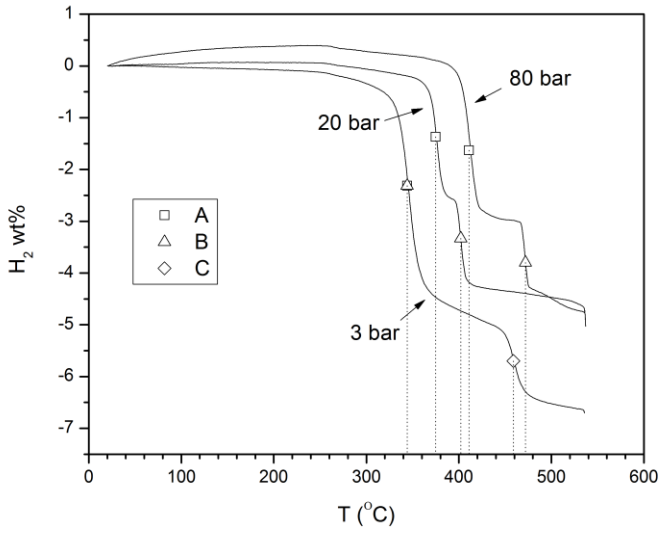

Figure 1-21. Dynamic thermal decomposition of *2LiBH$_4$-Mg$_2$FeH$_6$* under variable hydrogen pressure (heating rate 1 °C.min^{-1} in Sievert apparatus). Inflexion points denoting the subsequent steps of the reaction are indicated by corresponding symbols.

Simultaneous thermal analysis (STA) in flowing N_2 and 2°C.min^{-1} heating ramp was done on the *2LiBH$_4$-Mg$_2$FeH$_6$* composite (Figure 1-22). The Differential Scanning Calorimeter (DSC) pattern showed three peaks at 112, 280 and 356 °C. The first two can be tentatively interpreted as *LiBH$_4$* polymorphic transition (orthorhombic to hexagonal), and melting process. The third broad peak, confirmed also by the thermogravimetric and hydrogen mass spectroscopy patterns, is interpreted as due to the simultaneous A and B reactions (cf. (1-9) and (1-10); its temperature value agrees with results from TPD data. On the other hand, no traces are seen of the C reaction, probably because with those experimental conditions it would occur beyond the maximum temperature reached.

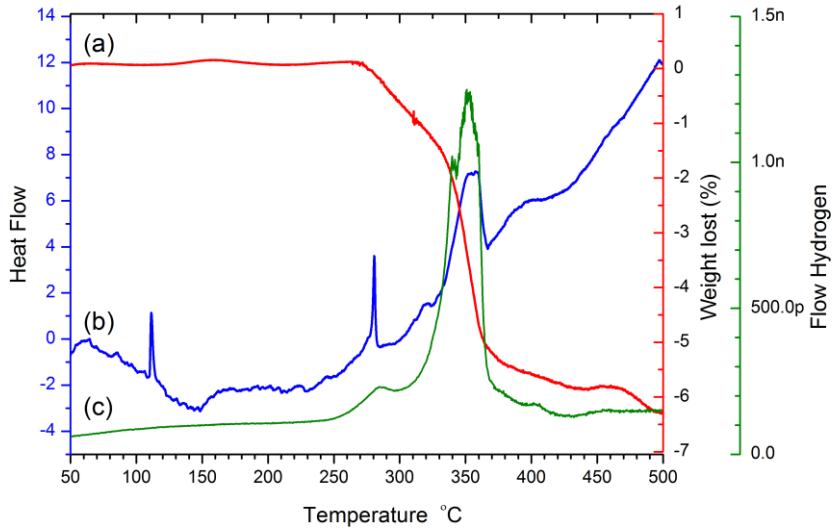

Figure 1-22. Thermal analysis of $2LiBH_4+Mg_2FeH_6$ in flowing N_2 (2 °C.min^{-1} heating ramp).Thermogravimetric analysis (a), differential scanning calorimetry (b), hydrogen mass spectrometry (c).

Ex-situ X-ray assisted phase identification

In order to identify the solid phases produced in the PCI experiments, in the runs at 375 °C (Figure 1-23) and at 345 °C (Figure 1-24) the hydrogen desorption reaction was interrupted after the A and B steps, the sample holder was quenched in water, and laboratory X-ray powder patterns were recorded. X-ray data were collected at the beginning (before A) and at the end (after C) of desorption, too.

In another experiment at 345 °C FTIR spectra were collected on the samples obtained after A and B in desorption mode, and after the B+C reaction in absorption mode.

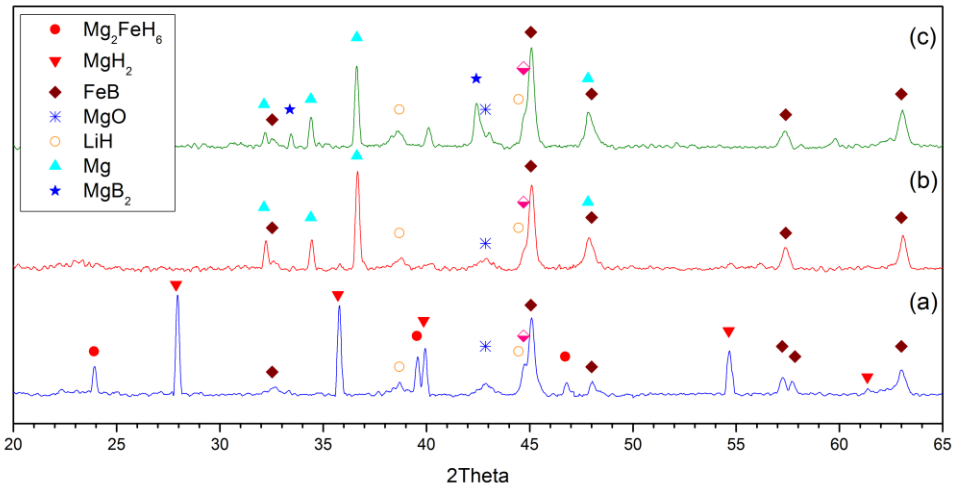

Figure 1-23. X-ray diffraction patterns (Cu-Kα radiation) of the subsequent products of dehydrogenation of the *2LiBH$_4$-Mg$_2$FeH$_6$* composite after reactions A (a) and B (b), and the final product after reaction C (c), as obtained by PCI experiment at 375 °C.

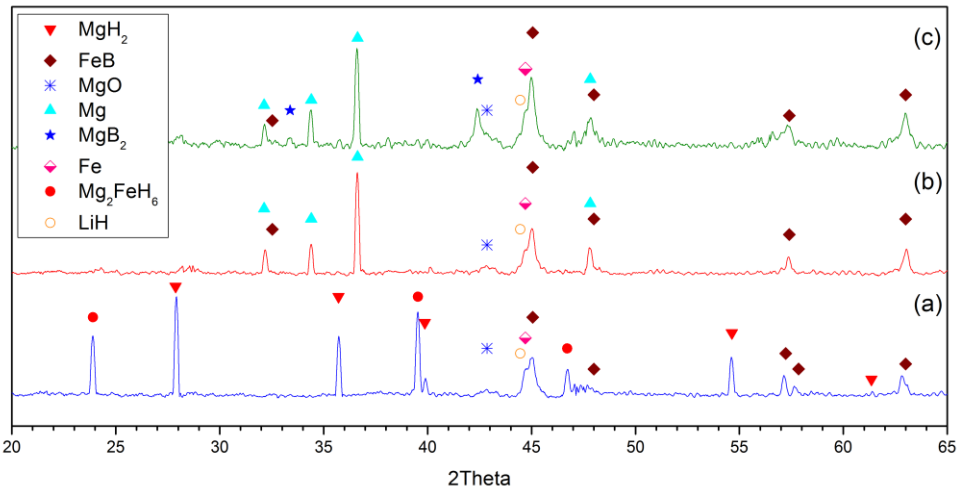

Figure 1-24. X-ray diffraction patterns (Cu-Kα radiation) of the subsequent products of dehydrogenation of the *2LiBH$_4$-Mg$_2$FeH$_6$* composite after reactions A (a) and B (b), and the final product after reaction C (c), as obtained by PCI experiment at 345 °C.

The X-ray results of the experiment at 375 °C are shown in Figure 1-23; those obtained at 345 °C are the same. After reaction A, *MgH_2*, *FeB* and *LiH* are formed as

products. This proves that $LiBH_4$ indeed reacts with Mg_2FeH_6 during this dehydrogenation process. Thus, the most probable reaction occurring during process A is as follows:

$$2Mg_2FeH_6 + 2LiBH_4 \rightarrow 2LiH + 4MgH_2 + 2FeB + 5H_2 \qquad 1\text{-}9$$

A small amount of residual Mg_2FeH_6 appears among the products (Figure 1-23-a), indicating that when the sample was taken out of the Sievert device (just at the end of the A horizontal plateau) the reaction was not fully completed yet.

The B process can be interpreted unambiguously as the dehydrogenation reaction of MgH_2, as the Bragg peaks of magnesium hydride disappear after B and are replaced by those of *Mg*:

$$MgH_2 \rightarrow Mg + H_2 \qquad 1\text{-}10$$

No role should be played by $LiBH_4$ in this process, because MgB_2 is not formed.

In the final product of dehydrogenation, in addition to the previous H-free compounds also the new Bragg peaks of MgB_2 are observed. This proves that in the C step the residual amount of $LiBH_4$ has reacted with *Mg* according to:

$$2LiBH_4 + Mg \rightarrow 2LiH + MgB_2 + 3H_2 \qquad 1\text{-}11$$

A reaction of $LiBH_4$ with MgH_2 can be excluded, because magnesium hydride had disappeared after the B step.

At variance with the $LiBH_4$+MgH_2 system, the dehydrogenation thermodynamics of the $LiBH_4$+*Mg* assemblage is not reported as such in the literature. Only the catalytic effect of *Mg* on the lithium borohydride decomposition was studied [80]. However, reaction (1-11) was reported to occur [81] as the second part of the two-step dehydrogenation of $LiBH_4$+MgH_2, after decomposition of MgH_2 into *Mg*+H_2. Indeed, the second step was shown to follow route (1-11) at higher pressure when sufficient equilibration time is provided, whereas when pressure is reduced quickly to a lower value *Mg* would not be involved in the reaction, but the alternative route $2LiBH_4 + Mg \rightarrow 2LiH + Mg + 2B + 3H_2$ would be followed [82]. This is

consistent with our result: reaction C occurs with slow pressure equilibration, so that *Mg* can react with $LiBH_4$ according to route (1-11).

Surprisingly, no peaks of $LiBH_4$ appear in the X-ray (a) and (b) patterns of Figure 1-23, although only half lithium borohydride was consumed in reaction A, and the rest of it must be involved in reaction C because of the observed H_2 release with formation of MgB_2 (cf. the (c) pattern). It should be noticed that $LiBH_4$ melts at 280 °C; as PCI experiments were carried out at a higher temperature, re-solidification of unreacted lithium borohydride in nanocrystalline or amorphous form may have occurred. Indeed, results of FTIR measurements show clearly the presence of $LiBH_4$ after the A and B reactions (spectrum (a) in Figure 1-25). The three IR absorption peaks at 2225, 2291 and 2380 cm^{-1} correspond to active *B-H* stretching modes, and the peak at 1125 cm^{-1} indicates a *B-H* bending [83-85]. Our results are consistent with what reported by other authors, who found the X-ray peaks of $LiBH_4$ to be hardly visible after re-solidification from melt [80], and who could detect by FTIR but not by X-ray measurements lithium borohydride formed by hydrogenation of the $2LiH + MgB_2$ assemblage [86].

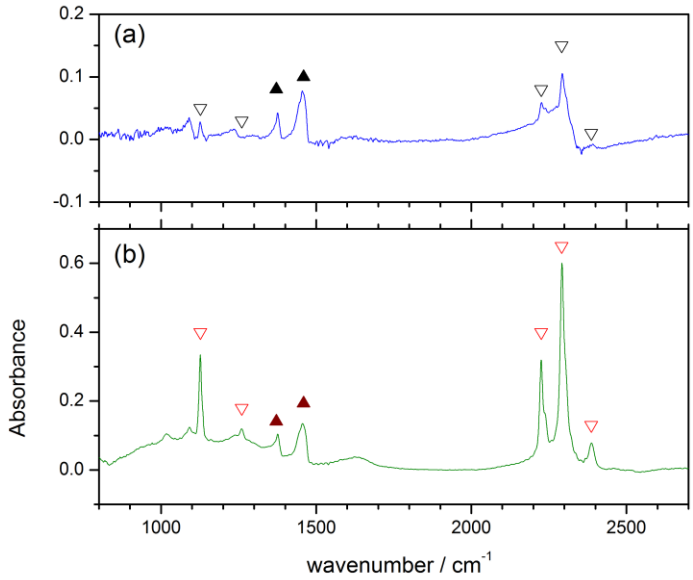

Figure 1-25. FTIR spectra (a) of H_2 desorption products of $2LiBH_4$-Mg_2FeH_6 after reaction B, and (b) of H_2 absorption products after reactions C+B.

In summary, the global desorption reaction can be written as A+4B+C:

$$2Mg_2FeH_6 + 4LiBH_4 \rightarrow 4LiH + 3Mg + 2FeB + MgB_2 + 12H_2 \qquad 1\text{-}12$$

corresponds to a theoretical hydrogen yield of 7.85 wt% H_2. Taking into account that the actual molar ratio of $LiBH_4$ to Mg_2FeH_6 is slightly larger than the nominal value of 2, because of the presence of little residual iron and magnesium in the as-synthesized Mg_2FeH_6 sample, the small excess of $LiBH_4$ is presumed to have reacted with excess *Mg* in reaction C.

In a previous dehydrogenation study of the $5LiBH_4/Mg_2FeH_6$ mixture [87] no clear diffraction peaks could be detected in the X-ray pattern of the decomposed sample, possibly because of the small content of magnesium iron hydride and/or the absorption of the parafilm used as sample holder atmosphere protection. Therefore, the phases obtained could not be identified.

In-situ synchrotron assisted phase identification

The evolution of the synchrotron XRD pattern of $2LiBH_4$-Mg_2FeH_6 during dynamic decomposition in vacuum (heating rate 10°C.min^{-1}) is presented in Figure 1-26.

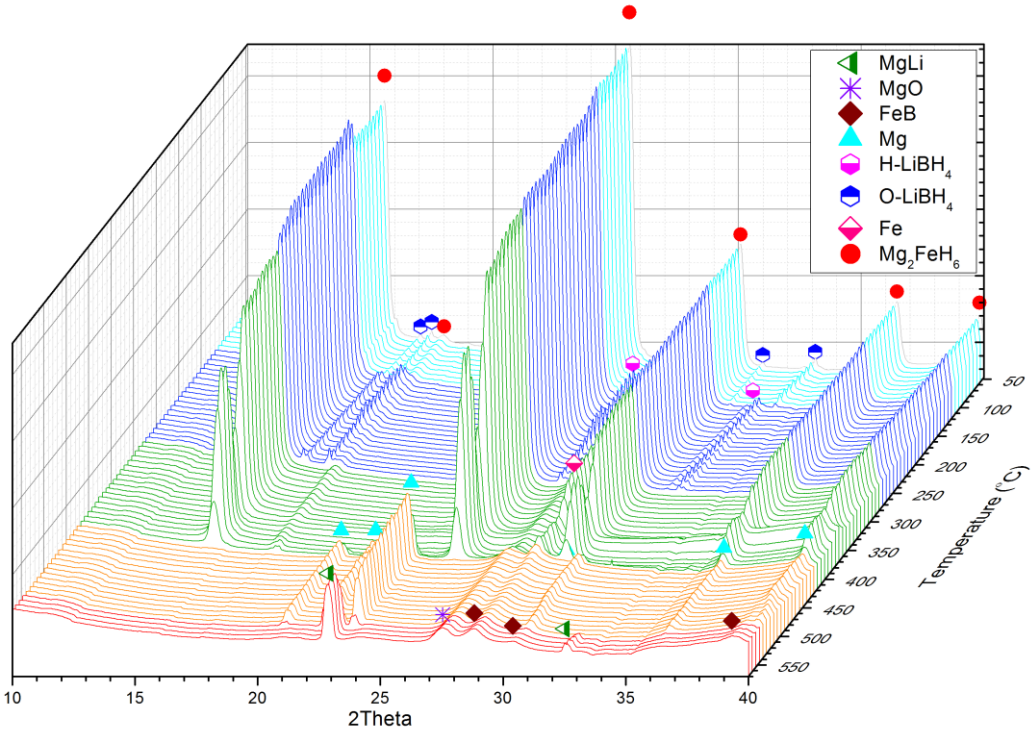

Figure 1-26. In situ synchrotron XRD patterns of $2LiBH_4$-Mg_2FeH_6 during dynamic decomposition in vacuum (10°C.min^{-1} heating rate). Pattern recorded in Lund, Sweden (λ=0.99242Å).

Lithium borohydride transforms from the orthorhombic to hexagonal phase at 110 °C and melts at 285 °C. These values are in agreement with the thermal behavior of pure $LiBH_4$ reported in previous studies [42]. As a result of melting the $LiBH_4$ diffraction peaks disappear in the patterns (Figure 1-27).

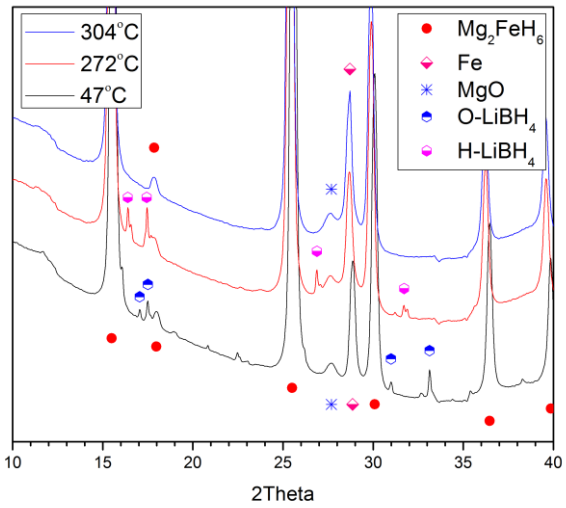

Figure 1-27. Phase change and melting of *$LiBH_4$* (expansion of Figure 1-26).

Before the first decomposition reaction, in the 350 to 400 °C thermal range an unusual behavior of diffraction intensities is observed. Indeed, the background increases sharply and then decreases again; parallel to that, the net Bragg peak intensities drop and rise again. To illustrate the phenomenon, the intensity evolution of two background points (2θ = 10.02 and 35.02°) is plotted vs. temperature in Figure 1-28.

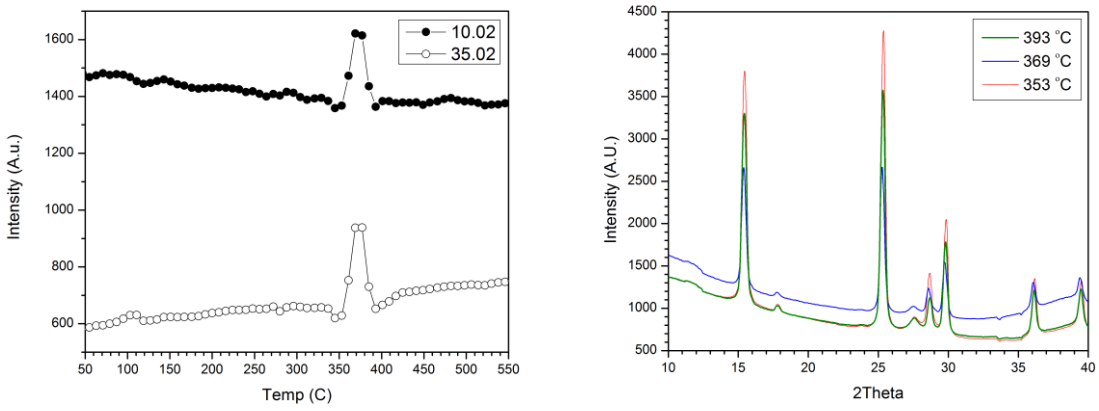

Figure 1-28. Evolution of X-ray diffraction intensity of two background points (2θ=10.02 and 35.02°) vs. temperature (cf. Figure 1-26).

This effect is present also in the dynamic decomposition in hydrogen atmosphere (Figure 1-33), and it can be ascribed to formation of an unknown intermediate amorphous phase which causes a different level of background intensity. Indeed, Orimo et al. have shown a similar phenomenon on decomposition of pure $LiBH_4$ [88]. From Raman results, and comparing with the calculated phonon density of states, they suggested that the intermediate compound should be $Li_2B_{12}H_{12}$, according to the reaction (1-13):

$$12LiBH_4 \rightarrow Li_2B_{12}H_{12} + 10LiH + 13H_2 \qquad 1\text{-}13$$

Unfortunately in our case the LiH product cannot be detected because its diffraction peaks peaks are covered by those of Mg_2FeH_6 and *Fe*. Kang et al. [89] suggested, from DFT calculations, that two other intermediate compounds such as Li_3BH_6 and *LiBH* could be formed, according to reactions (1-14) and (1-15):

$$3LiBH_4 \rightarrow Li_3BH_6 + 2B + 3H_2 \qquad 1\text{-}14$$

$$LiBH_4 \rightarrow LiBH + 3/2H_2 \qquad 1\text{-}15$$

The decomposition of Mg_2FeH_6+$2LiBH_4$ occurs between 420 and 425 °C, producing *Mg* and *FeB*: this means that the process involves the A and B reactions at the same time (Figure 1-29), because of the high heating rate and the strong dehydrogenation driving force of vacuum.

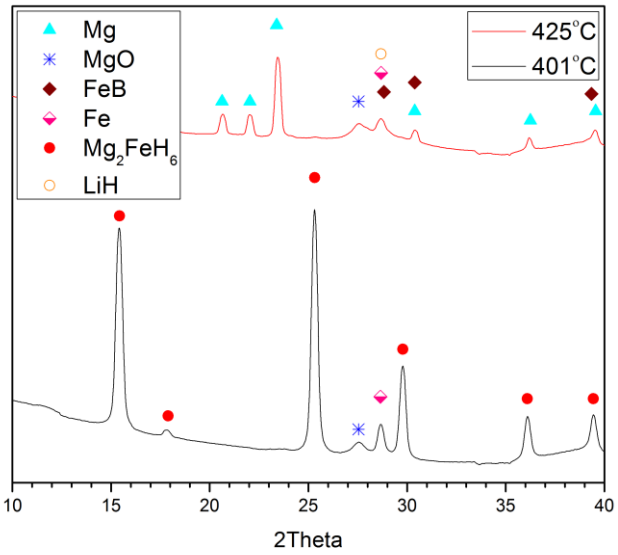

Figure 1-29. Simultaneous A and B reactions ($Mg_2FeH_6 + LiBH_4 \rightarrow FeB + 2Mg + LiH + 9/2H_2$).

Walker et al. reported the results of decomposition of $LiBH_4$ in presence of *Mg* under dynamic vacuum [32]. In agreement with their study, in our case it can be observed that at 440 °C unreacted $LiBH_4$ decomposed to *LiH* and *B* by releasing some hydrogen. Figure 1-30 shows the formation of *LiH* due to the $LiBH_4$ decomposition.

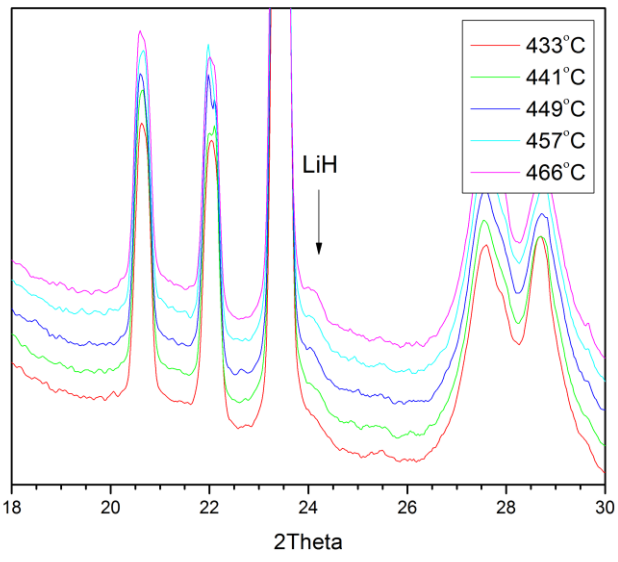

Figure 1-30. *LiH* formation from decomposition of pure $LiBH_4$ at 440°C.

LiH formed on decomposition of $LiBH_4$ reacts with *Mg* at 500 °C producing the $Mg_{0.816}Li_{0.184}$ alloy. Due to *Li* substitution in the magnesium HCP structure two Bragg peaks (2θ = 22.02 and 23.4°) shift to higher 2θ values (Figure 1-31). This alloy formation is in agreement with previous studies on the $2MgH_2$-$LiBH_4$ system [32, 86, 90-92].

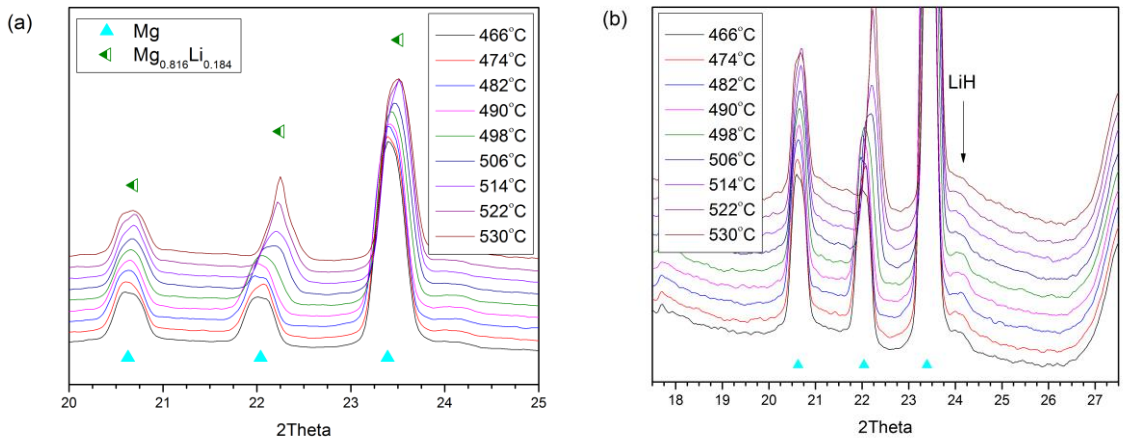

Figure 1-31. Formation of the $Mg_{0.816}Li_{0.184}$ alloy by reaction of *LiH* with *Mg*.

This alloying reaction reduces the *LiH* peak intensity as *Li* diffuses into *Mg* (Figure 1-31-b), and then the higher lithium content alloy $Mg_{0.70}Li_{0.30}$ starts forming with both alloys coexisting in a given thermal range, until only the $Mg_{0.70}Li_{0.30}$ phase is left (Figure 1-32). It should be yet remarked that in the final pattern (at 586 °C) the peak of *LiH* is still present and the alloy peak area has not changed significantly. Therefore, in can be concluded that the overall dynamic decomposition reaction of $2LiBH_4$-Mg_2FeH_6 under vacuum with programmed temperature ramp (10 °C.min^{-1}) is as follows:

$$2\,LiBH_4 + Mg_2FeH_6 \rightarrow FeB + 1.14LiH + 2.86Mg_{0.7}Li_{0.3} + 5.86H_2 \quad \text{1-16}$$

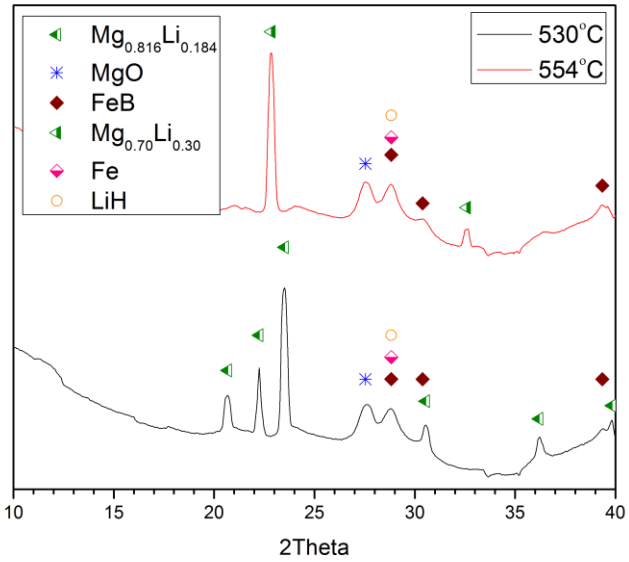

Figure 1-32. Transformation of $Mg_{0.816}Li_{0.184}$ into $Mg_{0.70}Li_{0.30}$.

A different experiment of dynamic decomposition, with in-situ synchrotron XRD monitoring, was carried out in H_2 atmosphere instead of vacuum, and with a lower heating rate (5 °C.min^{-1}). Quite different results were obtained (Figure 1-33), as now all three distinct A, B and C reactions occur at different temperatures and the final decomposition products are *FeB*, MgB_2 and the *Mg* left.

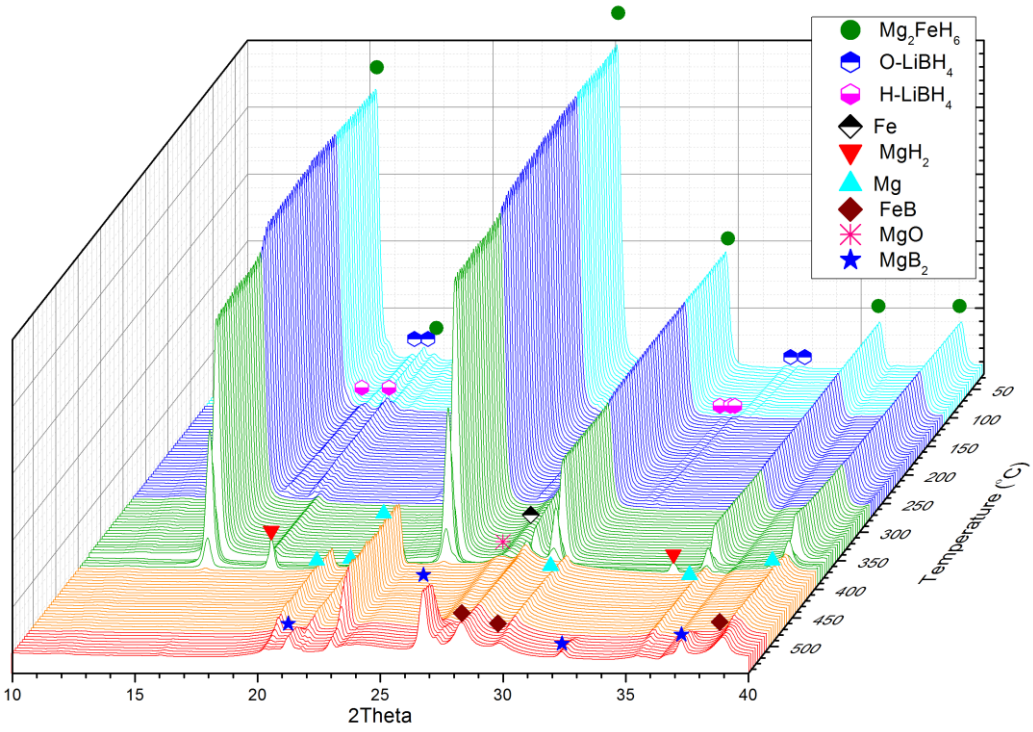

Figure 1-33. In situ synchrotron XRD patterns of $2LiBH_4$-Mg_2FeH_6 dynamic decomposition (heating rate 5 °C.min^{-1}) under 10 bar H_2 atmosphere. Measurement performed in Lund, Sweden (λ=0.99242 Å).

Indeed, the A and B steps are resolved in temperature partially, but not completely. As one can see in the scan recorded at 394 °C (Figure 1-34), the products of the A and B reactions are present together. In comparison with the dehydrogenation in dynamic vacuum, the kinetics of MgH_2 decomposition is slower because of the ambient overpressure instead of under pressure, and also of the lower heating rate.

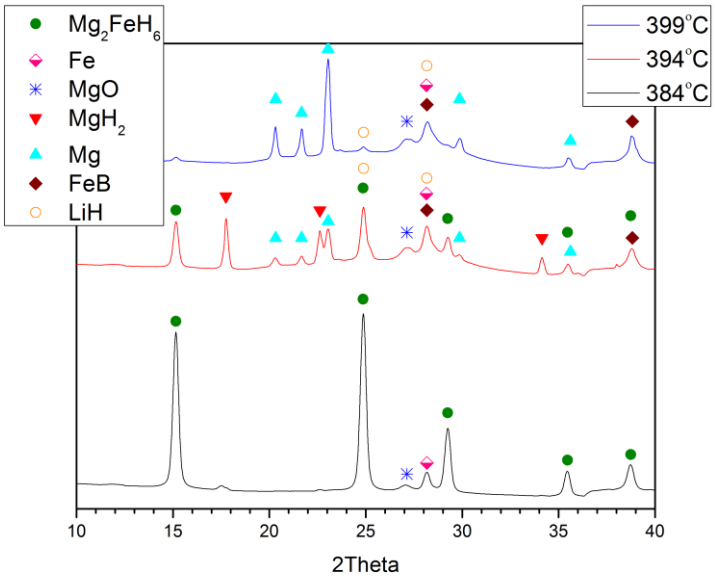

Figure 1-34. A + B reactions at different temperatures.

On increasing temperature, the C reaction takes place at 510 °C. MgB_2 is seen to be formed by reaction of *Mg* with liquid $LiBH_4$. At the end of the process the peaks of some unreacted *Mg* can still be observed (Figure 1-35), in agreement with the proposed reaction based ex-situ XRD measurements.

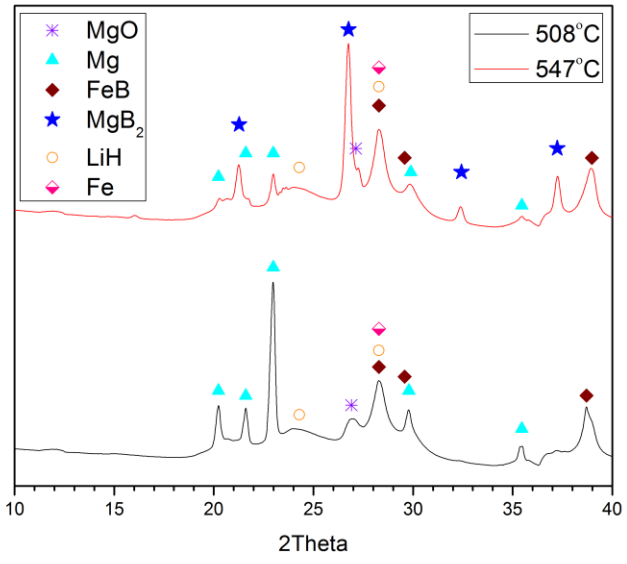

Figure 1-35. Joint decomposition of $LiBH_4$ with *Mg* forming MgB_2 (C reaction).

The last in-situ synchrotron XRD measurement was performed in isothermal mode at 375 °C (Figure 1-36), so as to reproduce the condition of PCI decomposition at the same temperature. The sample kept under H_2 at100 bar, was heated to 375 °C and in three steps the pressure decreased to 35, 10 and 1 bar to observe the A, B and C reactions respectively.

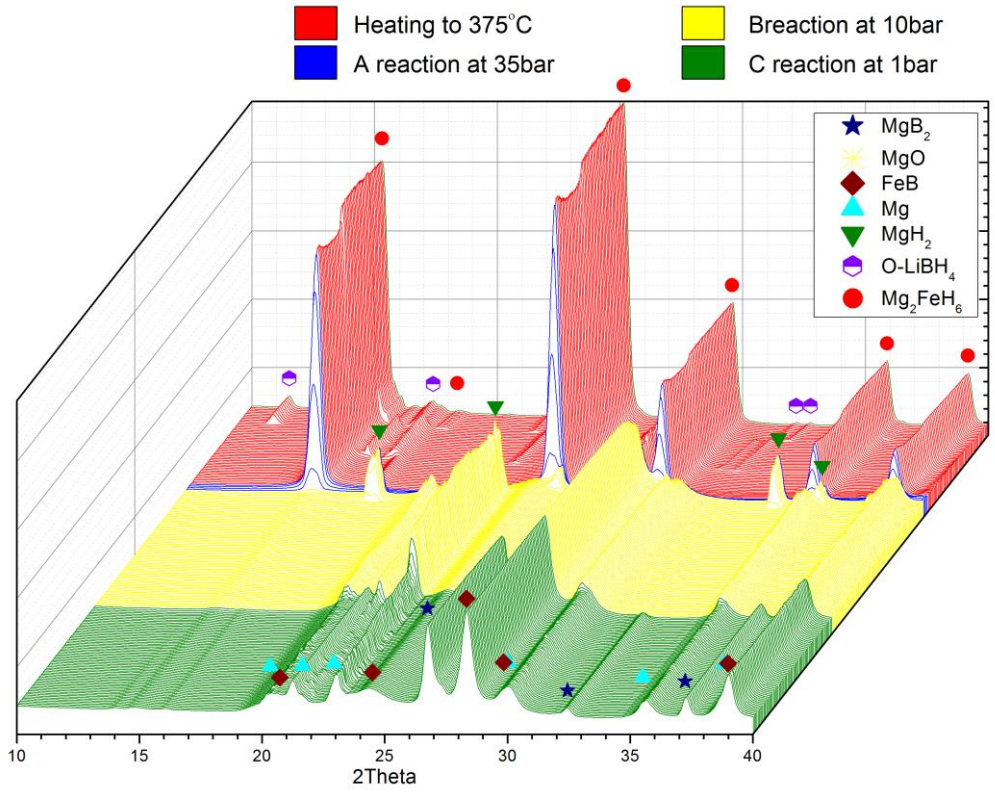

Figure 1-36. In situ synchrotron XRD patterns of $2LiBH_4$-Mg_2FeH_6 isothermal decomposition at 375 °C under various H_2 pressure ranges. Measurement performed in Lund, Sweden (λ=0.99242 Å).

The synchrotron XRD results (Figure 1-36) show that in these conditions all three reactions occurred separately, in complete agreement with the previous ex-situ experiment and conventional XRD study (Figure 1-23). This is confirmed by considering the phase assemblages shown by the separated patterns recorded after each reaction (Figure 1-37).

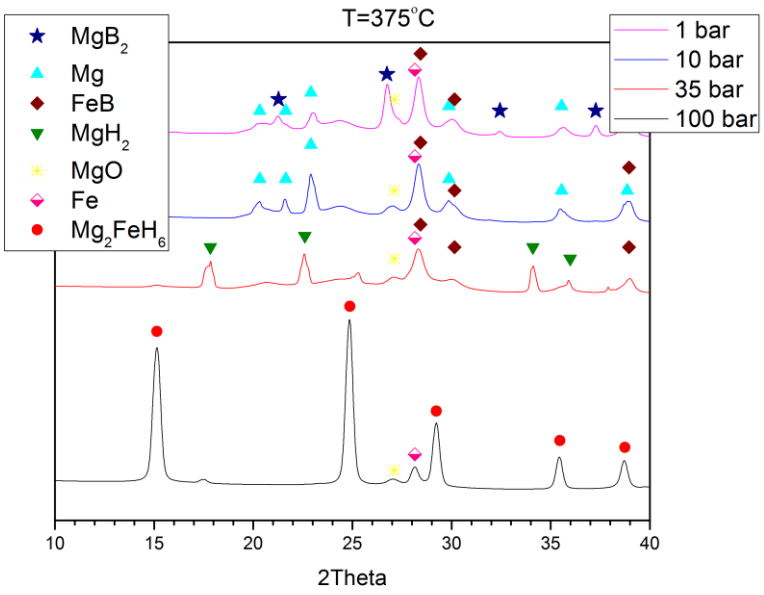

Figure 1-37. In-situ synchrotron XRD patterns recorded after the A, B and C reactions at 375 °C.

1.4.1.3 PCI study of desorption/absorption reactions

The *p(T)* equilibrium relationships were determined for each of the three A, B, and C reactions, by measuring the pressure values at inflexion points of all isothermal plateaus (Figure 1-20). On the basis of van`t Hoff equation:

$$ln(\frac{P}{P_0}) = \frac{\Delta_r S}{R} - (\frac{\Delta_r H}{R})(\frac{1}{T}) \qquad 1\text{-}17$$

The corresponding van't Hoff plots were obtained, and they are shown in Figure 1-38.

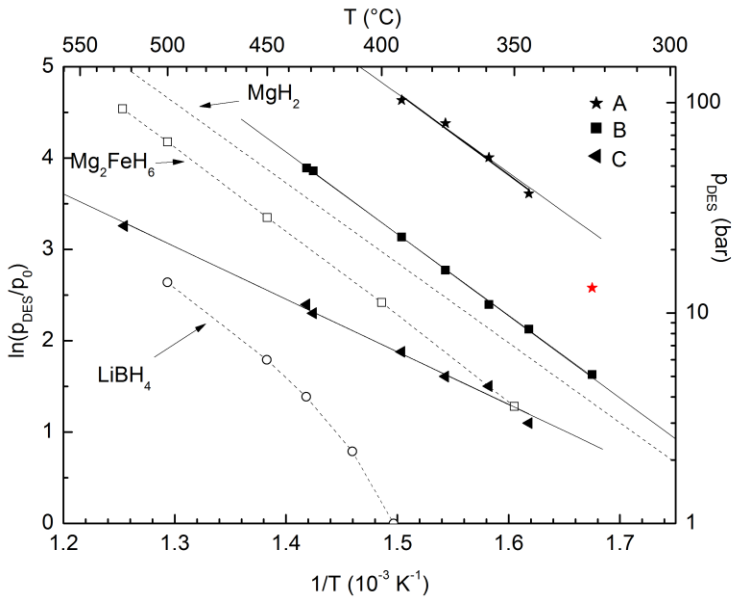

Figure 1-38. Van't Hoff plots of the three dehydrogenation steps A, B, C of the *2LiBH$_4$-Mg$_2$FeH$_6$* composite from PCI desorption results (full symbols including best fit lines). Open symbols denote literature data for the *LiBH$_4$* (circles) [93] and *Mg$_2$FeH$_6$* (squares) [47] decompositions. The dotted line without symbols corresponds to *MgH$_2$* dehydrogenation [24].

The corresponding $\Delta_r H$ and $\Delta_r S$ values, fitted by linear regression and normalized to 1 mole of H_2, are reported in Table 1-5. Also the plots for decomposition of the pure *LiBH$_4$*, *Mg$_2$FeH$_6$* and *MgH$_2$* hydrides from the literature [24, 47, 93] are shown in Figure 1-38 for the sake of comparison; in Table 1-6 the corresponding reaction enthalpies and entropies are given. For *Mg$_2$FeH$_6$*, the entropy for data from Ref. [47] was derived by the van't Hoff fitting of original points; results by other authors [60, 94, 95] are also reported for comparison.

Table 1-5. Thermodynamic parameters (PCI measurements, Figure 1-38) for the *H$_2$* desorption steps of the *2LiBH$_4$-Mg$_2$FeH$_6$* composite, referred to 1 mole of *H$_2$*. The e.s.d.'s are given in parentheses.

	Chemical reaction	$\Delta_r H$ (kJ mol^{-1})	$\Delta_r S$ (J K^{-1}mol^{-1})
A	$2Mg_2FeH_6 + 2LiBH_4 \rightarrow 2LiH + 4MgH_2 + 2FeB + 5H_2$	72(4)	147(7)
B	$MgH_2 \rightarrow Mg + H_2$	74.6(7)	138.0(8)
C	$2LiBH_4 + Mg \rightarrow 2LiH + MgB_2 + 3H_2$	48(2)	87(2)

By inspection of Figure 1-38, the van't Hoff plot of process A lies well above the decomposition lines of Mg_2FeH_6 and $LiBH_4$ (and also of MgH_2). This proves definitely that both components of the composite are strongly destabilized thermodynamically by reacting together with formation of iron boride *FeB*, according to reaction (1-9). For the sake of comparison it can be useful to extrapolate the ideal dehydrogenation temperature at standard pressure by the Δ_rH/Δ_rS approximation, on neglecting the thermal dependence of enthalpy and entropy. We get 217 °C, to be compared with 302-319 °C for Mg_2FeH_6 and 370 °C for $LiBH_4$, on the basis of data in Table 1-6. Thus, the first H_2 desorption step of the $2LiBH_4$-Mg_2FeH_6 composite is confirmed to be thermally more favorable than dehydrogenation of either pure hydride component. Interestingly, this result is due not to the reaction enthalpy, which is comparable for the three reactions (cf. Table 1-5 and Table 1-6, and the slopes of van't Hoff plots in Figure 1-38), but to the entropy, which is substantially larger for reaction (1-9) than for decomposition of either simple hydride. Therefore in this case the thermodynamic destabilization (i.e., the decrease of $\Delta_rG = \Delta_rH - T\Delta_rS$) is due to the entropic rather than to the enthalpic effect.

Table 1-6. Literature thermodynamic parameters for the dehydrogenation reactions of Mg_2FeH_6, MgH_2 and $LiBH_4$, referred to 1 mole of H_2.

Chemical reaction	Δ_rH (kJ mol^{-1})	Δ_rS (J K^{-1}mol^{-1})	Ref.
$Mg_2FeH_6 \rightarrow 2Mg + Fe + 3H_2$	77	134	[47]
	87(3)	147(15)	[95]
	80(7)	137(13)	[94]
	79	135	[60]
$MgH_2 \rightarrow Mg + H_2$	74.5	135	[24]
$2LiBH_4 \rightarrow 2LiH + 2B + 3H_2$	48(2)	87(2)	[93]

According to plots of Figure 1-38, reaction B is clearly confirmed to be the dehydrogenation of magnesium hydride; the numerical values of van't Hoff parameters in Table 1-5 match well with literature data (Table 1-6). Reaction C shows a remarkably smaller enthalpy than all other processes (including those of Table 1-6). This enthalpy is

comparable to that given in the literature for decomposition of the $LiBH_4+MgH_2$ assemblage in a single step [34]; we are not aware of previous results for the individual second step C. Indeed, it is interesting to notice how the plots of reactions B and C are well separated in Figure 1-38, fully consistent with the two-step model proposed for the $LiBH_4+MgH_2$ decomposition [81]. Thus, $LiBH_4$ is destabilized by reaction (1-9) because of its smaller enthalpy, which over compensates the slight increase of entropy, with respect to dehydrogenation of pure $LiBH_4$ (cf. also Figure 1-38).

The scheme of dehydrogenation reactions should be discussed also in connection with the amount of hydrogen released in the three different identified steps. In Table 1-7, the average values of desorbed H_2 wt% (PCI and TPD results) are given for the A, B, C processes and for the overall decomposition reaction. Significant deviations from the PCI averages can be observed for individual isotherms (cf. also Figure 1-20). For comparison, the theoretical ideal wt% values are reported, too; these quantities are always referred to the initial weight of the $2LiBH_4$-Mg_2FeH_6 composite. As a small fraction of unreacted *Fe* and *Mg* is present in the sample, as discussed in the previous section, the ideal overall H_2 wt% should be corrected accordingly. On using the Fe/Mg_2FeH_6 weight ratio obtained by Rietveld refinement of the X-ray pattern, an expected overall wt% hydrogen yield of 7.45% is obtained for the system (cf. the ideal value of 7.85%).The other corrected values for individual reaction steps are also reported in the last column of Table 1-7. Average PCI and TPD results are slightly lower than expected for the B and C reactions; the deficit is somehow larger for the A step (from PCI rather than TPD data). On the whole, therefore, the observed relative amounts of desorbed hydrogen are consistent with the interpretation of reactions A, B and C according to (1-9), (1-10) and (1-11).

Table 1-7. Average hydrogen yields of the decomposition steps of the $2LiBH_4$- Mg_2FeH_6 composite from isothermal (PCI) and dynamic (TPD) measurements, compared with ideal and corrected values (cf. the text).

	PCI H wt%	TPD H wt%	Ideal H wt%	Corrected H wt%
A	1.9	2.6	3.27	2.93
B	2.2	2.0	2.62	2.34
C	2.0	1.9	1.96	2.18
Total	6.1	6.5	7.85	7.45

The final samples obtained after full decomposition (1-12) could always be rehydrogenated successfully in the Sievert apparatus. However, only the equivalent of the H_2 amount released in the C and B steps was reabsorbed, whereas the A reaction could not be reversed (Figure 1-39). The two distinct C and B plateaus can be observed clearly at 359 °C (a), whereas at 375 °C the B and C processes merge into a single plateau (b). At 460 °C only the C plateau (reverse of reaction1-11) can be observed, as the MgH_2 formation from $Mg + H_2$ (B process) would need 80 bar hydrogen pressure at this temperature (c).

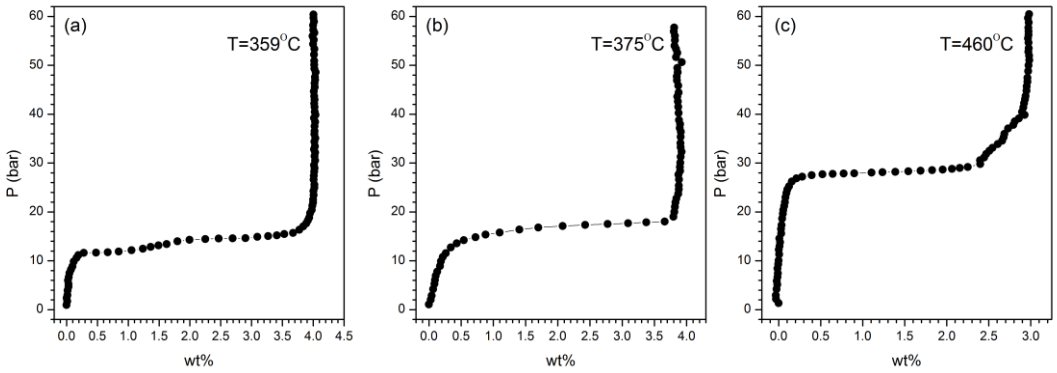

Figure 1-39. PCI hydrogenation of a fully decomposed sample of $2LiBH_4$- Mg_2FeH_6 at three different temperatures.

Comparable amounts of exchanged H_2 are observed in absorption and desorption modes for both the B and C steps. Re-desorption experiments were also performed after absorption, showing a very good reproduction of the B and C dehydrogenation steps as in the first desorption cycle.

The complete C+B rehydrogenation process can be written as:

$$2LiH + MgB_2 + 4H_2 \rightarrow 2LiBH_4 + MgH_2 \qquad 1\text{-}18$$

The fingerprints of *$LiBH_4$* formed on rehydrogenation appear with great evidence (in the IR spectrum (b) in Figure 1-25), whereas the corresponding X-ray pattern (Figure 1-40) shows only the peaks of *MgH_2* and *FeB*.

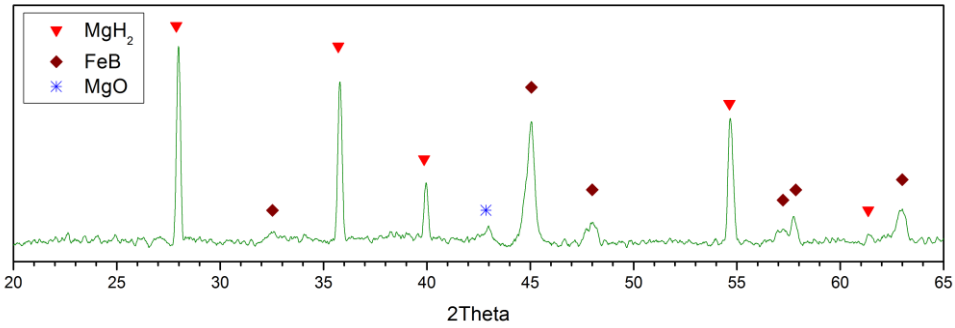

Figure 1-40. X-ray diffraction patterns (CuKα radiation) of the products of rehydrogenation the products of complete dehydrogenation of *$2LiBH_4$-Mg_2FeH_6* mixture composite.

Van't Hoff plots for C and B hydrogenation reactions are shown in Figure 1-41 as dashed lines.

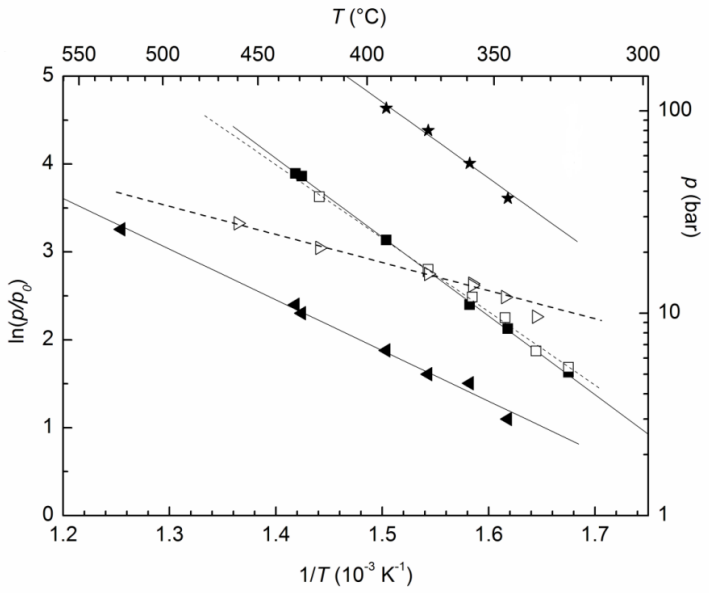

Figure 1-41. Van't Hoff plots of the A (stars), B (squares), and C (triangles) dehydrogenation reactions and of the B (open squares) and C (open triangles) hydrogenation processes.

The B line is nearly coincident with the corresponding one for dehydrogenation, confirming the well-known good reversibility of B reaction. On the other hand, a strong hysteresis increasing with decreasing temperature is observed in the C case. Further, a peculiar feature appears immediately: the C hydrogenation line crosses the B one at about 370 °C, so that above that temperature the reaction occurs as:

$$2LiH + MgB_2 + 3H_2 \rightarrow 2LiBH_4 + Mg \qquad 1\text{-}19$$

On the other hand, below 370 °C the slightly different path is observed:

$$2LiH + MgB_2 + 4H_2 \rightarrow 2LiBH_4 + MgH_2 \qquad 1\text{-}20$$

Here the B process $Mg + H_2 \rightarrow MgH_2$ occurring at lower pressure consumes the excess Mg coming from Mg_2FeH_6 decomposition. The two variants of C hydrogenation reaction share approximately the same van't Hoff plot with $\Delta_r H$= -27(2) kJ.mol $(H_2)^{-1}$ and $\Delta_r S$= -64(2) J.K^{-1}mol $(H_2)^{-1}$; cf. the values for C dehydrogenation (Table 1-5) $\Delta_r H$= 48(2) kJ.mol $(H_2)^{-1}$ and $\Delta_r S$= 87(2) J.K^{-1}mol $(H_2)^{-1}$. The much smaller slope of the hydrogenation line makes the hysteresis gap to widen significantly at lower temperatures, consistently with what expected as reversibility is favored by higher *T* values.

C reaction in the low temperature range

The $2LiBH_4$-Mg_2FeH_6 decomposition reaction pathway is altered for T<340 °C. The A and B processes are still the same, but the C reaction changes. Figure 1-42 illustrates the behavior of the C plateaus from PCI measurements in the low temperature range; those below 340 °C appear clearly to be different from that at 344 °C. The pressure values derived from the van't Hoff line of the C reaction at 315, 324 and 335 °C should lie between 2.1 to 2.7 bar, whereas the observed plateaus are at about 0.5 bar.

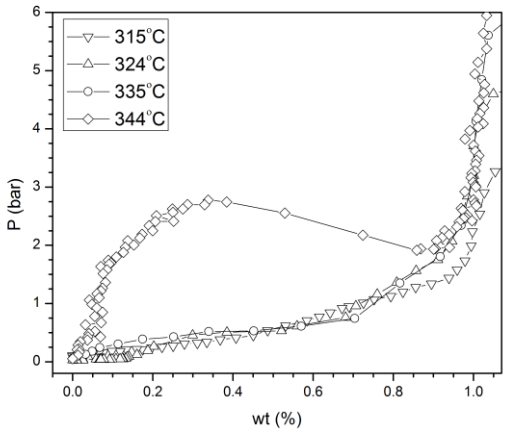

Figure 1-42. C dehydrogenation step from PCI measurements at low temperatures.

A PCI rehydrogenation experiment was also done on the sample decomposed at 324 °C (Figure 1-43). In this case the absorbed hydrogen amount is about half of that found on high temperature rehydrogenation. On the basis of the plateau pressure, the process can be considered to be a pure magnesium hydrogenation (B reaction). It can be concluded that, on dehydrogenation at 324 °C, in the plateau at low pressure (C`) no MgB_2 had formed, so that the process could only correspond to plain $LiBH_4$ decomposition giving $LiH + B + 3/2H_2$.

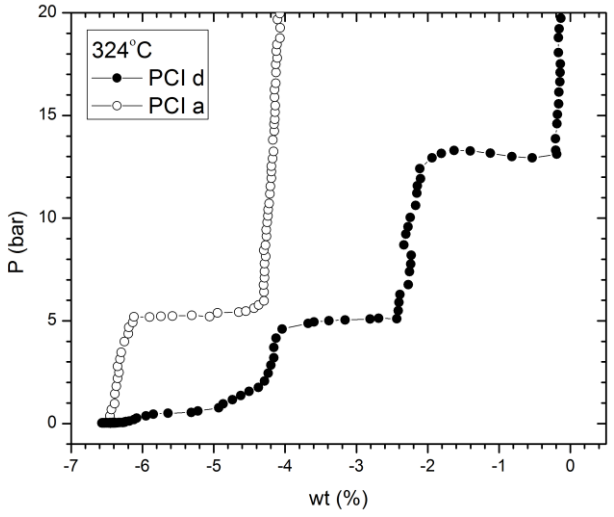

Figure 1-43. PCI dehydrogenation/rehydrogenation cycle at 324°C.

1.4.1.4 Kinetic study of desorption/absorption reactions

Isothermal kinetic curves

Kinetic measurements in isothermal-isobaric mode were performed on the A and C dehydrogenation reactions at several *T* and *p* values, which were selected taking into account the corresponding thermodynamic van't Hoff plots. Some preliminary results were obtained also for C hydrogenation. For a given reaction, the equilibrium H_2 pressure $p_e(T)$ is calculated on the basis of the reaction enthalpies and entropies reported in Table 1-5 (and given above in the C hydrogenation case). For each temperature, measurements were repeated at different values of overpressure $\Delta p/p = (p - p_e)/p_e$. Although this is usually negative for dehydrogenation and positive for hydrogenation, non-zero reaction rates were observed also for small $\Delta p/p$ values with the 'wrong' sign, as will be discussed below. Results of kinetic measurements are reported as curves of the normalized degree of reaction advancement ξ (vs. a total of 3 and 2 wt% H_2 for the A and C cases, respectively) against time *t*. As examples, the curves obtained for dehydrogenation A at 358 °C and $\Delta p/p$ = -0.233, -0.067, 0.088 are shown in Figure 1-44, and those for C at 375 °C and $\Delta p/p$ = -0.255, -0.149, -0.021, 0.064 are shown in Figure 1-45.

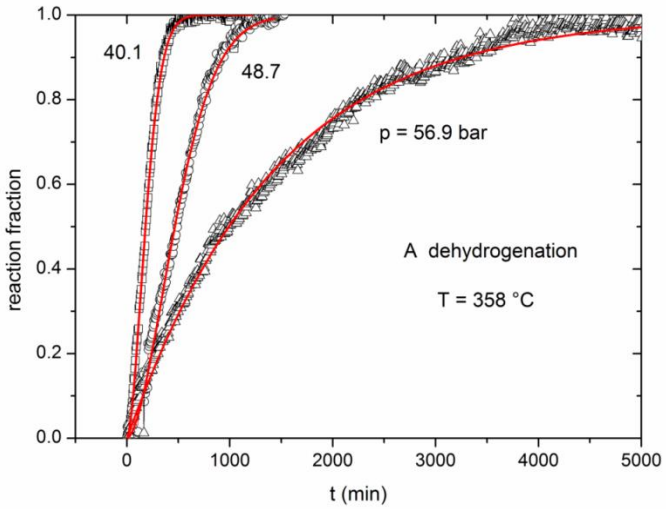

Figure 1-44. Isothermal kinetic plots for the A reaction
($2Mg_2FeH_6 + 2LiBH_4 \rightarrow 2LiH + 4MgH_2 + 2FeB + 5H_2$)
at three different hydrogen pressures. Avrami-like fitting curves are shown.

All kinetic curves for the C reaction have a clear sigmoidal shape, so as to immediately suggest use of the Avrami (or Johnson-Mehl-Avrami-Kolmogorov (JMAK)) equation [96-99] $\xi(t) = 1 - exp[-(kt)^n]$ for fitting data and derive the rate constant *k*. In the A case, where the reaction kinetics is clearly much slower (compare Figure 1-44, Figure 1-45 and Figure 1-45), the shape of curves rather resembles that of first-order kinetics.

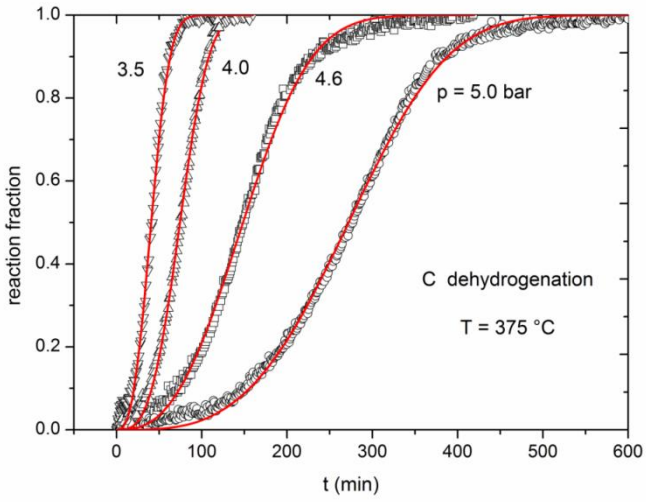

Figure 1-45. Isothermal kinetic plots for the C dehydrogenation
($2LiBH_4 + Mg \rightarrow 2LiH + MgB_2 + 3H_2$)
at four different hydrogen pressures. Avrami-like fitting curves are shown.

However, the JMAK formula is able to include also that as a particular case, so that the fitting was performed by the same equation for all A and C data. In each case the calculation was carried out both on relaxing the *n* exponent, and on fixing it at the closest integer value. The fitted rate constant *k* did not change significantly, proving to be rather independent of minor exponent variations. For the A reaction, the relaxed *n* exponent ranged between 1 and 2, whereas in the C case values between 2.5 and 3.5 were obtained. The quality of the fitting was always very good, with an average R^2 index value of 99.5% (cf. Figure 1-44, Figure 1-45 and Figure 1-45). However, we also tried different kinetic models, like the 'contracting volume' or 'moving boundary'

equation [99], $\xi(t) = 1 - (1 - kt)^3$, and the diffusion-controlled one [99], $\xi(t) = 1 - [1 - (kt)^{1/2}]^3$. In all cases the fit was definitely much worse than with the JMAK formula. Taking into account the physical basis underlying the Avrami model, and the fitted *n* exponent values, we can conclude that the C reaction kinetics is controlled by the slow step of growth of nuclei with *n* dimensions in cases with the lower *n* exponents, with a contribution of the nucleation step when *n*> 3. For the slower A reaction, a pure growth mechanism with low grain dimensionality seems to be appropriate.

A preliminary kinetic study was also carried out on the C hydrogenation reaction, by performing a limited number of measurements. In Figure 1-46 examples of isotherms for a single temperature and different overpressure values (0.105, 0.133 and 0.319) are shown. Such curves resemble more those of dehydrogenation A than C, as they lack the sigmoidal shape of the latter. The Avrami equation proved yet to be quite adequate to fit data, with an *n* exponent slightly smaller than 1.

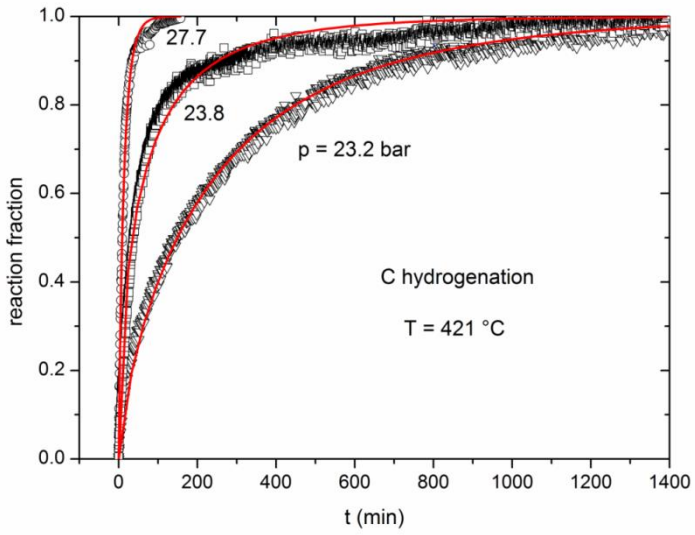

Figure 1-46. Isothermal kinetic plots for the C hydrogenation
($2LiH + MgB_2 + 3H2 \rightarrow 2LiBH_4 + Mg$)
at three different hydrogen pressures. Avrami-like fitting curves are shown.

Rate constant dependence on temperature and overpressure

By the JMAK fitting of kinetic curves, a set of rate constants k associated to different temperatures and overpressures was derived for each of the A and C dehydrogenation reactions, obtaining corresponding numerical tables of $k(T, \Delta p/p)$ data. We assume that this functional dependence can be factorized into the product

$$k = k_0(T) k_1(^{\Delta p}/_{p}) \qquad 1\text{-}21$$

Where k_0 is defined as the rate constant at vanishing overpressure (i.e. for $p = p_e$), so that the condition $k_1(\Delta p/p = 0) = 1$ must be fulfilled. More generally, the second factor k_1 should be written as $k_1(T, \Delta p/p)$, in order to include a possible coupling of its thermal and pressure dependences.

At constant T, we tried to fit the $k(\Delta p/p)$ empirical function at first by the power law $lnk = a \times ln(\Delta p/p + 1) + b$, obtaining satisfactory results but with quite large values of the -a exponent (between 5 and 6). This would indicate a stronger kinetic effect of overpressure than in the study of sodium alanate [100, 101], where a linear or parabolic dependence of the rate constant on overpressure was observed. Then an exponential law was tested, according to

$$\mathrm{lnk} = \mathrm{a}(^{\Delta \mathrm{p}}/_{\mathrm{p}}) + \mathrm{b} \qquad 1\text{-}22$$

This linear relationship between lnk and overpressure proved to be always well obeyed, and thus the exponential empirical law was adopted for treatment of all data. Indeed this formula is easily integrated into a kinetic theoretical frame, as will be discussed below, at variance with the power law with large variable exponent. An example of two experimental straight lines of lnk vs. $\Delta p/p$ for the C dehydrogenation is shown in Figure 1-47.

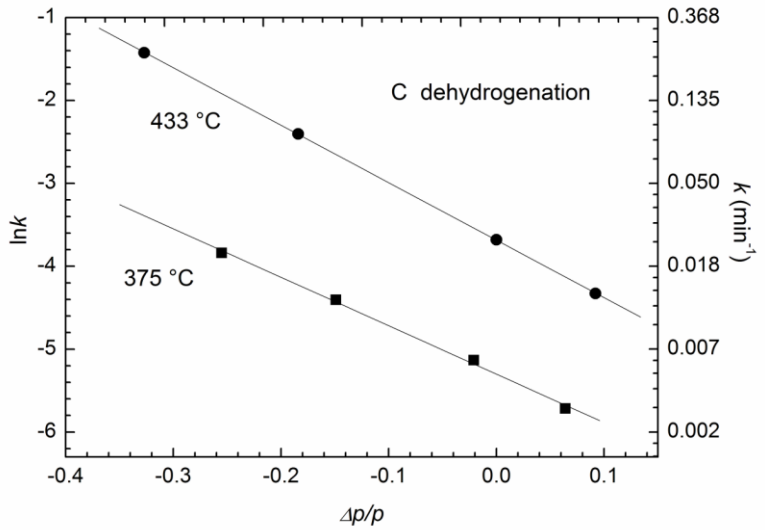

Figure 1-47. Logarithm of the rate constant k (min^{-1}) for the C dehydrogenation plotted against overpressure $\Delta p/_p = (p - pe)/_{p_e}$ at two different temperatures.

The fitted *a* and *b* linear coefficients for all measured data of the A and C reactions are reported in Table 1-8.

Table 1-8. Coefficients of the $lnk = a(\Delta p/_p) + b$ empirical relation between reaction rate constant k (min^{-1}) and overpressure $\Delta p/_p$, fitted to isothermal kinetic measurement data.

T (°C)	a	b
A dehydrogenation		
324	-3.3	-7.78
343	-4.2	-6.92
358	-5.8	-6.75
363	-5.3	-6.25
376	-5.4	-5.8
C dehydrogenation		
345	-3.9	-6.63
358	-4.6	-6.09
375	-5.8	-5.3
392	-4.2	-4.82
433	-6.9	-3.69
460	-9.5	-3.3

C hydrogenation		
421	11	-6.3
460	15	-6

The zero-order coefficient in (1-22) can be written as $b = lnk_0$, according to Eqn. 1-21 and the definition of k_0. Eqn. 1-22 can then be restated as:

$$k = k_0(T)exp[a(^{\Delta p}/_{p})] \qquad 1\text{-}23$$

So that $k_1 = exp[a(^{\Delta p}/_{p})]$ is obtained with the a coefficient including a possible thermal dependence. The Arrhenius-like dependence on temperature can be reasonably assumed for $k_0(T)$:

$$k_0 = f\exp\left(-\frac{\Delta G_a^0}{RT}\right) = f\exp\left(\frac{\Delta S_a^0}{R}\right) \times \exp\left(-\frac{E_a^0}{Rt}\right) = A_0\exp\left(-\frac{E_a^0}{RT}\right) \qquad 1\text{-}24$$

Where f is an effective vibrational frequency (or a dimensional coefficient time^{-1}), ΔG_a^0 and ΔS_a^0 are the activation Gibbs free energy and entropy, respectively, at vanishing overpressure, and E_a^0 is the corresponding activation energy (approximately equal to the activation enthalpy ΔH_a^0 at the pressures of interest). On looking at values in Table 1-8, a decreasing trend of a with increasing temperature appears clearly for both reactions; this can be simply modeled according to $a = a_0 + a_1/T$, with $a_0 < 0$ and $a_1 > 0$. This means that the higher the temperature, the more effective is overpressure to increase the reaction rate. On substitution into the k expression, one obtains:

$$k = k_0 \exp\left[\left(a_0 + \frac{a_1}{T}\right)\left(\Delta p/p\right)\right]$$

$$= f\exp[\frac{\Delta S_a^0}{R} + a_0(\Delta p/p)] \times \exp[-\frac{E_a^0 - Ra_1\left(\Delta p/p\right)}{RT} \qquad 1\text{-}25$$

$$= Aexp(-\frac{E_a}{RT})$$

Eqn.1-25 can be interpreted by stating that (negative) overpressure has a twofold effect: it increases both the activation entropy and the activation energy. The second effect is due to the thermal dependence of the *a* coefficient with positive a_1 parameter, and it reduces the increase of reaction rate *k* due to the first one:

$$\Delta S_a = \Delta S_a^0 + Ra_0\left(\Delta p/p\right) \qquad 1\text{-}26$$

$$E_a = E_a^0 - Ra_1\left(\Delta p/p\right) \qquad 1\text{-}27$$

$$A = f\exp\left(\Delta S_a/R\right) \qquad 1\text{-}28$$

The thermal dependence of the rate constant was analyzed by plotting $b = lnk_0$ against 1/*T* from data of Table 1-8 for each of the A and C dehydrogenation reactions. According to the Arrhenius relation (1-24): $lnk_0 = -E_a/RT + lnA_0$, so that by a linear fit of lnk_0 vs. 1/*T* the activation energy and the pre-exponential factor A_0 at $\Delta p/p$=0 can be obtained. The procedure was then repeated for non-vanishing overpressure values, by plottinglnk calculated by eqn. 1-22, instead of lnk_0, vs. 1/*T*. In this way the Arrhenius parameters were obtained as functions of $\Delta p/p$, according to the dependence appearing in eqn. 1-25. The results are reported in Table 1-9 for each reaction and for different overpressure values.

Table 1-9. Arrhenius parameters (activation energy and logarithm of the pre-exponential factor) from kinetic measurements on dehydrogenation reactions A and C at different overpressures *Δp/p*. The e.s.d.'s are given in parentheses.

Δp/p	Ea (kJ mol-1)	ln(A/min-1)
A dehydrogenation		
0	118(13)	16(2)
-0.1	132(10)	19(2)
-0.2	148(7)	23(1)
-0.3	163(6)	26(1)
C dehydrogenation		
0	110(7)	15(1)
-0.1	130(10)	19(2)
-0.2	139(13)	22(2)
-0.3	149(17)	24(3)

In Figure 1-48 and Figure 1-49 the Arrhenius plots are shown in the A and C cases, respectively, for *Δp/p*= 0 and -0.30. The corresponding linear relationships (1-26) are as follows:

$$E_a = -151\left(^{\Delta p}/_{p}\right) + 118\, kJ.mol^{-1}, ln(A/min^{-1}) = -34(^{\Delta p}/_{p}) + 16,$$

For reaction A and;

$$E_a = -160(^{\Delta p}/_{p}) + 110\, kJ.mol^{-1}, ln(A/min^{-1}) = -34(^{\Delta p}/_{p}) + 15,$$

for reaction C.

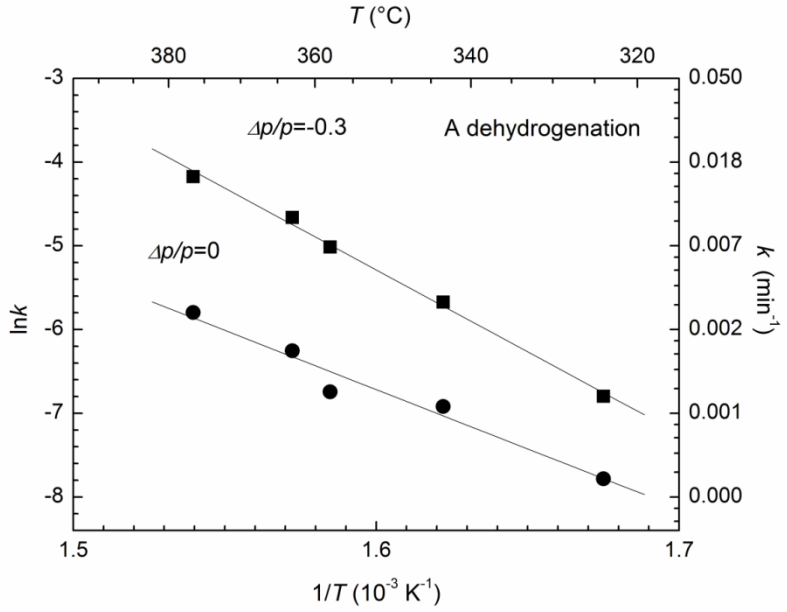

Figure 1-48. Arrhenius plots for the A dehydrogenation reaction at two different values of the overpressure *Δp/p*.

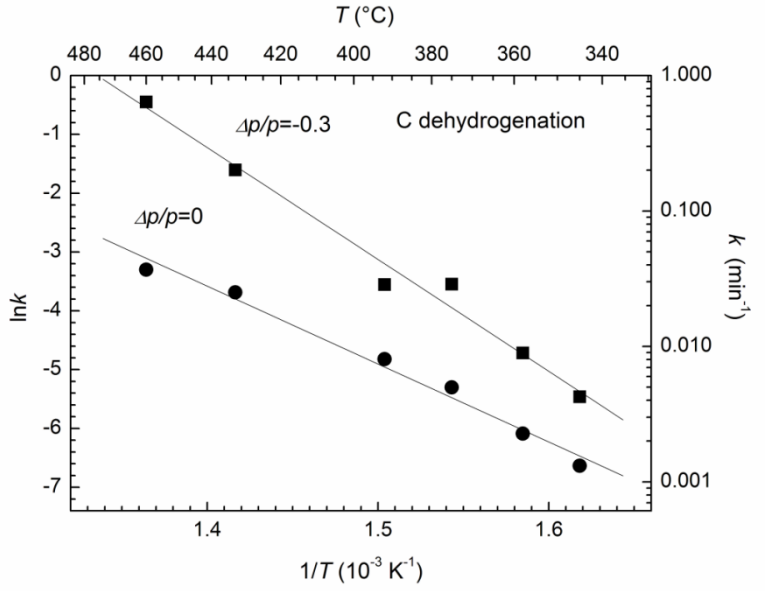

Figure 1-49. Arrhenius plots for the C dehydrogenation reaction at two different values of the overpressure *Δp/p*.

The coefficients of the $a = a_0 + a_1/T$ expression turn out to be for A: a_0 = -34, $a_1 = 18 \times 10^3\ K$; for C: a_0 = -34, $a_1 = 19 \times 10^3\ K$. Such coefficients could have been obtained also by direct fitting of the *a* values *reported in* Table 1-8 against 1/*T*,

where the scatter of data shows that they are affected by a significant uncertainty. However, the overall trend is well defined, with not only the activation energies and entropies at $\Delta p/p$=0, but also their overpressure coefficients very similar for both dehydrogenation reactions. This suggests that the temperature/overpressure effects on the rate constant are controlled by physical features of the solid phases present (surface state and extension, defect distribution, interface energy, etc.), which are similar in the A and C cases, rather than by their chemical specificities.

For results of C hydrogenation, the rate constant k vs. $\Delta p/p$ was again fitted by eqn. (1-22). The a and b coefficients obtained are reported in Table 1-8 for only two T values, so that the Arrhenius-like analysis of results could not be done because of insufficient data. However, one can notice that the $|a|$ values are over 50% bigger than the corresponding ones for dehydrogenation, indicating a significantly larger effect of overpressure in accelerating hydrogenation ($\Delta p/p > 0$) with respect to dehydrogenation ($\Delta p/p < 0$) for the C reaction. Of course, the sign of a changes with reversion of the reaction direction.

Thermodynamic driving force and irreversibility

More insight into the fundamental kinetic meaning of the previous analysis can be obtained by relating overpressure $\Delta p/p$ to the thermodynamic driving force ΔG. According to basic thermodynamics, $\Delta G = \pm RT ln(\Delta p/p + 1)$, with positive and negative signs for dehydrogenation and hydrogenation directions, respectively; for $|\Delta p/p|$ smaller enough than 1, $\Delta G \approx \pm RT(\Delta p/p)$, so that by substitution of $\Delta p/p$ in eqns. (1-23) and (1-24) we obtain:

$$k = k_0 \exp(\pm a\Delta G/RT) = f\exp[-(\Delta G_a^0 \pm a\Delta G)/RT \qquad 1\text{-}29$$

This relationship connects the action of the thermodynamic driving force to the Arrhenius formalism, based on the activated state concept. It resembles somehow the **Tafel** equation of electrochemical kinetics [102], where the driving force ΔG is proportional to overvoltage rather than to overpressure. However, there is a fundamental

difference, because in Tafel equation *a* is replaced by the transfer coefficient $1 \geq \alpha \geq 0$; here, on the other hand, *a* is an empirical parameter with absolute value larger than 1. This means that, in the present instance, the overpressure driving force has a stronger action in increasing the rate constant: in addition to the maximum 'transfer' effect (α = 1), there is a further direct reduction of the activation barrier ΔG_a^0 by a $(|a| - 1)|\Delta G|$ amount.

In cases where the dehydrogenation reaction is irreversible (A), or where it is reversible but with a large hysteresis (C), the Tafel (or Butler-Volmer) approach [102] of electrochemical kinetics should be modified. In fact, it is not possible any more to use the same kinetic diagram of *G* free energy along the reaction coordinate in both directions of the transformation. One is forced either to consider only one of the two directions (A dehydrogenation), or to consider two different *G* diagrams specific for each direction (C dehydrogenation and hydrogenation). In particular, in the latter case two 'equilibrium' pressures are defined at each temperature: $p_{e1}(T)$ for dehydrogenation and $p_{e2}(T)$ for hydrogenation, with $p_{e1}(T) < p_{e2}(T)$: see the two experimental van't Hoff lines in Figure 1-41. In this instance 'equilibrium' means simply that both phase assemblages (cf. $2LiH + MgB_2 + 3H_2$ and $2LiBH_4 + Mg$) may coexist together at either $p_{e1}(T)$ or $p_{e2}(T)$, but the direction of transformation is unique and different in each case. Therefore, using p_{e1} and p_{e2} as reference pressures for defining overpressures (as we did to analyses kinetic data in Table 1-8) may not be the only possible choice, particularly in the region $p_{e1}(T) < p < p_{e2}(T)$, where overpressure ranges with 'wrong' signs (positive for dehydrogenation, negative for hydrogenation) are observed. An empirical alternative to remove this feature could be to use the average $(p_{e1} + p_{e2})/2$ as single reference pressure for both reactions.

1.4.1.5 The effect of FeB on the $LiBH_4$-MgH_2 system

To investigate the effect of *FeB* on the $LiBH_4$-MgH_2 dehydrogenation, such a composite was prepared by mixing 1:1 commercial MgH_2 and $LiBH_4$. Decomposition experiments in PCI mode were done at T= 340 and 345 °C. After the $MgH_2 \rightarrow Mg + H_2$ process (equivalent to B) has occurred, on decreasing pressure dehydrogenation of

the *LiBH₄+Mg* system takes place. The results are shown and compared to the corresponding previous ones for C reaction (where the *LiBH₄+Mg* assemblage decomposes in presence of *FeB* produced by the previous A process) Figure 1-50 .

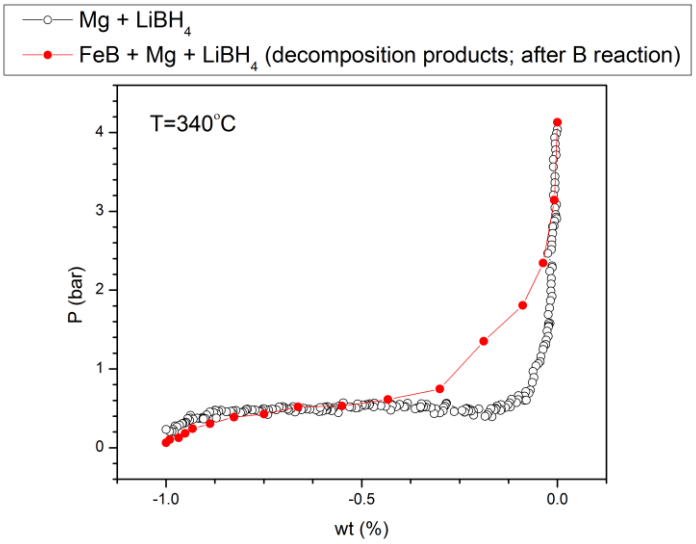

Figure 1-50. PCI decomposition of *LiBH₄+Mg* compared to the C reaction at 340 °C.

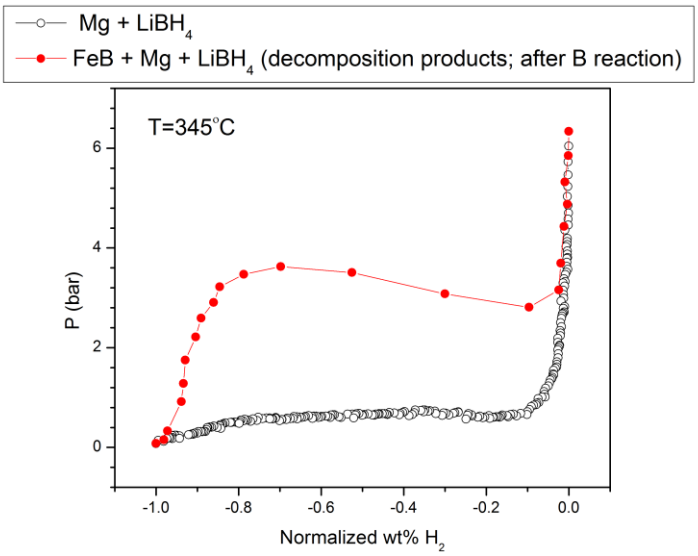

Figure 1-51. PCI decomposition of *LiBH₄+Mg* compared to the C reaction at 345 °C

At both temperatures the *LiBH₄+Mg* assemblage decomposes as pure *LiBH₄*, with no MgB_2 formation and no role of *Mg*, only below 1 bar. The *LiBH₄+Mg+FeB* system

behaves similarly at 340 °C (cf. the low temperature C process as discussed above, but it gives the expected (1-11) reaction at 345 °C with formation of MgB_2 at $p(H_2)$ = 3 bar.

Kou et al. [82] tried to explain the mechanism of MgB_2 formation from the $LiBH_4$-MgH_2 system in different dehydrogenation conditions. They conclude that the process consists of an incubation period followed by nucleus growth. Their results show that the formation process of MgB_2 is enhanced by increasing the initial dehydrogenation pressure at constant temperature. Further, the incubation period could be significantly reduced at higher temperature.

In the above cases of the $LiBH_4$+Mg and $LiBH_4$+Mg+FeB assemblages, pressure, temperature and provided incubation time are the same. The only difference is the presence of *FeB*, which therefore has to play a key catalytic role to promote the (1-11) reaction, probably providing heterogeneous sites for MgB_2 nucleation. Further studies are required to investigate the mechanism of MgB_2 formation in Mg-$LiBH_4$ and Mg_2FeH_6-$LiBH_4$ systems.

The second important effect of *FeB* is to favor the reversibility of the MgH_2-$LiBH_4$ desorption/absorption cycling.

In isothermal-isobaric kinetic desorption studies which were done on full $2LiBH_4$-Mg_2FeH_6 composite, it was found that cycling of B and C absorption/desorption does not have any practical effect on kinetic of these reactions. Figure 1-52 represents two desorption cycles of C reaction at 392 °C and 5.6 bar and two desorption cycles on Mg+$LiBH_4$ system at 421 °C and 8 bar.

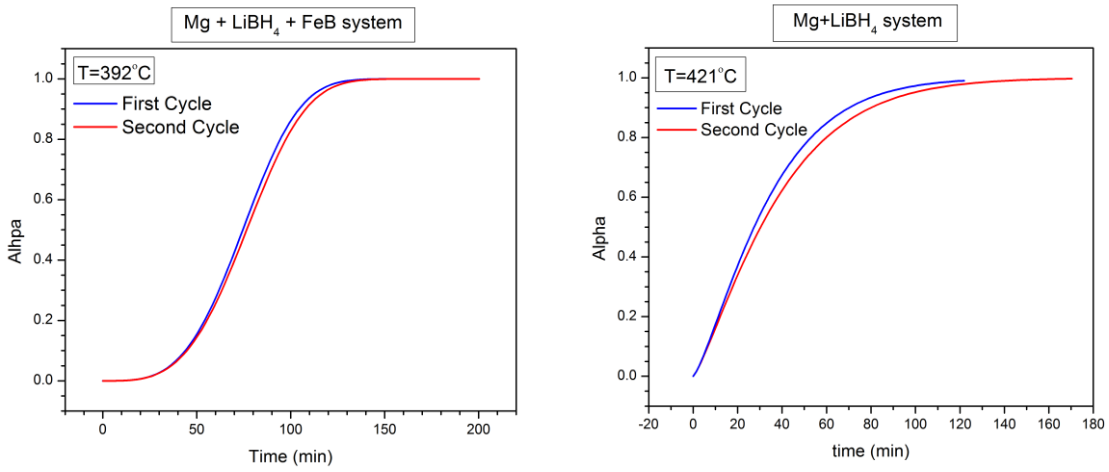

Figure 1-52. Isothermic-Isobaric dehydrogenation kinetic curves for different systems at 392 °C and 421 °C.

The corresponding kinetic parameters obtained from the fitting by Avrami model are reported in Table 1-10. The difference of rate constant for the system containing *FeB* is significantly smaller than for the other case. This can be ascribed to hydride nucleation in the *FeB* surface during the rehydrogenation cycle, so that hydride particles agglomeration would be hampered providing a better decomposition kinetic on the second desorption cycle.

Table 1-10. Kinetic Avrami parameters for the first and second cycles of the *Mg-LiBH$_4$* joint decomposition in two different systems.

$Mg + LiBH_4 + FeB$ (392 °C)		$2Mg + LiBH_4$ (421 °C)	
n_1	k_1	n_1	k_1
3.56	0.01210(3)	1.78	0.02735(25)
n_2	k_2	n_2	k_2
3.51	0.01175(5)	1.24	0.02450(15)
Δk%		Δk%	
2.89		10.42	

1.4.2 Nano confined systems

1.4.2.1 Carbon xerogel synthesis

The surface area of synthesized carbon xerogels is reported in Table 1-11. The trend of pore size and volume reduction of sample on increasing the initial *pH* is in agreement with previous studies [103, 104] As a consequence of the activation process, a larger specific surface but a constant pore diameter are observed [105].

Table 1-11. BET values of carbon xerogels prepared by different initial *pH*.

Sample name	initial pH	S_{BET} (m^2/g)	V_{micro} (cc/g)	V_{meso} (cc/g)	D_{max} (nm)	V_{tot} (cc/g)
CX-617	6.17	854	0.226	1.51	21	1.73
CX-667	6.67	935	0.221	0.91	8	1.10
CX-671	6.71	904	0.250	0.33	3	0.54
CX-617-ACT	6.17	1756	0.582	2.75	20	3.23
CX-667-ACT	6.67	2605	0.704	1.64	9	2.44

1.4.2.2 Insertion of Mg, Fe and Co into carbon xerogels

The different substances used for infiltration experiments in the xerogels, with concentrations of their solutions and infiltration time are reported in the first two columns of Table 1-12. The ideal uptake is calculated by multiplying the solution concentration by the gel specific volume, whereas the experimental one was determined by ICP analysis of the infiltrated samples. 'Scratched' and 'non-scratched' specifications refer to the surface treatment of xerogels after infiltration. By comparison of uptake values for scratched and non-scratched iron containing samples, it can be concluded that about half of the expected (ideal) *Fe* content (weight difference before and after iron infiltration) was not confined but covered the gel surface as bulk iron.

Table 1-12. Results of ICP analysis on different carbon xerogel.

Sample	Conc. (mmol/g gel)	Immersed solution conc. (M)	Gel Total Vol (cc/g)	Calculated uptake (mmol/g gel)	Exp./Calc. uptake (%)
$Mg(BU)_2$, 3M, Scratched	0.91	3.00	1.09	3.27	27.89
$Mg(BU)_2$, 1M, Scratched	0.98	1.00	1.09	1.09	90.09
$Fe(NO_3)_3$ 3h non-Scratched	0.73	0.99	1.20	1.19	61.51
$Fe(NO_3)_3$ 24h non-Scratched	0.71	0.99	1.20	1.19	59.75
$Fe(NO_3)_3$ 24h Scratched	0.33	0.99	1.20	1.19	27.39
$Co(NO_3)_2$ 24h non-Scratched	1.11	0.99	1.20	1.19	93.28

The lower value of truly confined iron and cobalt with respect to magnesium in the gel is related to the different character of the infiltration solutions. *Fe* and *Co* were contained in waster solution but magnesium dibutyl was in an organic solution. Solution uptake is due to capillary pressure inside the scaffold pores which is a function of wettability. RF carbon aerogels/xerogels are known to be hydrophobic compounds [65], so that the capillary force and uptake capability of carbon scaffolds in water media is less than in organic solutions.

By the use of magnesium dibutyl (Aldrich- 1M), the maximum theoretical amount of infiltrated magnesium hydride in this scaffold (with specific volume 1.09 $ml.g^{-1}$) is about 2.87% which means 0.22% wt% H_2 capacity. This value cannot be increased by increasing the concentration of the starting solution, because the viscosity also increases with concentration so as to affect the uptake value.

The uptake rate is fast in the case of iron solution; the maximum uptake is reached after 3 hours of immersion.

1.4.2.3 Reduction study of infiltrated iron and cobalt oxides

Iron nitrate was decomposed to iron oxide forming $\gamma - Fe_2O_3$ nanoparticles inside the carbon xerogel [106, 107]. On the basis of Ellingham diagram [108] iron oxide can be reduced to metal at 400 °C and 4 bar of H_2.

The reaction was performed and monitored by in-situ synchrotron XRD measurements in the course of temperature programmed reduction of infiltrated $\gamma - Fe_2O_3$ in 100 bar hydrogen atmosphere presented in Figure 1-53.

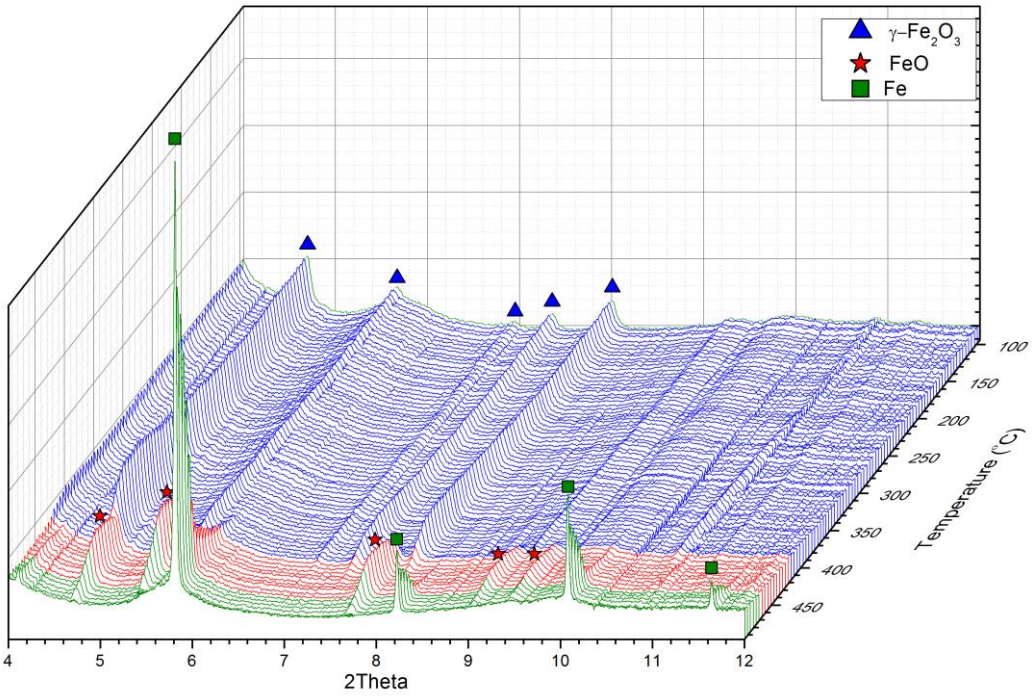

Figure 1-53. In-situ synchrotron XRD patterns for infiltrated $\gamma - Fe_2O_3$ during temperature programmed (10°C.min^{-1}) reduction in 100 bar H_2. Measurement performed at DESY, Germany (λ=0.2072 Å).

In temperature range 400 to 450 °C the first step (Figure 1-53- red area) of reduction of γ-Fe_2O_3 to FeO takes place. The reaction sequence for α-Fe_2O_3 reported in previous studies [109-111] shows the intermediate formation of Fe_3O_4; this cannot be observed here because of similarity of the XRD patterns of $\gamma - Fe_2O_3$ and Fe_3O_4. The

final step of reduction, $FeO \rightarrow Fe$ (Figure 1-53- green area), occurs in the 450-500 °C temperature range.

In the cobalt case, *CoO* is produced by decomposition of cobalt nitrate inside the carbon scaffold [112, 113]. The reduction reaction of *CoO* in 100 bar H_2 atmosphere is monitored in Figure 1-55. During heating above 140 °C the *CoO* crystallinity increases (Figure 1-54- blue area). The reduction process starts at 270 °C forming metallic cobalt (Figure 1-54- red area).

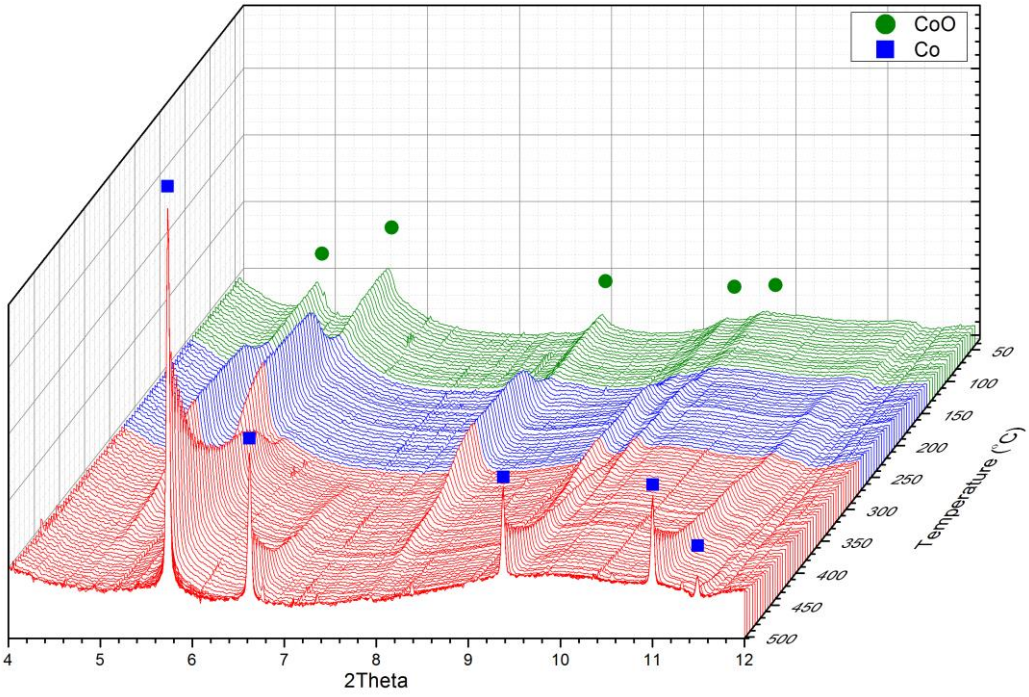

Figure 1-54. In-situ synchrotron XRD patterns of the temperature programmed (10°C.min^{-1}) reduction of infiltrated *CoO* in carbon xerogel under100 bar H_2. Measurement performed at DESY, Germany (λ=0.2072 Å).

The evolution of the synchrotron X-ray diffraction patterns during heating (5 °C min^{-1} under 100 bar of H_2) of a sample containing magnesium dibutyl and cobalt illustrated in Figure 1-55.

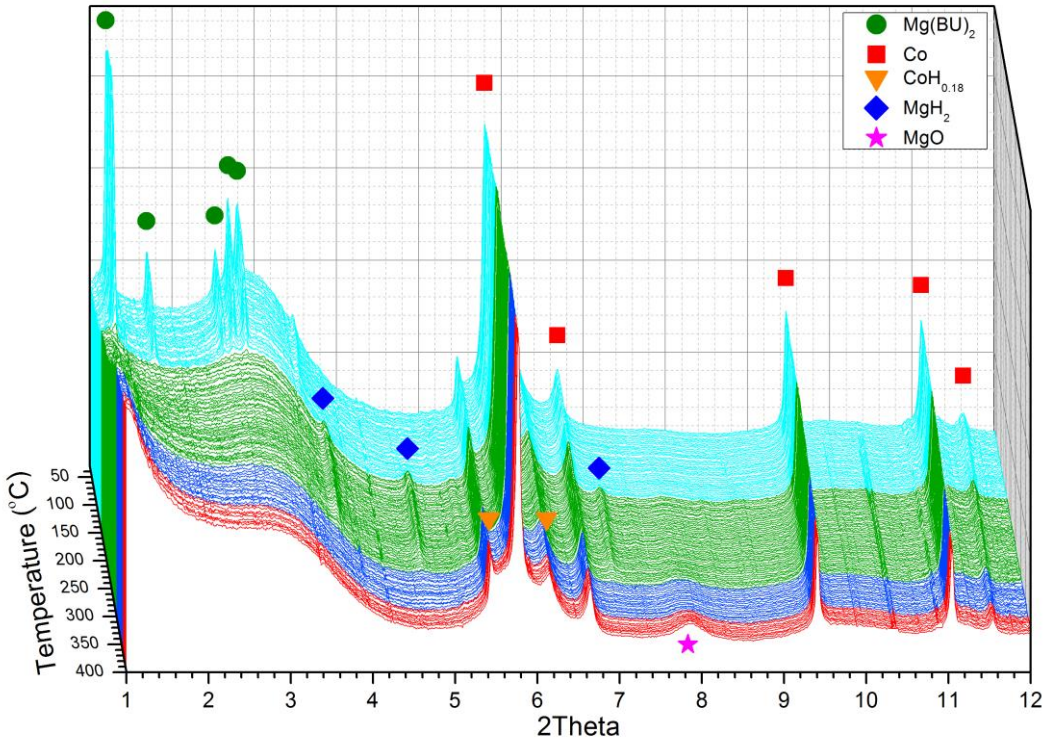

Figure 1-55. In-situ synchrotron XRD patterns of a carbon xerogel infiltrated with *Co* + *Mg(Bu)*$_2$ during temperature programmed reaction at 100 bar *H*$_2$, Measurement performed at DESY, Germany (*λ*=0.2072 Å).

The direct conversion of *Mg(Bu)*$_2$ into *MgH*$_2$ occurred about 160 °C (Figure 1-55-green area) according to the fallowing reaction:

$$Mg(C_4H_9)_2(s) + 2H_2(g) \rightarrow MgH_2(s) + 2C_4H_{10}(g) \qquad 1\text{-}30$$

Around 300 °C the peaks of magnesium hydride disappear because of an unknown reaction. The expected reaction ($Co + MgH_2 \rightarrow Mg_2CoH_5$) [114, 115] does not seem to occur, as no peaks belonging to *Mg*$_2$*CoH*$_5$ appear and also the intensities of the *Co* peaks remain the same. However, because of the small amount of *MgH*$_2$, it cannot be excluded that the peaks of the possibly formed *Mg*$_2$*CoH*$_5$ would be too weak to be detected against the high background due to the amorphous carbon scaffold.

The low uptake value of magnesium dibutyl is probably due to most open pores being saturated during the first cobalt infiltration, so that little room was left for magnesium dibutyl in the subsequent insertion.

1.4.3 Lithium amidoborane system

1.4.3.1 LiAB Synthesis

Lithium amidoborane was synthesized by ball milling a stoichiometric mixture of commercial (Sigma Aldrich) *LiH* and NH_3BH_3 for (16h with 400 rpm) in *Ar* atmosphere. The X-ray diffraction pattern of the obtained sample (Figure 1-56-a) showed the formation of $LiNH_2BH_3$ phase [48].

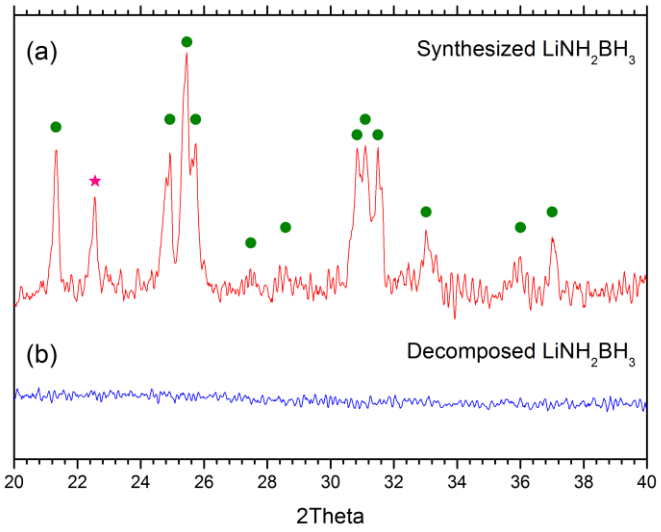

Figure 1-56- X-ray diffraction pattern (Cu-Kα radiation) of synthesized $LiNH_2BH_3$ (a) and decomposed $LiNH_2BH_3$ in 20 bar (1°C.min^{-1}) samples.
α-$LiNH_2BH_3$ (●), Postdecomposed product of $LiNH_2BH_3.3NH_3BH_3$ (▲) [48]

1.4.3.2 Dehydrogenation study on pure $LiNH_2BH_3$

Four TPD experiments were performed on *LiAB* in the Sievert's apparatus, under 1, 10, 20 and 80 bar of hydrogen pressure. The results are shown in Figure 1-57.

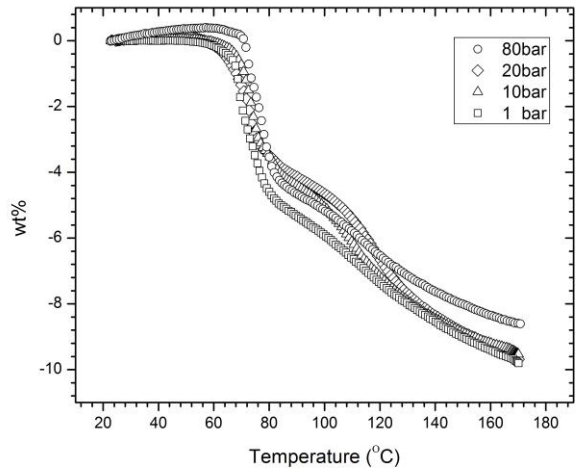

Figure 1-57. Dynamic thermal decomposition of $LiNH_2BH_3$ at different hydrogen pressures (heating rate 1 °C min^{-1} in Sievert apparatus).

In all curves two inflection points can be seen, suggesting two different reactions (A, B) during decomposition. The temperatures corresponding to inflection point are reported in Table 1-13.

Table 1-13. Inflection points temperatures calculated from TPD curve measured on $LiNH_2BH_3$ under different pressures.

Pressure (bar)	Reaction Temperature (°C)	
	A	B
1	72	118
10	73	110
20	73	117
80	73	113

The X-ray diffraction pattern of decomposed *LiAB* (Figure 1-56-b) shows that the products are fully amorphous, so that it is not possible to define the dehydrogenation reaction by this technique.

Z. Xiong et al. [50] reported an enthalpy of -3 to -5 kJ.mol^{-1}(H_2), measured by DSC method (in *Ar* flow), for the A reaction. On the basis of the van't Hoff equation and the reported enthalpy, we can calculate the expected ΔT value caused by a pressure change Δp:

$$\ln\frac{p_1}{p_2} = -\frac{\Delta H}{R}\left(\frac{1}{T_1} - \frac{1}{T_2}\right) \qquad 1\text{-}31$$

Calculated values for high H_2 pressures based on eq. 1-31 and literature enthalpy are reported in Table 1-14.

Table 1-14. Expected decomposition temperatures of *LiAB* calculated for high H_2 pressures.

Pressure (bar)	A temp. (°C)	
1	72	Fixed
10	-124	Calculated
20	-146	
80	-175	

It was found that there is a huge gap between calculated and experimental values. A similar difference between theoretical and actual temperature was also observed in case of NH_3BH_3 by F. Baitalow et al. [116], suggesting a kinetic effect on the dehydrogenation reaction.

1.4.3.3 Addition of MgH_2 and $LiBH_4$ to LiAB

The TPD experiment with 1 bar (H_2) was repeated with the *LiAB*+MgH_2 and *LiAB*+$LiBH_4$ systems. By comparing the obtained curves (Figure 1-58), MgH_2 is found to have no significant effect on the *LiAB* decomposition, as the *LiAB*+MgH_2 curve is quite similar to that of pure *LiAB*.

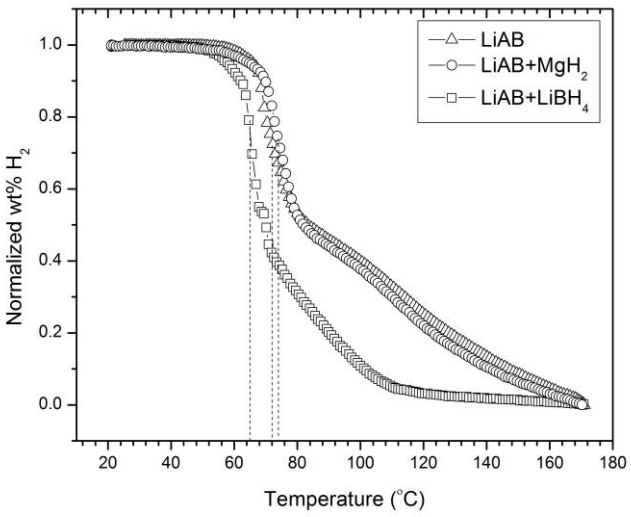

Figure 1-58. Dynamic thermal decomposition of $LiNH_2BH_3 + MgH_2$ (○), $LiNH_2BH_3 + LiBH_4$ (□) and pure $LiNH_2BH_3$ (Δ) under 1 bar hydrogen pressure (heating rate 1 °C min^{-1} in Sievert apparatus).

On the other hand, significant changes appear with the *LiAB+LiBH₄* curve. The decomposition temperature for the A process decreases by about 10 K with respect to pure *LiAB* (i). Further, a much larger loss of hydrogen follows, indicating that either the B process occurs at a lower temperature or a completely different reaction takes place (ii). These phenomena can be due to a simple catalytic effect of *LiBH₄*, acting on the same decomposition reactions experienced by pristine *LiAB*, or else a true joint decomposition of *LiAB* and *LiBH₄* may occur. To investigate this aspect, the TPD run was repeated with a different composition (*5LiAB+LiBH₄*) and the same other conditions. The resulting curve is compared to that of the *LiAB+LiBH₄* system and to that of pure *LiAB* (dashed line) in Figure 1-59. The feature (i), i.e. the decrease of temperature of the A process, is independent of the relative amount *LiBH₄/LiAB*, but the subsequent large H_2 loss (ii) is observed only when the amount of *LiBH₄* is larger (*LiAB+LiBH₄* system). We can then conclude that the latter effect, concerning the B process, is due to a real joint decomposition reaction of *LiBH₄* and lithium amidoborane.

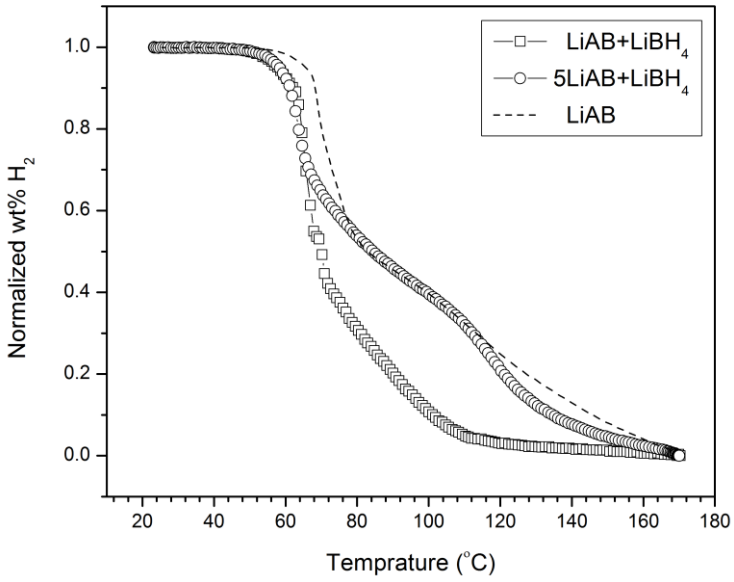

Figure 1-59. Dynamic thermal decomposition of $5LiNH_2BH_3 + LiBH_4$ (○) and $LiNH_2BH_3 + LiBH_4$ (□) under 1 bar hydrogen pressure (heating rate 1 °C.min^{-1} in Sievert apparatus).

1.5 Conclusions

The $2LiBH_4$-Mg_2FeH_6 composite has proved to undergo dehydrogenation in three distinct steps A, B, and C. Reaction A occurs well within the $p(T)$ stability regions of both pure components, with formation of the mixed compound *FeB*. Each of the two hydrides is found to be really destabilized thermodynamically by the presence of the other one in desorption conditions; the effect was shown to be of entropic rather than enthalpic nature. As an example, at 30 bar of H_2 pressure the composite should decompose at 330 °C, whereas at the same pressure Mg_2FeH_6 would release H_2 only at 455 °C, and $LiBH_4$ even at 580 °C. For comparison, also MgH_2 would require heating to 425 °C to decompose at 30 bar. This confirms that the destabilization method [33] may be quite effective in a broad chemical context. Of course, however, the wt% hydrogen yield of the composite from reaction A is smaller than the full decomposition yields of the two single hydrides. Further, below $p(H_2)$ = 100 bar the reaction A could not be reversed, so that higher pressures would be possibly necessary to re-hydrogenate *FeB*.

The B and C steps are well reversible, and they correspond to two distinct decomposition stages of the well-known $LiBH_4$-MgH_2 assemblage, according to what previously found by different experimental methods [81]. In particular, the present study provides a full thermodynamic characterization of the poorly defined second stage C (reaction of $LiBH_4$ with *Mg*).The results of the thermodynamic study of the $2LiBH_4$-Mg_2FeH_6 system were published in the Journal of Physical Chemistry C [117].

The kinetic properties of the A desorption and C desorption-absorption reactions of the $2LiBH_4$-Mg_2FeH_6 assemblage were determined by isothermal-isobaric experiments, with a particular focus on the role of overpressure and its coupling with temperature. By extending measurements to condition close to equilibrium, where reactions are very slow, a convenient range of overpressures could be covered. This allowed us to explore the kinetic effect of $\Delta p/p$ in a proper way, and to interpret the data on the basis of an exponential dependence of the reaction rate constants on overpressure. Such a result fits naturally with the conventional Arrhenius formalism, suggesting simple linear relations of activation energy and entropy with overpressure. As $\Delta p/p$ is straightforwardly

connected to the thermodynamic driving force ΔG, the empirical results found can be accounted for by a consistent theoretical frame related to that used in electrochemical kinetics. This analysis can have a broader interest for application to kinetic properties of a large class of solid-gas reactions. However, irreversibility and/or hysteresis conditions specific of these processes require extending and generalizing the approach here proposed, and further researches can be done in that direction. The study of overpressure role in the absorption/desorption kinetics was recently published in the Journal of Physical Chemistry C to complete the study of the $2LiBH_4$-Mg_2FeH_6 composite as a promising hydrogen storage material [118].

A series of experiments have been also carried out attempting to synthesize Mg_2FeH_6 and Mg_2CoH_5 in confined nanostructured form inside the pores of carbon xerogels. The encouraging results obtained refer to the stages of infiltration of the precursors (Magnesium dibutyl, and iron or cobalt nitrate) into the carbon scaffold, and of their decomposition and/or reduction to give confined magnesium hydride and metal iron or cobalt. The last part, concerning the reaction of MgH_2 with Fe or Co in H_2 atmosphere to produce the mixed hydride, will be accomplished in future work.

The other very interesting hydrogen storage system considered in this thesis is lithium amidoborane $LiNH_2BH_3$. The effect of H_2 pressure on its dynamic decomposition reaction has been studied, finding that in such conditions the dehydrogenation temperature does not decrease at high pressure, as it would be expected on the basis of the reaction enthalpy. The reasons for that have to be further investigated. Further, it has been shown that the assemblage of lithium amidoborane with lithium borohydride dehydrogenates at a lower temperature with respect to pure $LiNH_2BH_3$, owing to a probable joint decomposition reaction. This system will then be object of intense research work in the future.

2 Chemical lithiation of niobium oxide

2.1 Introduction

In the research field on rechargeable lithium batteries, an important role is played by the search for electrode materials with a medium to low discharge voltage vs. a Li^+/Li anode (2.5 to 1.0 V range). This contrasts with the well-known trend towards higher and higher cathode voltages, aiming to attain the maximum energy density (cf. the 4.8 V of the $LiNi_{0.5}Mn_{1.5}O_4$ cathode [119]), but it is motivated by two specific reasons. The first one concerns the use as anode rather than cathode, replacing the conventional LiC_6 anode vs. a high voltage cathode like the one just mentioned above [120-123]. Indeed, the electrochemical potential of conventional organic liquid-carbonate electrolytes (1.0 V) is slightly larger than that of the lithium or lithium/carbon anode, so that the carbonate would be reduced if no layer of passivating solid-electrolyte interface were formed, preventing the direct electrolyte-anode reaction. However, lithium dendrites tend to grow on that layer, leading to danger of short-circuits which may fire the flammable electrolyte [124, 125]. For this reason anodes with no passivating layer and with potentials in the 1.0 to 1.5 V range, so as to be exempt from possible interactions with the electrolyte, would be highly desirable [120-123]. An already reported stable anode of this kind is $Li_4Ti_5O_{12}$, with spinel structure, and working at a 1.5 V voltage on the basis of the Ti^{4+}/Ti^{3+} redox couple [126, 127].

The second application (1.5 to 2.5 V range) is for cathode use in batteries powering the memory backup in portable electronic devices [128, 129]. The microfabrication of integrated circuits brings about a reduction of power supply voltage to about 2 V or less, and the mismatch with a high voltage battery should be possibly avoided. That can be achieved by employing a battery cathode with electrochemical potential in the required range. With this purpose the lithium insertion reaction into Nb_2O_5 was studied electrochemically, in order to exploit the convenient potential of the Nb^{5+}/Nb^{4+} couple [128, 129]. All three main polymorphs of niobium oxide were tested, finding a

maximum capacity of 200 mAh (g-oxide)$^{-1}$ (i.e. 1.98 *Li* atoms inserted on discharge) in the voltage range 2.2 to 1.5 V vs. *Li* anode. The behaviour of the monoclinic phase is claimed to differ slightly from that of the other modifications, because a flat portion of the potential vs. capacity curve would suggest a possible two-phase character of the reaction. However, the in-situ X-ray diffraction results are not exhaustive in this respect. Significant improvements of cycling stability and high rate capability were reported on using Nb_2O_5 nanobelts as electrode material [130].

We have thus undertaken a research program to clarify the structural and electronic properties of lithiated niobium oxides, with a particular focus on the high-temperature monoclinic phase often reported in the literature as α-Nb_2O_5 or *H*-Nb_2O_5 [131, 132]; the latter notation may cause possible confusion with another polymorph with hexagonal symmetry. In order to solve the challenging structural problem (14 f.u. are contained in the unit-cell of α-Nb_2O_5) [133], an accurate neutron diffraction study of the lithiated oxide is necessary; we thus decided to perform the lithium insertion reaction chemically to obtain a sample in the required form and amount. By locating the lithium atoms in the niobium oxide framework an important insight into the mechanism of the insertion reaction was expected; further, this would provide the prerequisite knowledge for theoretical analysis of the electronic and magnetic properties of the material.

2.2 Synthesis of Nb_2O_5 polymorphs

Four different polymorphs of diniobium pentoxide were synthesized with the condition reported in Table 2-1, according to different methods reported in the literature. Orthorhombic *T-Nb_2O_5* (Aldrich) was used as starting reagent.

Table 2-1. Synthesis conditions.

Phase	Precursor	Thermal treatment	Ref.
α-Nb_2O_5	Commercial T-Nb_2O_5	1200°C for 24h	[129]
N-Nb_2O_5	NbO_2F / $Nb(OH)_5$	1100°C for 24h	[134, 135] / [136, 137]
M-Nb_2O_5	TT-Nb2O5	1000°C for 24h	[138, 139]
TT-Nb_2O_5	Peroxo-Citrato-Niobium	600°C for 24h	[140, 141]

The X-ray diffraction patterns of the obtained polymorphs are shown in Figure 2-1.

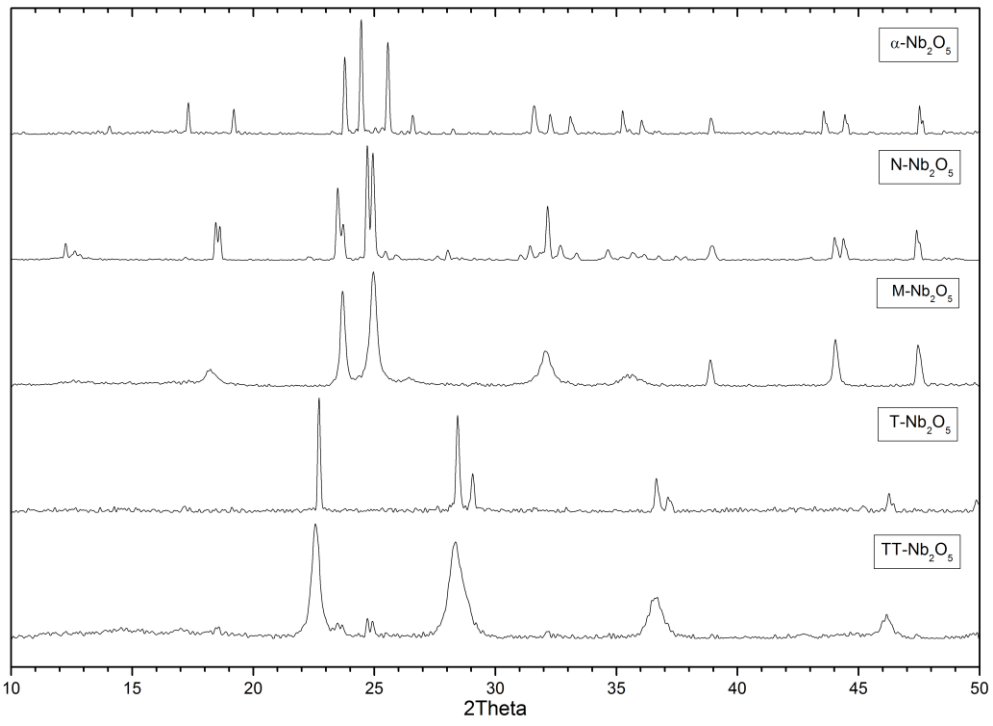

Figure 2-1. XRD pattern of different *Nb_2O_5* polymorphs (Cu-Kα radiation).

2.3 The lithium insertion reaction

Lithiation experiments were carried out by making these phases react with n-butyllithium in hexane, under N_2 flow [142] at 50 °C for 2 days. All lithiated compounds obtained, but those coming from α-Nb_2O_5, were poorly crystalline and not suitable for diffraction studies. Therefore the α-Nb_2O_5 phase was selected to continue our study on chemical lithiation.

With the α phase, the reaction at 50 °C for 60 h produced a black powder, which was filtered, washed repeatedly with hexane and dried in a glove-box with re-circulated *Ar* atmosphere.

It was then found that the amount of inserted lithium is a function of lithiation time at constant temperature (50°C). The powders change to black immediately after n-butyllithium injection, suggesting a fast lithium insertion. To determine the rate of lithiation quantitatively, samples were removed after selected reaction times to measure their lithium content. In Figure 2-2 the lithium content, determined by flame photometry, is plotted vs. lithiation time at 50 °C.

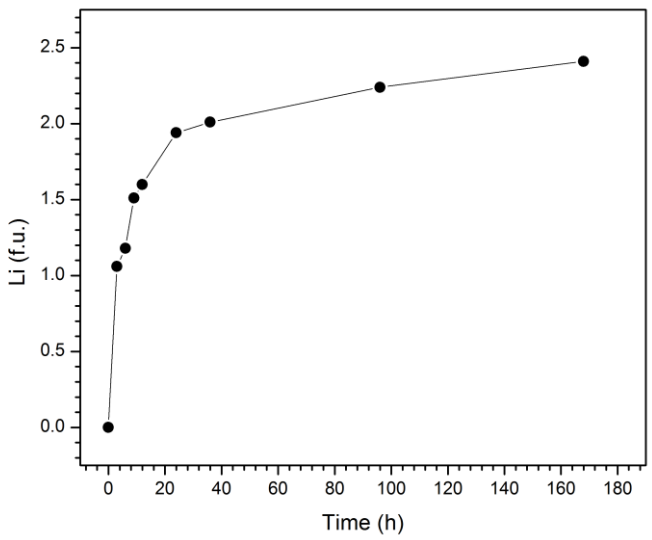

Figure 2-2. Number of inserted lithium atoms per Nb_2O_5 formula unit vs. lithiation time.

2.4 Structure properties

Neutron diffraction measurements

Powder neutron diffractometers are very large in comparison to laboratory X-ray instruments as shown by the scale in the figure below, which shows the layout of the high-resolution powder neutron diffractometer D2B at the ILL. The term high-resolution refers not to the smallest peak width in the powder diffraction pattern, but to the fact that the instrumental resolution function results in narrow peaks at high scattering angle. This is achieved by having large monochromator take-off angle as shown in the Figure 2-3, which for this instrument is 135°. The layout of the instrument is "Debye-Scherrer" in the sense that it uses a cylindrical sample with transmission geometry.

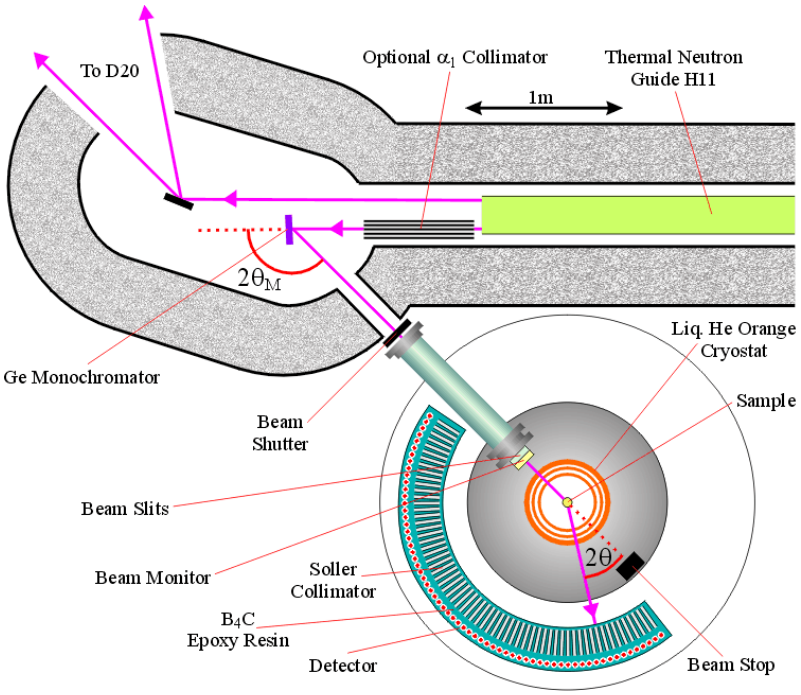

Figure 2-3. Top-view schematic of the D20 neutron diffractometer at the ILL [143].

With the detector bank placed so that the configuration of incident, monochromated, and diffracted beams is "Z" shaped, a focusing effect occurs: this produces a minimum in the resolution function for the diffractometer at high scattering angle as shown in the next figure. The resolution function is determined from the full-

width of the peaks at half-maximum height (FWHM) as a function of scattering angle from a standard sample.

In order to achieve high resolution, the instrument must be able to count neutrons with a very precise Bragg angle. This is achieved by the use of Soller collimators placed in front of each detector. Finally, given the relatively low flux available at neutron sources, instrument efficiency is greatly improved by using many detectors at the same time: the early powder neutrons diffractometers used only a single detector; while the high-resolution powder diffractometer at the ILL, D2B, is designed with 64 detectors so as to cover virtually the entire 2θ range.

The instruments function in a similar way to that of a laboratory diffractometer in that the detector bank of n detectors is step scanned in 2θ. In principle, a complete diffraction pattern can be obtained by just stepping through a 2θ range that is equal to the detector separation angle, which is 2.5° for D2B [143].

A sample of 3 g of $Li_{1.714}Nb_2O_5$ was loaded into a vanadium can which was sealed with indium wire in *Ar* atmosphere. Data were collected in the 5-160° 2θ range on the high-resolution ($\Delta d/d$ =5x10^{-4}) D2B powder diffractometer at the neutron source (nuclear reactor) of the Institut-Laue-Langevin (Grenoble, France). A primary beam monochromator of 28 Ge(115) crystals, set at λ = 1.595 Å, was employed.

Structure analysis

All calculations for determining and analysing the crystal structure were carried out by the GSAS computer package [79, 144].The intensity background was modeled by six Chebyshev polynomials, and the peak shape was represented by a pseudo-Voigt function (linear combination of Gaussian and Lorentzian components, with σ and γ half-widths, respectively). The σ and γ parameters vary with θ as $\sigma = (U\,tan^2\theta + V\,tan\theta + W + P/cos^2\theta)^{1/2}$ and $\gamma = X/cos\theta + Y\,tan\theta$; the U, V and W coefficients are mainly related to instrumental resolution [145], *P* and *X* are the Scherrer coefficients for Gaussian and Lorentzian particle size broadening, respectively, and Y is related to particle strain broadening. The mixing coefficient and the full width of the

pseudo-Voigt function depend on σ and γ according to equations given in the literature [146].

By X-ray diffractometry (with a protected sample holder) a single-phase pattern was obtained which could be indexed according to the monoclinic unit-cell a = 20.800, b = 4.134, c = 19.116 Å, β = 119.54°, similar to that reported previously for $Li_{1.9}Nb_2O_5$ [142]. Chemical analysis by atomic emission flame photometry gave a Li content of 1.8 *Li* per f.u., but the $Li_{1.714}Nb_2O_5$ chemical formula was retained because consistent with the results of the structure determination by neutron diffraction.

A Rietveld refinement of the crystal structure was started from the atomic coordinates of *Nb* and *O* atoms of α-Nb_2O_5 in space group *P2/m* [133] with isotropic displacement factors. This structural model implies that all atoms are in special positions on mirror planes (*y* coordinates either 0 or ½), except for the Nb1 atom in tetrahedral coordination which is disordered with occupancy 0.5. After reaching convergence a difference Fourier map was computed, revealing the positions of 12 negative peaks in the asymmetric unit in special positions on mirror planes. These could be interpreted as *Li* atoms on the basis of their distances to first neighbours, and their coordinates were included in the refinement successfully. Restraints on the *Nb-O* and *Li-O* distances had to be introduced, in order to prevent some of these bonds to become too short. A subsequent difference Fourier map did not show any negative peaks with crystal-chemical surroundings suitable for additional *Li* atoms. Therefore, the $Li_{1.714}Nb_2O_5$ chemical composition consistent with 24 *Li* atoms per unit-cell (with 14 formula units) was accepted.

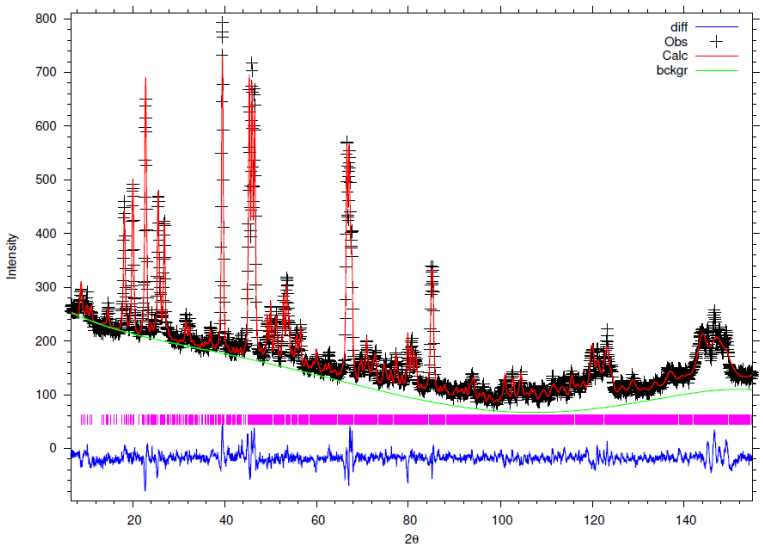

Figure 2-4. Neutron powder diffraction pattern (ILL-D2B, λ=1.5951 Å) of $Li_{1.714}Nb_2O_5$; observed, Rietveld calculated and difference intensity profiles are plotted vs. the 2θ angle (°).

Table 2-2. Rietveld refinement results of neutron diffraction data for $Li_{1.714}Nb_2O_5$ (space group *P2*, Z=14); the e.s.d.'s are reported in parentheses

	$Li_{1.714}Nb_2O_5$	α-Nb_2O_5
	Refined values	Reported values[133]
a (Å)	20.7914(9)	21.153(7)
b (Å)	4.1346(2)	3.8233(5)
c (Å)	19.1318(9)	19.356(5)
β (°)	119.571(3)	119.80(2)
V (Å^3)	1430.42	1358.30
Data	2969	
Variables	220	
wR_p	0.0447	
R_p	0.0347	
$R(F^2)$	0.0285	
Red. $\chi 2$	3.922	

At this stage we decided to test the lower symmetry *P2* space group, in order to remove the severe geometric constraint of mirror symmetry on the *Li* atoms, which may prevent them from attaining the most favourable bonding environment. The origin on the twofold polar axis was fixed at *y*(Nb2) = 0, and the Nb1 atom became ordered with full occupancy. Improved refinement results were obtained with respect to *P2/m*

symmetry, and eventually convergence was attained with the agreement factors and unit-cell constants given in Table 2-2. Another attempt to find additional *Li* atoms in a difference Fourier map failed. Observed, calculated and difference intensity profiles obtained after the final cycle are shown in Figure 2-4. The list of refined atomic fractional coordinates and displacement factors is reported in Table 2-3.

Table 2-3. Refined atomic fractional coordinates and displacement factors of $Li_{1.714}Nb_2O_5$, with e.s.d.'s in parentheses.

Atom name	x	y	z	$U(10^2Å^2)$
Nb1	0	0.265(30)	0	80
Nb2	0.5	0.0000	0.5	0(1)
Nb3	0.1506(31)	0.008(26)	0.9765(34)	8(2)
Nb4	0.240(4)	0.950(27)	0.237(4)	40
Nb5	0.2956(22)	0.014(20)	0.4574(22)	1(1)
Nb6	0.3569(34)	0.973(26)	0.026(4)	14(4)
Nb7	0.4217(28)	0.955(19)	0.2498(28)	5(2)
Nb8	0.5738(16)	0.983(19)	0.0717(17)	0.1
Nb9	0.6349(17)	0.977(19)	0.3152(18)	0.1
Nb10	0.1044(18)	0.471(19)	0.1978(20)	0.1
Nb11	0.167(4)	0.491(30)	0.427(4)	18(4)
Nb12	0.6829(17)	0.474(18)	0.0981(18)	0.1
Nb13	0.7574(19)	0.448(18)	0.3383(20)	0.1
Nb14	0.8927(24)	0.491(18)	0.1446(26)	3(1)
Nb15	0.9655(22)	0.435(17)	0.3888(21)	2(1)
O1	0	0.456(35)	0.5	5(3)
O2	0.5	0.560(15)	0.5	0.1
O3	0.1237(27)	0.978(23)	0.209(4)	12(4)
O4	0.1807(29)	0.011(24)	0.4323(30)	3(2)
O5	0.1902(23)	0.929(16)	0.1104(25)	0.1
O6	0.2600(18)	0.987(17)	0.3353(19)	0.1
O7	0.2521(18)	0.951(19)	0.0057(20)	0.1
O8	0.3210(23)	0.041(18)	0.2366(26)	2(1)
O9	0.4006(26)	0.116(19)	0.4796(32)	4(2)
O10	0.3922(20)	0.025(18)	0.1462(21)	0.1
O11	0.472(4)	0.989(25)	0.3828(31)	11(3)
O12	0.4628(30)	0.072(23)	0.049(4)	11(4)
O13	0.5292(17)	0.047(17)	0.2742(22)	0.1
O14	0.6106(27)	0.031(21)	0.1905(25)	2(1)

O15	0.6632(19)	0.006(18)	0.4278(20)	0.1
O16	0.6870(28)	0.987(21)	0.1041(29)	3(1)
O17	0.7575(19)	0.011(18)	0.3455(23)	0.1
O18	0.895(4)	0.999(19)	0.1574(30)	8(3)
O19	0.9572(19)	0.009(18)	0.0425(22)	0.1
O20	0.9514(32)	0.957(18)	0.3693(29)	6(2)
O21	0.0715(18)	0.510(19)	0.0816(18)	12(4)
O22	0.0695(18)	0.480(20)	0.4046(20)	0.1
O23	0.1371(19)	0.506(19)	0.3143(20)	0.1
O24	0.2176(21)	0.450(17)	0.2266(22)	0.1
O25	0.2829(21)	0.526(17)	0.4553(19)	0.1
O26	0.3493(21)	0.502(19)	0.0145(25)	1(1)
O27	0.4267(26)	0.472(17)	0.260(4)	4(2)
O28	0.5712(20)	0.492(19)	0.0725(22)	0.1
O29	0.6421(24)	0.469(19)	0.3207(27)	3(2)
O30	0.7129(21)	0.505(20)	0.2274(21)	0.1
O31	0.7774(29)	0.462(22)	0.4508(26)	10(3)
O32	0.8009(21)	0.494(20)	0.1362(26)	2(1)
O33	0.8535(23)	0.520(19)	0.3525(28)	2(1)
O34	0.8484(21)	0.481(20)	0.0140(21)	0.1
O35	0.9347(17)	0.453(17)	0.2721(18)	0.1
O36	0.990(4)	0.531(26)	0.172(4)	14(5)
Li1	0.371(4)	0.01(4)	0.353(4)	0.1
Li2	0.754(4)	0.970(27)	0.445(4)	0.1
Li3	0.866(4)	0.040(23)	0.406(5)	0.1
Li4	0.294(4)	0.136(29)	0.125(5)	0.1
Li5	0.726(6)	0.008(29)	0.233(5)	7(7)
Li6	0.171(5)	0.408(24)	0.107(5)	0.1
Li7	0.966(5)	0.963(25)	0.280(4)	0.1
Li8	0.043(4)	0.380(28)	0.277(5)	0.1
Li9	0.253(4)	0.483(25)	0.352(4)	0.1
Li10	0.666(5)	0.506(25)	0.436(4)	0.1
Li11	0.515(4)	0.550(23)	0.278(7)	0.1
Li12	0.470(4)	0.589(26)	0.050(6)	0.1

One can see by the agreement factors in Table 2-2 and by Figure 2-4 that the fit of data is quite good; however, the e.s.d.'s of atomic coordinates are larger than desirable, particularly for the *y* values. This is yet not unexpected, despite the high quality of the experimental measurements and equipment, taking into account the large number of refined parameters due to the structure complexity (number of observations to number

of variables ratio as low as 13.5). The particularly large e.s.d.'s of the *y* coordinates are related to the strong *P2/m* pseudo-symmetry of the structure, which introduces significant atomic positional correlations along [010] normal to the pseudo-plane. Other features of the results which are not fully satisfactory concern some of the displacement factors. Those of Nb1 and Nb4 had to be fixed at quite large values; as Nb1 lies on the twofold symmetry axis, its large apparent thermal motion suggests that the symmetry should be possibly lowered to *P1*. Other values were fixed to 0.1 to prevent them from becoming negative.

On comparing the unit-cell geometry of lithiated to unlithiated niobium oxide (Table 1), a significant volume expansion (+5.3%) is observed, as expected. However, the effect is highly anisotropic, as all the expansion is concentrated along the [010] direction (+8.1%), whereas the *a* and *c* cell edges even contract by -1.7 and -1.2%, respectively, on lithium insertion.

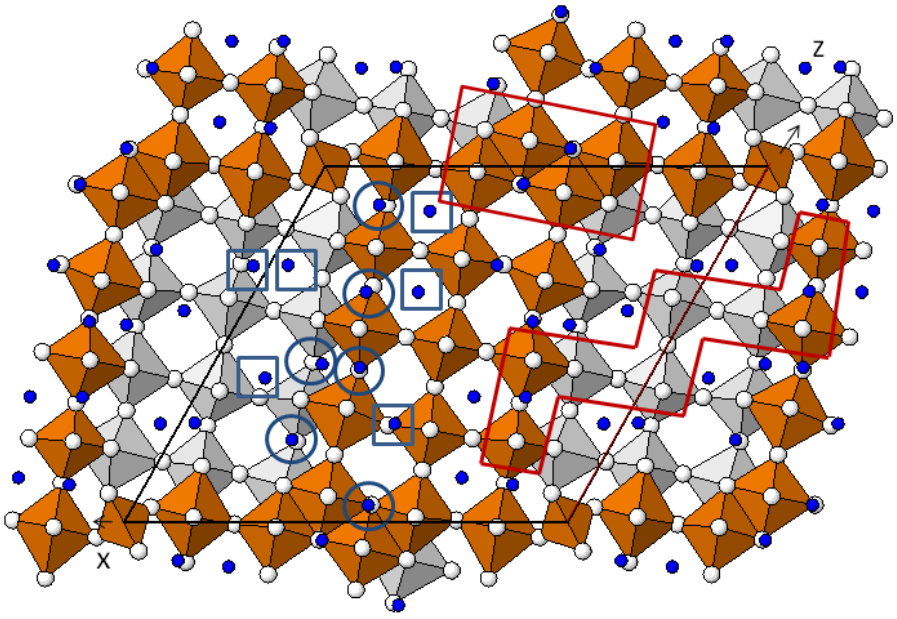

Figure 2-5. Projection onto (010) of the *P2* structure of $Li_{1.714}Nb_2O_5$, from Rietveld refinement of neutron diffraction data. NbO_6 coordination octahedra are shown; circles and squares emphasize fivefold- and fourfold-coordinated Li atoms, respectively. For the two large encirclements, see the text.

Indeed, the most interesting feature of the refined crystal structure of $Li_{1.714}Nb_2O_5$ is the distribution of *Li* atoms in the framework of niobium oxide (Figure 2-5). In perovskite-related structures, the preferred lithium sites are known to lie close to the square windows delimiting the cube-octahedral cages typical of these arrangements. In such cases, *Li* lies close to the window center with a flat square pyramidal coordination: cf. the example of lithium-lanthanum-titanate (LLTO) [133]. However, Nb_2O_5 phases show an additional feature not present in the perovskite-type, but rather in the rutile-type arrangement, i.e. double planes parallel to [010] of NbO_6 octahedra sharing edges (Figure 2-5). Thus, *Li* atoms near windows in such planes acquire an extra contact with an *O* atom belonging to the neighbouring plane, so as to raise their C.N. from 4 to 5 (Figure 2-6). In the structure of lithiated Nb_2O_5 there are, therefore, two kinds of possible *Li* sites: the tetracoordinated perovskite-type ones, and those which are pentacoordinated. These sites can be counted: there are 16 of the first and 11 of the second type per asymmetric unit.

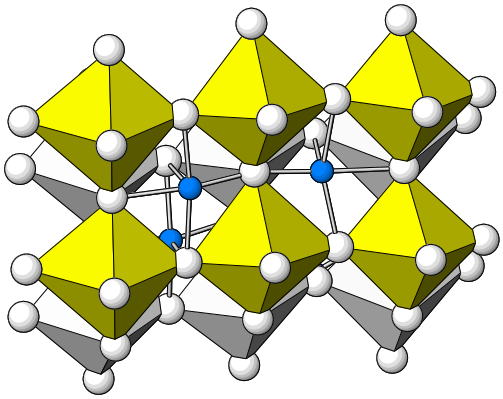

Figure 2-6. Crystal-chemical environment of fivefold-coordinated *Li* atoms in the structure of $Li_{1.714}Nb_2O_5$.

In the structure of $Li_{1.714}Nb_2O_5$ there are 6 *Li* atoms with C.N.= 5 and 6 with C.N.=4; they are denoted by circles and squares, respectively, in Figure 2-5. The higher ratio of the number of fivefold- to fourfold-coordinated Li atoms (1:1) with respect to the average value (1:1.5) is consistent with the lower energy of the former class of *Li* sites, as suggested by obvious bonding considerations. However, entropic factors and

non-equilibrium kinetic conditions of the lithiation reaction can also account for the significant observed fraction of *Li* atoms with C.N.=4.

The statistical distribution of *Li-O* bond distances (Figure 2-7) appears to be quite asymmetric, with a fall above the most populated range (2.1 to 2.2 Å). Shorter bonds are more populated than longer bonds, so as to depress the mean value (2.064 Å) below that range. This feature is common to both fourfold and fivefold coordinated Li atoms, whose partial distributions are not very dissimilar from the overall one. A comparable situation is observed also for the distribution of *Nb-O* bond lengths, which is plotted in Figure 2-8 with exclusion of the shorter bonds of tetrahedrally coordinated Nb1 (1.81 Å x2 and 1.84 Å x2). Again the observed mean and median (2.056 Å) is smaller than the abscissa of the maximum (2.15 Å), giving rise to a skewed distribution.

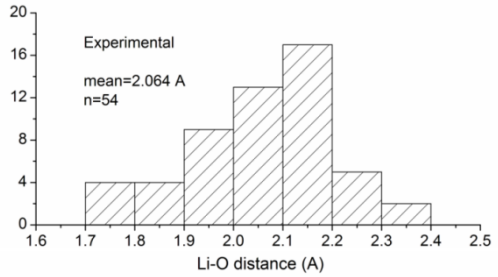

Figure 2-7. Statistical distribution of the *Li-O* bond lengths from fivefold- and fourfold-coordinated *Li* atoms in the structure of $Li_{1.714}Nb_2O_5$.

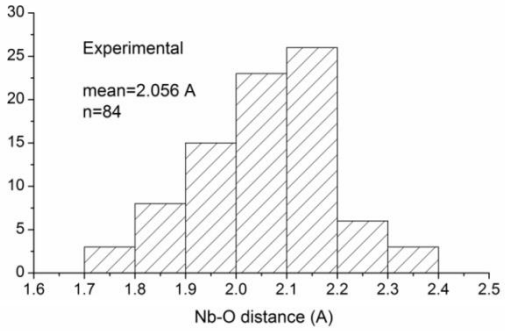

Figure 2-8. Statistical distribution of the *Nb-O* bond lengths from NbO_6 coordination octahedra in the structure of $Li_{1.714}Nb_2O_5$.

2.5 Conclusion

Chemical lithiation on monoclinic α-Nb_2O_5 has been performed, so as to mimic the corresponding electrochemical reaction during discharge vs. a lithium anode, or charge vs. a high voltage cathode. The lithium atom distribution in the $Li_{1.714}Nb_2O_5$ product of *Li* insertion into niobium oxide has been determined by neutron diffraction. Lower energy fivefold- and a higher energy fourfold- coordinated sites are occupied by lithium in the reaction course; the former ones are more but not exclusively populated, indicating that entropic in addition to energetic factors play a substantial role in the insertion process. The results on structural properties of $Li_{1.714}Nb_2O_5$, together with first principle calculations of its electronic behaviour, have been recently published on the Journal of Physical Chemistry-Chemical Physics [147].

3 References

1. Momirlan, M., L. Muresan, A.A.M. Sayigh, and T.N. Veziroglu, *The use of solar energy in hydrogen production.* Renewable Energy, 1996. **9**(1–4): p. 1258-1261.

2. Ni, M., M.K.H. Leung, and D.Y.C. Leung, *Technological development of hydrogen production by solid oxide electrolyzer cell (SOEC).* International Journal of Hydrogen Energy, 2008. **33**(9): p. 2337-2354.

3. Dell, R.M. and D.A.J. Rand, *Energy storage — a key technology for global energy sustainability.* Journal of Power Sources, 2001. **100**(1–2): p. 2-17.

4. Conte, M., A. Iacobazzi, M. Ronchetti, and R. Vellone, *Hydrogen economy for a sustainable development: state-of-the-art and technological perspectives.* Journal of Power Sources, 2001. **100**(1–2): p. 171-187.

5. (DOE), U.S.D.o.E. *Fuel Cell Technologies Office Multi-Year Research, Development and Demonstration Plan*. 2013; Available from: http://www1.eere.energy.gov/hydrogenandfuelcells/mypp/pdfs/storage.pdf.

6. Tozzini, V. and V. Pellegrini, *Prospects for hydrogen storage in graphene.* Physical Chemistry Chemical Physics, 2013. **15**(1): p. 80-89.

7. Züttel, A., *Hydrogen storage methods.* Naturwissenschaften, 2004. **91**(4): p. 157-172.

8. Lynch, S.P., *Environmentally assisted cracking: Overview of evidence for an adsorption-induced localised-slip process.* Acta Metallurgica, 1988. **36**(10): p. 2639-2661.

9. Wolf, J., *Liquid-Hydrogen Technology for Vehicles.* MRS Bulletin, 2002. **27**(09): p. 684-687.

10. Aceves, S.M., G.D. Berry, J. Martinez-Frias, and F. Espinosa-Loza, *Vehicular storage of hydrogen in insulated pressure vessels.* International Journal of Hydrogen Energy, 2006. **31**(15): p. 2274-2283.

11. Ahluwalia, R.K. and J.K. Peng, *Dynamics of cryogenic hydrogen storage in insulated pressure vessels for automotive applications.* International Journal of Hydrogen Energy, 2008. **33**(17): p. 4622-4633.

12. Scanlon, L.G., et al., *Hydrogen Storage Based on Physisorption.* The Journal of Physical Chemistry B, 2009. **113**(14): p. 4708-4717.

13. Walker, G., M. Institute of Materials, and Mining, *Solid-state hydrogen storage: materials and chemistry*. 2008: Woodhead Publishing.

14. Yoon, M., S. Yang, E. Wang, and Z. Zhang, *Charged Fullerenes as High-Capacity Hydrogen Storage Media.* Nano Letters, 2007. **7**(9): p. 2578-2583.

15. Vasil'ev, Y.V., A. Hirsch, R. Taylor, and T. Drewello, *Hydrogen storage on fullerenes: hydrogenation of C59N[radical dot] using $C_{60}H_{36}$ as the source of hydrogen.* Chemical Communications, 2004(15): p. 1752-1753.

16. Dillon, A.C., K.M. Jones, T.A. Bekkedahl, C.H. Kiang, D.S. Bethune, and M.J. Heben, *Storage of hydrogen in single-walled carbon nanotubes.* Nature, 1997. **386**(6623): p. 377-379.

17. Becher, M., et al., *Hydrogen storage in carbon nanotubes.* Comptes Rendus Physique, 2003. **4**(9): p. 1055-1062.

18. Patchkovskii, S., J.S. Tse, S.N. Yurchenko, L. Zhechkov, T. Heine, and G. Seifert, *Graphene nanostructures as tunable storage media for molecular hydrogen.* Proceedings of the National Academy of Sciences of the United States of America, 2005. **102**(30): p. 10439-10444.

19. Spyrou, K., D. Gournis, and P. Rudolf, *Hydrogen Storage in Graphene-Based Materials: Efforts Towards Enhanced Hydrogen Absorption.* ECS Journal of Solid State Science and Technology, 2013. **2**(10): p. M3160-M3169.

20. Juan-Juan, J., J.P. Marco-Lozar, F. Suárez-García, D. Cazorla-Amorós, and A. Linares-Solano, *A comparison of hydrogen storage in activated carbons and a metal–organic framework (MOF-5).* Carbon, 2010. **48**(10): p. 2906-2909.

21. Li, J., S. Cheng, Q. Zhao, P. Long, and J. Dong, *Synthesis and hydrogen-storage behavior of metal–organic framework MOF-5.* International Journal of Hydrogen Energy, 2009. **34**(3): p. 1377-1382.

22. Hirscher, M. and K. Hirose, *Handbook of Hydrogen Storage: New Materials for Future Energy Storage*. 2010: Wiley.

23. Edwards, P.P., V.L. Kuznetsov, and W.I.F. David, *Hydrogen energy.* Philosophical Transactions of the Royal Society A: Mathematical, Physical and Engineering Sciences, 2007. **365**(1853): p. 1043-1056.

24. Bogdanović, B., K. Bohmhammel, B. Christ, A. Reiser, K. Schlichte, R. Vehlen, and U. Wolf, *Thermodynamic investigation of the magnesium–hydrogen system.* Journal of Alloys and Compounds, 1999. **282**(1–2): p. 84-92.

25. Bloch, J., *The kinetics of a moving metal hydride layer*. Journal of Alloys and Compounds, 2000. **312**(1–2): p. 135-153.

26. Wang, C.S., X.H. Wang, Y.Q. Lei, C.P. Chen, and Q.D. Wang, *The hydriding kinetics of $MlNi_5$—I. Development of the model.* International Journal of Hydrogen Energy, 1996. **21**(6): p. 471-478.

27. Martin, M., C. Gommel, C. Borkhart, and E. Fromm, *Absorption and desorption kinetics of hydrogen storage alloys.* Journal of Alloys and Compounds, 1996. **238**(1–2): p. 193-201.

28. Jang, M., *Nanostructured complex hydride systems for solid state hydrogen storage*, in Department of Mechanical Engineering, 2011, University of Waterloo. p. 222.

29. Züttel, A., A. Borgschulte, and L. Schlapbach, *Hydrogen as a Future Energy Carrier*. 2011: Wiley.

30. Yang, J., A. Sudik, C. Wolverton, and D.J. Siegel, *High capacity hydrogen storage materials: attributes for automotive applications and techniques for materials discovery.* Chemical Society Reviews, 2010. **39**(2): p. 656-675.

31. Reilly, J.J. and R.H. Wiswall, *Reaction of hydrogen with alloys of magnesium and nickel and the formation of Mg_2NiH_4.* Inorganic Chemistry, 1968. **7**(11): p. 2254-2256.

32. Walker, G.S., D.M. Grant, T.C. Price, X. Yu, and V. Legrand, *High capacity multicomponent hydrogen storage materials: Investigation of the effect of stoichiometry and decomposition conditions on the cycling behaviour of $LiBH_4$–MgH_2.* Journal of Power Sources, 2009. **194**(2): p. 1128-1134.

33. Vajo, J.J., T.T. Salguero, A.F. Gross, S.L. Skeith, and G.L. Olson, *Thermodynamic destabilization and reaction kinetics in light metal hydride systems.* Journal of Alloys and Compounds, 2007. **446-447**: p. 409-414.

34. Vajo, J.J., S.L. Skeith, and F. Mertens, *Reversible Storage of Hydrogen in Destabilized $LiBH_4$.* The Journal of Physical Chemistry B, 2005. **109**(9): p. 3719-3722.

35. Sakintuna, B., F. Lamari-Darkrim, and M. Hirscher, *Metal hydride materials for solid hydrogen storage: A review.* International Journal of Hydrogen Energy, 2007. **32**(Compendex): p. 1121-1140.

36. Zaluska, A., L. Zaluski, and J.O. Ström–Olsen, *Nanocrystalline magnesium for hydrogen storage.* Journal of Alloys and Compounds, 1999. **288**(1–2): p. 217-225.

37. Wagemans, R.W.P., J.H. van Lenthe, P.E. de Jongh, A.J. van Dillen, and K.P. de Jong, *Hydrogen Storage in Magnesium Clusters: Quantum Chemical Study.* Journal of the American Chemical Society, 2005. **127**(47): p. 16675-16680.

38. Aguey-Zinsou, K.F., J.R. Ares Fernandez, T. Klassen, and R. Bormann, *Effect of Nb_2O_5 on MgH_2 properties during mechanical milling.* International Journal of Hydrogen Energy, 2007. **32**(13): p. 2400-2407.

39. Nielsen, T.K., K. Manickam, M. Hirscher, F. Besenbacher, and T.R. Jensen, *Confinement of MgH_2 Nanoclusters within Nanoporous Aerogel Scaffold Materials.* ACS Nano, 2009. **3**(11): p. 3521-3528.

40. Khrussanova, M., M. Terzieva, P. Peshev, I. Konstanchuk, and E. Ivanov, *Hydriding Kinetics of Mixtures Containing Some 3d-Transition Metal Oxides and Magnesium*, in *Zeitschrift für Physikalische Chemie*1989. p. 1261.

41. Dornheim, M., S. Doppiu, G. Barkhordarian, U. Boesenberg, T. Klassen, O. Gutfleisch, and R. Bormann, *Hydrogen storage in magnesium-based hydrides and hydride composites.* Scripta Materialia, 2007. **56**(Compendex): p. 841-846.

42. Davis, W.D., L.S. Mason, and G. Stegeman, *The Heats of Formation of Sodium Borohydride, Lithium Borohydride and Lithium Aluminum Hydride.* Journal of the American Chemical Society, 1949. **71**(8): p. 2775-2781.

43. Yang, J., A. Sudik, and C. Wolverton, *Destabilizing $LiBH_4$ with a Metal (M = Mg, Al, Ti, V, Cr, or Sc) or Metal Hydride (MH_2 = MgH_2, TiH_2, or CaH_2).* The Journal of Physical Chemistry C, 2007. **111**(51): p. 19134-19140.

44. Luo, C., H. Wang, T. Sun, and M. Zhu, *Enhanced dehydrogenation properties of $LiBH_4$ compositing with hydrogenated magnesium-rare earth compounds.* International Journal of Hydrogen Energy, 2012. **37**(18): p. 13446-13451.

45. Kim, K.-B., J.-H. Shim, Y.W. Cho, and K.H. Oh, *Pressure-enhanced dehydrogenation reaction of the $LiBH_4$-YH_3 composite.* Chemical Communications, 2011. **47**(35): p. 9831-9833.

46. Vajo, J.J., W. Li, and P. Liu, *Thermodynamic and kinetic destabilization in $LiBH_4$/Mg_2NiH_4: promise for borohydride-based hydrogen storage.* Chemical Communications, 2010. **46**(36): p. 6687-6689.

47. Bogdanovic, B., A. Reiser, K. Schlichte, B. Spliethoff, and B. Tesche, *Thermodynamics and dynamics of the Mg-Fe-H system and its potential for thermochemical thermal energy storage.* J. Alloys Compd., 2002. **345**(1-2): p. 77-89.

48. Wu, C., G. Wu, Z. Xiong, W.I.F. David, K.R. Ryan, M.O. Jones, P.P. Edwards, H. Chu, and P. Chen, *Stepwise Phase Transition in the Formation of Lithium*

Amidoborane. Inorg. Chem. (Washington, DC, U. S.), 2010. **49**(Copyright (C) 2012 American Chemical Society (ACS). All Rights Reserved.): p. 4319-4323.

49. Wolf, G., J. Baumann, F. Baitalow, and F.P. Hoffmann, *Calorimetric process monitoring of thermal decomposition of B-N-H compounds.* Thermochim. Acta, 2000. **343**(Copyright (C) 2012 American Chemical Society (ACS). All Rights Reserved.): p. 19-25.

50. Xiong, Z., et al., *High-capacity hydrogen storage in lithium and sodium amidoboranes.* Nat. Mater., 2008. **7**(Copyright (C) 2012 American Chemical Society (ACS). All Rights Reserved.): p. 138-141.

51. Wu, H., W. Zhou, and T. Yildirim, *Alkali and alkaline-earth metal amidoboranes: structure, crystal chemistry, and hydrogen storage properties.* J Am Chem Soc, 2008. **130**(Copyright (C) 2012 U.S. National Library of Medicine.): p. 14834-9.

52. Varin, R.A., T. Czujko, and Z.S. Wronski, *Nanomaterials for Solid State Hydrogen Storage*. 2009: Springer.

53. Bérubé, V., G. Radtke, M. Dresselhaus, and G. Chen, *Size effects on the hydrogen storage properties of nanostructured metal hydrides: A review.* International Journal of Energy Research, 2007. **31**(6-7): p. 637-663.

54. Zaluski, L., A. Zaluska, and J.O. Ström-Olsen, *Nanocrystalline metal hydrides.* Journal of Alloys and Compounds, 1997. **253–254**(0): p. 70-79.

55. Fichtner, M., P. Canton, O. Kircher, and A. Léon, *Nanocrystalline alanates—Phase transformations, and catalysts.* Journal of Alloys and Compounds, 2005. **404–406**(0): p. 732-737.

56. Nielsen, T.K., F. Besenbacher, and T.R. Jensen, *Nanoconfined hydrides for energy storage.* Nanoscale, 2011. **3**(5): p. 2086-2098.

57. Gutowska, A., et al., *Nanoscaffold Mediates Hydrogen Release and the Reactivity of Ammonia Borane.* Angewandte Chemie International Edition, 2005. **44**(23): p. 3578-3582.

58. Feaver, A., S. Sepehri, P. Shamberger, A. Stowe, T. Autrey, and G. Cao, *Coherent Carbon Cryogel−Ammonia Borane Nanocomposites for H_2 Storage.* The Journal of Physical Chemistry B, 2007. **111**(26): p. 7469-7472.

59. Gross, A.F., J.J. Vajo, S.L. Van Atta, and G.L. Olson, *Enhanced Hydrogen Storage Kinetics of $LiBH_4$ in Nanoporous Carbon Scaffolds.* The Journal of Physical Chemistry C, 2008. **112**(14): p. 5651-5657.

60. Zhang, X., R. Yang, J. Qu, W. Zhao, L. Xie, W. Tian, and X. Li, *The synthesis and hydrogen storage properties of pure nanostructured Mg_2FeH_6.* Nanotechnology, 2010. **21**(9): p. 095706/1-095706/7.

61. Polanski, M., T.K. Nielsen, Y. Cerenius, J. Bystrzycki, and T.R. Jensen, *Synthesis and decomposition mechanisms of Mg_2FeH_6 studied by in-situ synchrotron X-ray diffraction and high-pressure DSC.* International Journal of Hydrogen Energy, 2010. **35**(8): p. 3578-3582.

62. Liang, C., G. Sha, and S. Guo, *Resorcinol–formaldehyde aerogels prepared by supercritical acetone drying.* Journal of Non-Crystalline Solids, 2000. **271**(1–2): p. 167-170.

63. Yamamoto, T., T. Nishimura, T. Suzuki, and H. Tamon, *Control of mesoporosity of carbon gels prepared by sol–gel polycondensation and freeze drying.* Journal of Non-Crystalline Solids, 2001. **288**(1–3): p. 46-55.

64. Durairaj, R.B., *Resorcinol: chemistry, technology and applications*. 2005, Berlin [etc.]: Springer.

65. Fricke, J. and T. Tillotson, *Aerogels: production, characterization, and applications.* Thin Solid Films, 1997. **297**(1–2): p. 212-223.

66. Horikawa, T., J.i. Hayashi, and K. Muroyama, *Controllability of pore characteristics of resorcinol–formaldehyde carbon aerogel.* Carbon, 2004. **42**(8–9): p. 1625-1633.

67. Al-Muhtaseb, S.A. and J.A. Ritter, *Preparation and Properties of Resorcinol–Formaldehyde Organic and Carbon Gels.* Advanced Materials, 2003. **15**(2): p. 101-114.

68. Pekala, R.W., C.T. Alviso, F.M. Kong, and S.S. Hulsey, *Aerogels derived from multifunctional organic monomers.* Journal of Non-Crystalline Solids, 1992. **145**(0): p. 90-98.

69. Czakkel, O., K. Marthi, E. Geissler, and K. László, *Influence of drying on the morphology of resorcinol–formaldehyde-based carbon gels.* Microporous and Mesoporous Materials, 2005. **86**(1–3): p. 124-133.

70. Elkhatat, A.M. and S.A. Al-Muhtaseb, *Advances in tailoring resorcinol-formaldehyde organic and carbon gels.* Advanced Materials, 2011. **23**(26): p. 2887-2903.

71. Cerenius, Y., K. Stahl, L.A. Svensson, T. Ursby, A. Oskarsson, J. Albertsson, and A. Liljas, *The crystallography beamline I711 at MAX II.* Journal of Synchrotron Radiation, 2000. **7**(4): p. 203-208.

72. Herklotz, M., F. Scheiba, M. Hinterstein, K. Nikolowski, M. Knapp, A.-C. Dippel, L. Giebeler, J. Eckert, and H. Ehrenberg, *Advances in in situ powder diffraction of battery materials: a case study of the new beamline P02.1 at DESY, Hamburg.* Journal of Applied Crystallography, 2013. **46**(4): p. 1117-1127.

73. Jensen, T.R., T.K. Nielsen, Y. Filinchuk, J.-E. Jorgensen, Y. Cerenius, E.M. Gray, and C.J. Webb, *Versatile in situ powder X-ray diffraction cells for solid-gas investigations.* Journal of Applied Crystallography, 2010. **43**(6): p. 1456-1463.

74. Hammersley, A.P., S.O. Svensson, M. Hanfland, A.N. Fitch, and D. Hausermann, *Two-dimensional detector software: From real detector to idealised image or two-theta scan.* High Pressure Research, 1996. **14**(4-6): p. 235-248.

75. de Boer, J.H., B.G. Linsen, T. van der Plas, and G.J. Zondervan, *Studies on pore systems in catalysts: VII. Description of the pore dimensions of carbon blacks by the t method.* Journal of Catalysis, 1965. **4**(6): p. 649-653.

76. Halsey, G., *Physical Adsorption on Non-Uniform Surfaces.* The Journal of Chemical Physics, 1948. **16**(10): p. 931-937.

77. Brunauer, S., P.H. Emmett, and E. Teller, *Adsorption of Gases in Multimolecular Layers.* Journal of the American Chemical Society, 1938. **60**(2): p. 309-319.

78. Barrett, E.P., L.G. Joyner, and P.P. Halenda, *The Determination of Pore Volume and Area Distributions in Porous Substances. I. Computations from Nitrogen Isotherms.* Journal of the American Chemical Society, 1951. **73**(1): p. 373-380.

79. Toby, B., *EXPGUI, a graphical user interface for GSAS.* Journal of Applied Crystallography, 2001. **34**(2): p. 210-213.

80. Orimo, S., Y. Nakamori, G. Kitahara, K. Miwa, N. Ohba, S. Towata, and A. Züttel, *Dehydriding and rehydriding reactions of.* Journal of Alloys and Compounds, 2005. **404–406**(0): p. 427-430.

81. Bösenberg, U., et al., *Hydrogen sorption properties of MgH_2–$LiBH_4$ composites.* Acta Materialia, 2007. **55**(11): p. 3951-3958.

82. Kou, H.-q., X.-z. Xiao, L.-x. Chen, S.-q. Li, and Q.-d. Wang, *Formation mechanism of MgB_2 in $2LiBH_4$ + MgH_2 system for reversible hydrogen storage.* Transactions of Nonferrous Metals Society of China, 2011. **21**(5): p. 1040-1046.

83. Harvey, K.B. and N.R. McQuaker, *Infrared and Raman Spectra of Potassium and Sodium Borohydride.* Canadian Journal of Chemistry, 1971. **49**(20): p. 3272-3281.

84. Gomes, S., H. Hagemann, and K. Yvon, *Lithium boro-hydride $LiBH_4$: II. Raman spectroscopy.* Journal of Alloys and Compounds, 2002. **346**(1–2): p. 206-210.

85. Brampton, D., *Destabilization of lithium borohydride with additions of magnesium hydride*, in *Department of Metallurgy and Materials*2010, University of Birmingham. p. 122.

86. Shaw, L.L., X. Wan, J.Z. Hu, J.H. Kwak, and Z. Yang, *Solid-State Hydriding Mechanism in the $LiBH_4 + MgH_2$ System.* The Journal of Physical Chemistry C, 2010. **114**(17): p. 8089-8098.

87. Langmi, H.W., G.S. McGrady, R. Newhouse, and E. Rönnebro, *Mg_2FeH_6–$LiBH_4$ and Mg_2FeH_6–$LiNH_2$ composite materials for hydrogen storage.* International Journal of Hydrogen Energy, 2012. **37**(8): p. 6694-6699.

88. Orimo, S.-I., Y. Nakamori, N. Ohba, K. Miwa, M. Aoki, S.-i. Towata, and A. Züttel, *Experimental studies on intermediate compound of $LiBH_4$.* Applied Physics Letters, 2006. **89**(2): p. -.

89. Kang, J.K., S.Y. Kim, Y.S. Han, R.P. Muller, and W.A. Goddard, *A candidate $LiBH_4$ for hydrogen storage: Crystal structures and reaction mechanisms of intermediate phases.* Applied Physics Letters, 2005. **87**(11): p. -.

90. Price, T.E.C., D.M. Grant, V. Legrand, and G.S. Walker, *Enhanced kinetics for the $LiBH_4$:MgH_2 multi-component hydrogen storage system – The effects of stoichiometry and decomposition environment on cycling behaviour.* International Journal of Hydrogen Energy, 2010. **35**(9): p. 4154-4161.

91. Price, T.E.C., D.M. Grant, I. Telepeni, X.B. Yu, and G.S. Walker, *The decomposition pathways for $LiBD_4$–MgD_2 multicomponent systems investigated by in situ neutron diffraction.* Journal of Alloys and Compounds, 2009. **472**(1–2): p. 559-564.

92. Bösenberg, U., et al., *Pressure and Temperature Influence on the Desorption Pathway of the $LiBH_4$–MgH_2 Composite System.* The Journal of Physical Chemistry C, 2010. **114**(35): p. 15212-15217.

93. Mauron, P., F. Buchter, O. Friedrichs, A. Remhof, M. Bielmann, C.N. Zwicky, and A. Zuttel, *Stability and Reversibility of $LiBH_4$.* The Journal of Physical Chemistry B, 2007. **112**(3): p. 906-910.

94. Puszkiel, J.A., P.A. Larochette, and F.C. Gennari, *Thermodynamic and kinetic studies of Mg-Fe-H after mechanical milling followed by sintering.* Journal of Alloys and Compounds, 2008. **463**(1-2): p. 134-142.

95. Puszkiel, J.A., P. Arneodo Larochette, and F.C. Gennari, *Thermodynamic-kinetic characterization of the synthesized Mg_2FeH_6-MgH_2 hydrides mixture.* International Journal of Hydrogen Energy, 2008. **33**(13): p. 3555-3560.

96. Avrami, M., *Kinetics of Phase Change. I General Theory.* The Journal of Chemical Physics, 1939. **7**(12): p. 1103-1112.

97. Jena, A.K.C.M.C., *Phase transformation in materials*. 1992, Englewood Cliffs, N.J.: Prentice Hall.

98. Cahn, J.W., *Transformation kinetics during continuous cooling.* Acta Metallurgica, 1956. **4**(6): p. 572-575.

99. Galwey, A.K. and M.E. Brown, *Chapter 3 Kinetic Background to Thermal Analysis and Calorimetry*, in *Handbook of Thermal Analysis and Calorimetry*, E.B. Michael, Editor. 1998, Elsevier Science B.V. p. 147-224.

100. Lozano, G.A., C.N. Ranong, J.M. Bellosta von Colbe, R. Bormann, G. Fieg, J. Hapke, and M. Dornheim, *Empirical kinetic model of sodium alanate reacting system (I). Hydrogen absorption.* International Journal of Hydrogen Energy, 2010. **35**(13): p. 6763-6772.

101. Lozano, G.A., C.N. Ranong, J.M. Bellosta von Colbe, R. Bormann, G. Fieg, J. Hapke, and M. Dornheim, *Empirical kinetic model of sodium alanate reacting system (II). Hydrogen desorption.* International Journal of Hydrogen Energy, 2010. **35**(14): p. 7539-7546.

102. Bard, A.J. and L.R. Faulkner, *Electrochemical Methods: Fundamentals and Applications*. 2000: Wiley.

103. Lin, C. and J.A. Ritter, *Effect of synthesis pH on the structure of carbon xerogels.* Carbon, 1997. **35**(9): p. 1271-1278.

104. Job, N., R. Pirard, J. Marien, and J.-P. Pirard, *Porous carbon xerogels with texture tailored by pH control during sol–gel process.* Carbon, 2004. **42**(3): p. 619-628.

105. Contreras, M.S., C.A. Páez, L. Zubizarreta, A. Léonard, S. Blacher, C.G. Olivera-Fuentes, A. Arenillas, J.-P. Pirard, and N. Job, *A comparison of physical activation of carbon xerogels with carbon dioxide with chemical activation using hydroxides.* Carbon, 2010. **48**(11): p. 3157-3168.

106. Wieczorek-Ciurowa, K. and A.J. Kozak, *The Thermal Decomposition of Fe(NO3)3·9H2O.* Journal of Thermal Analysis and Calorimetry, 1999. **58**(3): p. 647-651.

107. Petkov, V., P.D. Cozzoli, R. Buonsanti, R. Cingolani, and Y. Ren, *Size, Shape, and Internal Atomic Ordering of Nanocrystals by Atomic Pair Distribution Functions: A Comparative Study of γ-Fe_2O_3 Nanosized Spheres and Tetrapods.* Journal of the American Chemical Society, 2009. **131**(40): p. 14264-14266.

108. Ellingham, H., *Transactions and Communications.* Journal of the Society of Chemical Industry, 1944. **63**(5): p. 125-160.

109. Tao, Y., M. Endo, and K. Kaneko, *A Review of Synthesis and Nanopore Structures of Organic Polymer Aerogels and Carbon Aerogels.* Recent Patents on Chemical Engineering, 2008. **1**(3): p. 192-200.

110. Lin, H.-Y., Y.-W. Chen, and C. Li, *The mechanism of reduction of iron oxide by hydrogen.* Thermochimica Acta, 2003. **400**(1–2): p. 61-67.

111. Pineau, A., N. Kanari, and I. Gaballah, *Kinetics of reduction of iron oxides by H2: Part I: Low temperature reduction of hematite.* Thermochimica Acta, 2006. **447**(1): p. 89-100.

112. Richard W. Pekala, P.H.C.A., *Low density, resorcinol-formaldehyde aerogels*, 1991, US 4104208 (Aug, 1978) Kido et al. 521/141; US 4663358 (May, 1987) Hyon et al. 521/141; US 4861804 (Aug, 1989) Nakamishi 521/154; US 4863972 (Sep, 1989) Itagaki et al. 521/141; US 4873218 (Oct, 1989) Pekala 521/64; US 4888364 (Dec, 1989) Graiver et al. 521/141: US.

113. Zhang, R., W. Li, K. Li, C. Lu, L. Zhan, and L. Ling, *Effect of concentration of reactants on porosity of hydrogels, organic and carbon aerogels.* Microporous and Mesoporous Materials, 2004. **72**(1–3): p. 167-173.

114. Huot, J., H. Hayakawa, and E. Akiba, *Preparation of the hydrides Mg_2FeH_6 and Mg_2CoH_5 by mechanical alloying followed by sintering.* J. Alloys Compd., 1997. **248**(1-2): p. 164-167.

115. Norek, M., T.K. Nielsen, M. Polanski, I. Kunce, T. Płociński, L.R. Jaroszewicz, Y. Cerenius, T.R. Jensen, and J. Bystrzycki, *Synthesis and decomposition mechanisms of ternary Mg_2CoH_5 studied using in situ synchrotron X-ray diffraction.* International Journal of Hydrogen Energy, 2011. **36**(17): p. 10760-10770.

116. Baitalow, F., G. Wolf, J.P.E. Grolier, F. Dan, and S.L. Randzio, *Thermal decomposition of ammonia-borane under pressures up to 600 bar.* Thermochim. Acta, 2006. **445**(Copyright (C) 2012 American Chemical Society (ACS). All Rights Reserved.): p. 121-125.

117. Ghaani, M.R., M. Catti, and A. Nale, *Thermodynamics of Dehydrogenation of the $2LiBH_4$–Mg_2FeH_6 Composite.* The Journal of Physical Chemistry C, 2012. **116**(51): p. 26694-26699.

118. Catti, M., M.R. Ghaani, and I. Pinus, *Overpressure Role in Isothermal Kinetics of H2 Desorption–Absorption: the $2LiBH_4$–Mg_2FeH_6 System.* The Journal of Physical Chemistry C, 2013. **DOI:** 10.1021/jp409009n.

119. Zheng, J., et al., *Enhanced Li+ ion transport in $LiNi_{0.5}Mn_{1.5}O_4$ through control of site disorder.* Physical Chemistry Chemical Physics, 2012. **14**(39): p. 13515-13521.

120. Kang, S.-H., D.P. Abraham, W.-S. Yoon, K.-W. Nam, and X.-Q. Yang, *First-cycle irreversibility of layered Li–Ni–Co–Mn oxide cathode in Li-ion batteries.* Electrochimica Acta, 2008. **54**(2): p. 684-689.

121. Reddy, M.A. and U.V. Varadaraju, *Facile Insertion of Lithium into Nanocrystalline $AlNbO_4$ at Room Temperature.* Chemistry of Materials, 2008. **20**(14): p. 4557-4559.

122. Han, J.-T., D.-Q. Liu, S.-H. Song, Y. Kim, and J.B. Goodenough, *Lithium Ion Intercalation Performance of Niobium Oxides: KNb_5O_{13} and $K_6Nb_{10.8}O_{30}$.* Chemistry of Materials, 2009. **21**(20): p. 4753-4755.

123. Han, J.-T. and J.B. Goodenough, *3-V Full Cell Performance of Anode Framework $TiNb_2O_7$/Spinel $LiNi_{0.5}Mn_{1.5}O_4$.* Chemistry of Materials, 2011. **23**(15): p. 3404-3407.

124. Yamaki, J.-i., S.-i. Tobishima, K. Hayashi, S. Keiichi, Y. Nemoto, and M. Arakawa, *A consideration of the morphology of electrochemically deposited lithium in an organic electrolyte.* Journal of Power Sources, 1998. **74**(2): p. 219-227.

125. Nishikawa, K., T. Mori, T. Nishida, Y. Fukunaka, and M. Rosso, *Li dendrite growth and Li^+ ionic mass transfer phenomenon.* Journal of Electroanalytical Chemistry, 2011. **661**(1): p. 84-89.

126. Nakahara, K., R. Nakajima, T. Matsushima, and H. Majima, *Preparation of particulate $Li_4Ti_5O_{12}$ having excellent characteristics as an electrode active material for power storage cells.* Journal of Power Sources, 2003. **117**(1–2): p. 131-136.

127. Cheng, L., H.-J. Liu, J.-J. Zhang, H.-M. Xiong, and Y.-Y. Xia, *Nanosized Li4Ti5O12 Prepared by Molten Salt Method as an Electrode Material for Hybrid Electrochemical Supercapacitors.* Journal of The Electrochemical Society, 2006. **153**(8): p. A1472-A1477.

128. Kodama, R., Y. Terada, I. Nakai, S. Komaba, and N. Kumagai, *Electrochemical and In Situ XAFS-XRD Investigation of Nb_2O_5 for Rechargeable Lithium Batteries.* Journal of The Electrochemical Society, 2006. **153**(3): p. A583-A588.

129. Kumagai, N., Y. Koishikawa, S. Komaba, and N. Koshiba, *Thermodynamics and Kinetics of Lithium Intercalation into Nb_2O_5 Electrodes for a 2 V Rechargeable Lithium Battery.* Journal of The Electrochemical Society, 1999. **146**(9): p. 3203-3210.

130. Wei, M., K. Wei, M. Ichihara, and H. Zhou, *Nb_2O_5 nanobelts: A lithium intercalation host with large capacity and high rate capability.* Electrochemistry Communications, 2008. **10**(7): p. 980-983.

131. Nico, C., M.R.N. Soares, J. Rodrigues, M. Matos, R. Monteiro, M.P.F. Graça, M.A. Valente, F.M. Costa, and T. Monteiro, *Sintered NbO Powders for Electronic Device Applications.* The Journal of Physical Chemistry C, 2011. **115**(11): p. 4879-4886.

132. Reznichenko, L.A., V.V. Akhnazarova, L.A. Shilkina, O.N. Razumovskaya, and S.I. Dudkina, *Invar effect in n-Nb_2O_5, αht-Nb_2O_5, and L-Nb_2O_5.* Crystallography Reports, 2009. **54**(3): p. 483-491.

133. Kato, K., *Structure refinement of H-Nb2O5.* Acta Crystallographica Section B, 1976. **32**(3): p. 764-767.

134. Sten, A., *Phase Analysis Studies on the $NaNbO_3$-Nb_2O_5, NaF-Nb_2O_5, and $NaNbO_3$-Nb_2O_5-H_2O Systems.* Acta Chemica Scandinavica, 1967. **21**: p. 1777-1782.

135. Sten, A., *The thermal decomposition of NbO_2F.* Acta Chemica Scandinavica, 1965. **19**: p. 2136-2138.

136. Muthurajan, H., N.K. Rao, U.N. Gupta, S. Pradhan, R.K. Jha, H.H. Kumar, S.A. Mirji, and V. Ravi, *Novel hydroxide precursors for low temperature synthesis of selected ternary oxides.* Materials Research Bulletin, 2008. **43**(7): p. 1842-1849.

137. Zhang, D.-Q., Z.-C. Qin, X.-Y. Yang, H.-B. Zhu, and M.-S. Cao, *Study on synthesis and evolution of sodium potassium niobate ceramic powders by an oxalic acid-based sol–gel method.* Journal of Sol-Gel Science and Technology, 2011. **57**(1): p. 31-35.

138. Holtzberg, F., A. Reisman, M. Berry, and M. Berkenblit, *Chemistry of the Group VB Pentoxides. VI. The Polymorphism of Nb_2O_5.* Journal of the American Chemical Society, 1957. **79**(9): p. 2039-2043.

139. Mertin, W., S. Andersson, and R. Gruehn, *Über die Kristallstruktur von M・Nb_2O_5.* Journal of Solid State Chemistry, 1970. **1**(3–4): p. 419-424.

140. Brayner, R. and F. Bozon-Verduraz, *Niobium pentoxide prepared by soft chemical routes: morphology, structure, defects and quantum size effect.* Physical Chemistry Chemical Physics, 2003. **5**(7): p. 1457-1466.

141. Narendar, Y. and G.L. Messing, *Synthesis, Decomposition and Crystallization Characteristics of Peroxo−Citrato−Niobium: An Aqueous Niobium Precursor.* Chemistry of Materials, 1997. **9**(2): p. 580-587.

142. Cava, R.J., D.W. Murphy, and S.M. Zahurak, *Lithium Insertion in Wadsley-Roth Phases Based on Niobium Oxide.* Journal of The Electrochemical Society, 1983. **130**(12): p. 2345-2351.

143. Cockcroft, J.K. *High-Resolution Diffractometers*. [cited 2013 December 12]; Available from: http://pd.chem.ucl.ac.uk/pdnn/inst3/diff1.htm.

144. Larson, A.C. and R.B. Von Dreele, *General Structure Analysis System (GSAS).* Los Alamos National Laboratory Report LAUR, 1994(86).

145. Von Dreele, R.B., J.D. Jorgensen, and C.G. Windsor, *Rietveld refinement with spallation neutron powder diffraction data.* Journal of Applied Crystallography, 1982. **15**(6): p. 581-589.

146. Thompson, P., D.E. Cox, and J.B. Hastings, *Rietveld refinement of Debye-Scherrer synchrotron X-ray data from Al_2O_3.* Journal of Applied Crystallography, 1987. **20**(2): p. 79-83.

147. Catti, M. and M.R. Ghaani, *On the lithiation reaction of niobium oxide: structural and electronic properties of $Li_{1.714}Nb_2O_5$.* Physical Chemistry Chemical Physics, 2014. **DOI:** 10.1039/C3CP54215G.